UPPER HYBRID RESONANCE ABSORPTION AND SCATTERING FROM A PLASMA COLUMN

Thesis by

Richard Harold Ault

In Partial Fulfillment of the Requirements

for the Degree of

Doctor of Philosophy

California Institute of Technology

Pasadena, California

1971

(Submitted March 12, 1971)

ACKNOWLEDGMENTS

The author wishes to express deep appreciation to Professor Roy W. Gould for his guidance and advice throughout the course of this research. The many interesting discussions with members of the Plasma Laboratory research group were most helpful. The author is especially grateful to Dr. Reiner Stenzel, without whose aid and experimental expertise this work would not have been possible. Deepest thanks also go to Mrs. Ruth Stratton for her superb typing of the final draft.

The author acknowledges the financial assistance he has received from Caltech, N.S.F., and the Woodrow Wilson Foundation. This investigation was supported by the U. S. Atomic Energy Commission.

The author has not adequate words to express his gratefulness to his wife.

ABSTRACT

The electromagnetic scattering and absorption properties of small ($kr \sim 1/2$) inhomogeneous magnetoplasma columns are calculated via the full set of Maxwell's equations with tensor dielectric constitutive relation. The cold plasma model with collisional damping is used to describe the column. The equations are solved numerically, subject to boundary conditions appropriate to an infinite parallel strip line and to an incident plane wave. The results are similar for several density profiles and exhibit semiquantitative agreement with measurements in waveguide. The absorption is spatially limited, especially for small collision frequency, to a narrow hybrid resonant layer and is essentially zero when there is no hybrid layer in the column. The reflection is also enhanced when the hybrid layer is present, but the value of the reflection coefficient is strongly modified by the presence of the glass tube. The nature of the solutions and an extensive discussion of the conditions under which the cold collisional model should yield valid results is presented.

CONTENTS

I. Introduction

1.1 Historical background

Perhaps the most ubiquitous characteristic of matter in the plasma state is that small disturbances in the local charge neutrality result in strong local electrostatic restoring forces. The pioneering works by Langmuir and Tonks [1] showed that, in the absence of thermal motion, these electrostatic restoring forces cause perturbations in the equilibrium electron density to oscillate about their local equilibrium point at the electron plasma frequency ω_p. In 1931 Tonks [2] showed that in addition to such local oscillations at ω_p, the electrons in a bounded uniform plasma will also oscillate about the stationary ions due to the fields resulting from the charge separation at the plasma boundary. These fields, and thus the oscillation frequency, are dependent on the boundary shape and, in particular, a uniform slab oscillates at ω_p while a small uniform cylinder oscillates at $\omega_p/\sqrt{2}$. Early attempts to calculate the scattering from finite-sized plasmas used such uniform bounded models. In 1951 Herlofson [3] showed that the surface-charge driven modes of a uniform cylinder oscillate at $\omega_p/\sqrt{2}$ independent of the azimuthal distribution, but that a uniform external field perpendicular to the column axis couples most strongly to the dipolar mode. Thus the broad peak which occurs in experimentally measured scattering properties of small plasma columns at $\omega \sim \overline{\omega}_p/\sqrt{2}$ came to be known as the cold plasma main or dipolar resonance.

Development of the cold-plasma theory for a nonuniform density profile was hampered because the steady-state plasma response and the

internal electromagnetic fields are singular in the collision-free case at any surface on which the local plasma frequency is equal to the driving frequency and, as a consequence of the singular response, the cold collision-free plasma model appears to absorb energy at the singular surface. Although Herlofson proposed the correct method for treating this singular behavior in 1951, the collisionless absorption was not completely understood until 1964 when Barston [4] showed that the absorption arises because the collision-free plasma cannot attain a steady state at the resonant surface. As the time since the driving field has been turned on increases, there is a steadily narrowing band of electrons near the hybrid surface which have not reached their local steady state. The energy in this narrowing band of nonsteady-state electrons increases at a constant rate and appears as a steady-state "absorption", but the energy is actually being stored in the motion of this band of electrons (see Henderson [5] for further discussion and references).

When a plasma is placed in an external static magnetic field $\underset{\sim}{B}_0$ the $\underset{\sim}{v} \times \underset{\sim}{B}_0$ force combines with the electrostatic restoring forces so as to cause perturbations in the electron density to oscillate at the upper hybrid frequency $\omega_{uh}^2 = \omega_p^2 + \omega_c^2$ where ω_c is the electron cyclotron frequency. The scattering from bounded magnetoplasmas was first discussed [6,7,8] in the early 1960's.* Using bounded uniform plasma models, these treatments led to a description

*Some results were obtained earlier for uniaxial plasmas ($|\underset{\sim}{B}_0| = \infty$), see Stix [9] pp. 103-104 for additional references.

of the cold magnetoplasma scattering in terms of the dipolar surface-charge resonances analogous to the magnetic field-free case. However, such descriptions could not account for the width of the observed resonances, and it was postulated that the resonance width was a consequence of the inhomogeneity in the plasma density [10].

Budden [11] discussed qualitatively the reflection and transmission of a wave propagating perpendicular to $\underset{\sim}{B}_0$ through a weakly inhomogeneous plasma slab using WKB methods. This approach uses the refractive index of a plane wave propagating in an infinite uniform plasma to describe the local propagation properties of a plasma with varying density. For the scattering problem of interest in the current work, both the electric field and the propagation vector of the incident wave are perpendicular to $\underset{\sim}{B}_0$, so the appropriate propagation properties are given by the "extraordinary" branch [9] of the cold plasma refractive index. For the extraordinary mode the square of the refractive index [9] is

$$\mu_{ex}^2 = \frac{(1 - \omega_p^2/\omega^2)^2 - \omega_c^2/\omega^2}{(1 - \omega_c^2/\omega^2 - \omega_p^2/\omega^2)}$$

and is depicted in Fig. 1.1 as a function of ω_p^2/ω^2 (a normalized electron density) for $0 < \omega_c < \omega$. The important features of the refractive index are the cutoff points at $1 - \omega_c/\omega$ and $1 + \omega_c/\omega$ where the refractive index is zero, the hybrid point at $1 - \omega_c^2/\omega^2$

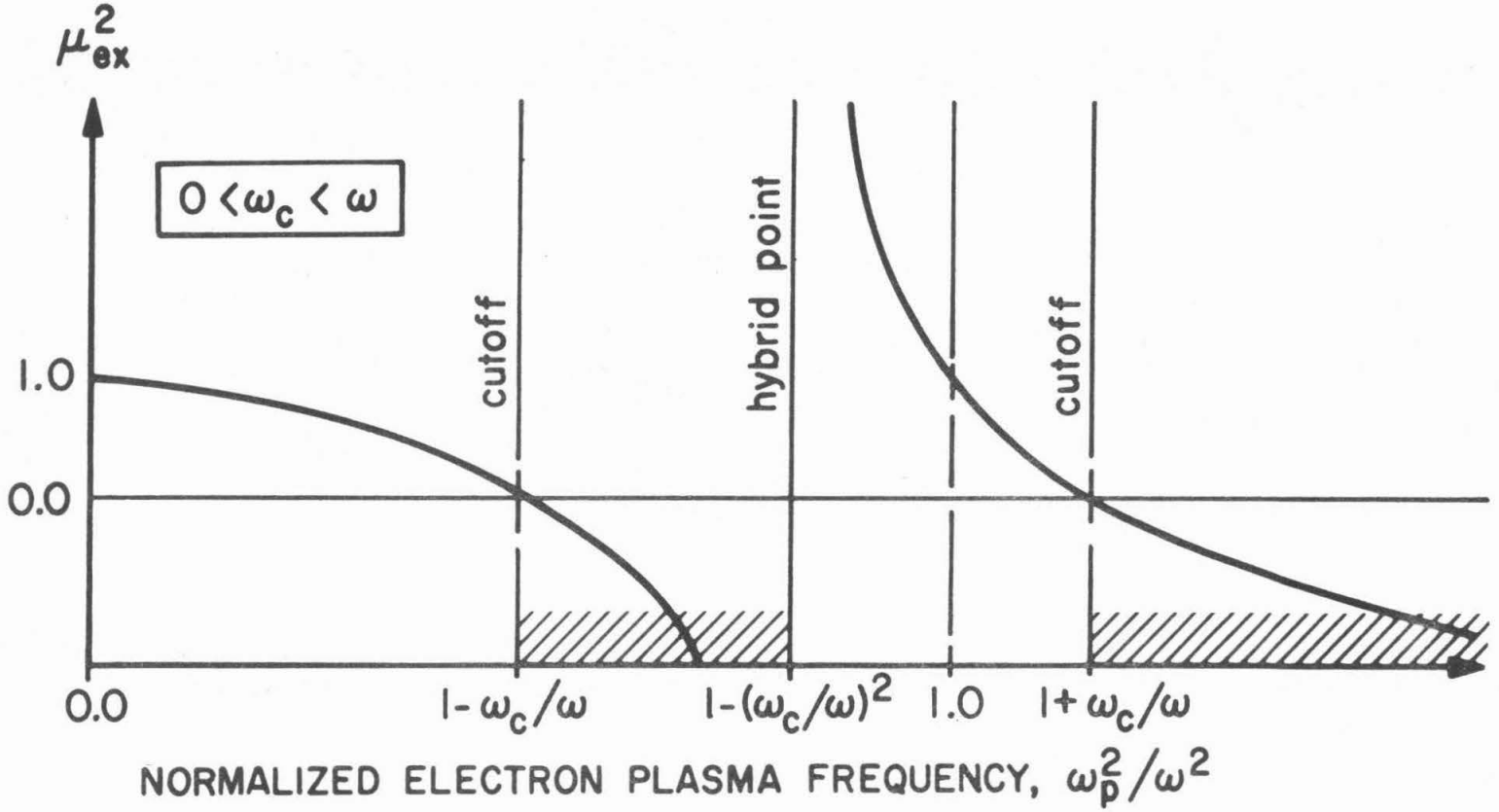

Fig. 1.1 Square of the extraordinary mode refractive index for fixed magnetic field such that $0 < \omega_c < \omega$ Extraordinary waves are evanescent for ω_p^2/ω^2 in shaded regions. As the magnetic field increases, the left-hand cutoff and the resonance move to lower densities until they coalesce at $\omega_p^2/\omega^2 = 0$ when $\omega_c = \omega$. For $\omega_c > \omega$, μ_{ex}^2 decreases smoothly from 1.0 to the right-hand cutoff.

where the refractive index is infinite*, and the evanescent† regions in which the square of the refractive index is negative.

Since ω_p^2 is proportional to the electron density, Fig. 1.1 also gives μ_{ex}^2 as a function of position for a plasma slab with a density profile that increases linearly from 0.0. A wave incident on such an inhomogeneous plasma slab from free space would be propagating from left to right in Fig. 1.1 and, when $0 < \omega_c < \omega$, it would encounter the cutoff at $\omega_p^2/\omega^2 = 1 - \omega_c/\omega$, the left-hand evanescent region, the hybrid point, the right-hand cutoff, and the right-hand evanescent region, in that order.

Budden [11] demonstrated that the scattering of such a wave depended on the spatial extent, in wavelengths, of the left-hand evanescent region between the first cutoff and the hybrid point. When the evanescent region is optically thick, the incident wave will be entirely reflected at the left-hand cutoff point and will be unaffected

---

*When the magnetic field is nonzero, the induced currents in an inhomogeneous plasma are infinite at any surface on which the driving frequency satisfies the hybrid condition. It is because of this infinite response, not the infinity in the refractive index, that such surfaces are denoted as resonant surfaces. When the magnetic field is zero, the cutoffs and the infinity in μ_{ex}^2 coalesce into a cutoff at $\omega_p^2/\omega = 1.0$ and the resonant response in an inhomogeneous plasma occurs at a zero in the local refractive index.

†Waves in an evanescent region spatially decay without loss of energy.

by the hybrid resonance. When the evanescent region is thin, the wave can tunnel through it to the resonance where it will undergo partial reflection, transmission*, and absorption.

Kuckes and Wong [12] calculated the absorption of a wave traveling through a thick ($k_0 x \sim 22$), bounded, collisional, slab magnetoplasma with a parabolic density profile as a function of magnetic field. The peak density was assumed to be low enough that $\omega_{p\ max}^2/\omega^2 < 1$, so the incident wave will propagate everywhere in the plasma when $\omega_c/\omega < 1 - \omega_{p\ max}^2/\omega^2$ or $\omega_c/\omega \geq 1$. When $1 - \omega_{p\ max}^2/\omega^2 \leq \omega_c/\omega < \sqrt{1 - \omega_{p\ max}^2/\omega^2}$, the left-hand cutoff shown in Fig. 1.1 appears in the slab and the incident wave is evanescent in the center of the slab. When $\sqrt{1 - \omega_{p\ max}^2/\omega^2} \leq \omega_c/\omega < 1$, both the left-hand cutoff and the hybrid surface can appear in the slab, as shown in Fig. 1.2. The calculated absorption curves, like the one illustrated in Fig. 1.3a, show two sharp peaks, one when the cutoff appears in the plasma core and another when $\omega_c/\omega = 1$. The reduction in absorption after the cutoff appears in the plasma core was attributed to a reduction in the effective absorbing volume of the plasma due to wave reflection at the cutoff point. The peak in absorption at $\omega_c/\omega = 1$ was interpreted as arising from the increasing tunneling through the steadily narrowing evanescent region to the strongly absorbing hybrid resonance as both the hybrid and cutoff points

---

*In a semi-infinite slab with constantly increasing density, this transmitted wave will propagate to the right-hand cutoff where it will be totally reflected back toward decreasing densities.

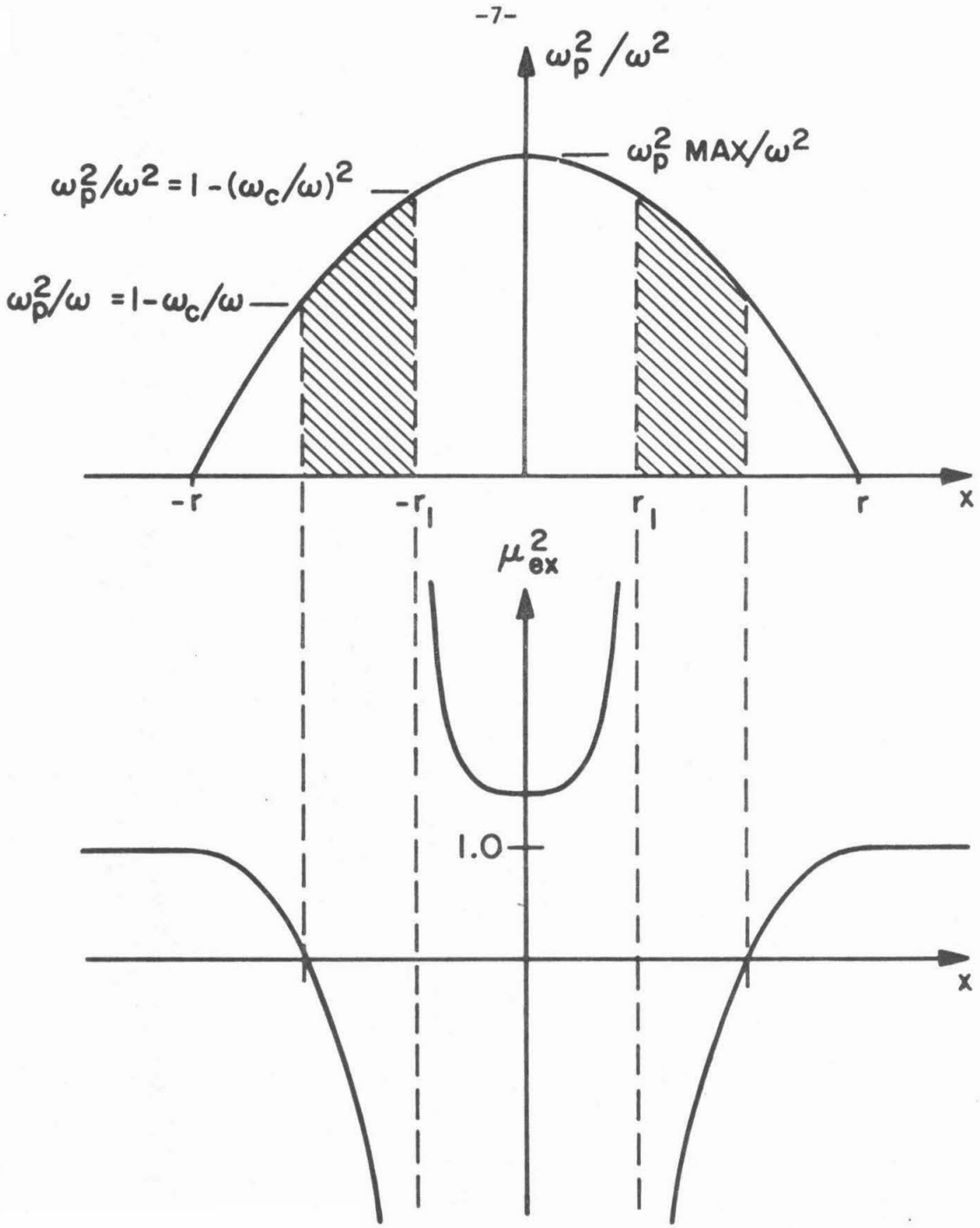

Fig. 1.2 Square of the refractive index and plasma density as a function of position for a slab plasma with a parabolic density profile for $\sqrt{1-\omega_{p\ max}^2/\omega^2} \leq \omega_c/\omega \leq 1$. The extraordinary wave is evanescent in the shaded regions. The hybrid resonance occurs at $x = \pm r_1$.

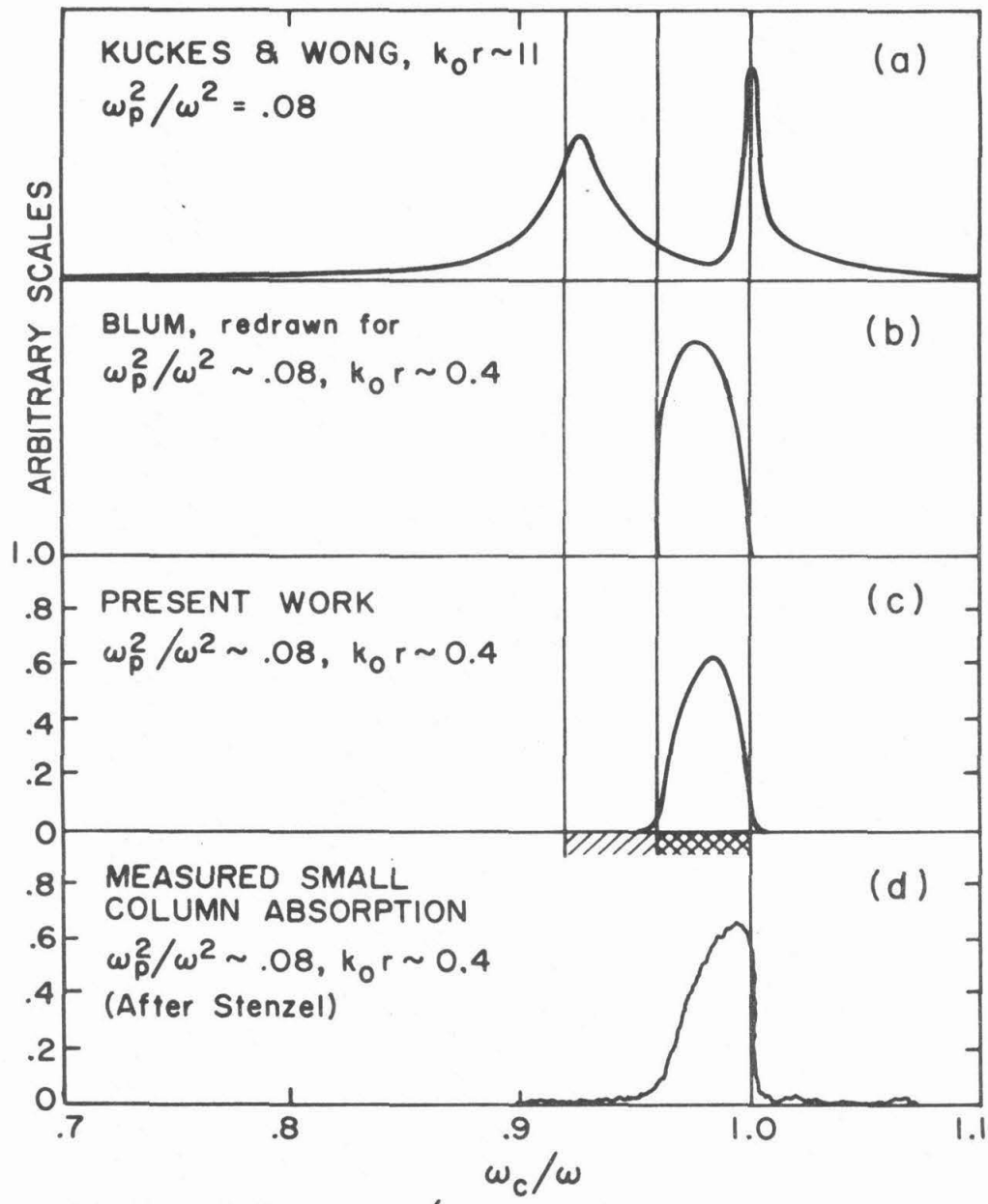

Shadings indicate ω_c/ω such that:

//////: cutoff condition satisfied in plasma

⊠⊠⊠⊠: cutoff and resonance conditions satisfied in plasma

Fig. 1.3 Absorption as a function of ω_c/ω as calculated by various theoretical approaches and a sample of Stenzel's [15] small column measurements. All curves are for similar peak plasma densities, but they are intended only for qualitative comparison due to the differences in approach.

approached the surface of the slab.

In order to describe a small column $k_0 r \sim 1/2$, Blum [13,14] eliminated both collisional and propagation effects by calculating the complex admittance of a collisionless, cold magnetoplasma slab in a parallel plate capacitor. This admittance was used to calculate the reflection and absorption properties of a plasma shunting a waveguide section. Since absorption can occur only at the hybrid resonance in the collisionless cold plasma model, Blum's calculation could show nonzero absorption only when a hybrid layer was present in the slab. A typical calculated absorptivity is illustrated in Fig. 1.3b. In contrast to the results for a thick slab, the absorptivity shows only a single, smooth peak with a sharp onset when the hybrid resonance appeared at the center of the slab. The calculated reflectivity of the plasma-loaded waveguide showed one peak when the hybrid resonance was at the center of the slab and another at $\omega_c/\omega = 1$.

Blum's calculated results show a reasonable qualitative comparison with experimental measurements of the scattering from small plasma columns ($k_0 r \sim 1/2$) . An experimentally measured absorption curve which is typical of Stenzel's [15] results for a small column is depicted in Fig. 1.3d. The experimental results show a sharply defined enhanced band just below cyclotron resonance ($\omega_c/\omega = 1$) similar to the calculated absorptivity. Blum's [13] experimentally measured reflectivities showed double peaks similar to his calculated reflectivities; however, experimentally measured absorption onsets occurred at values of ω_c/ω which were less than the values at which the corresponding reflection peaks occurred. The onset of significant

scattering has been used empirically as a diagnostic for the peak plasma density, as discussed in Section 5.4, but the disagreements between the locations of the experimentally measured absorption onsets and corresponding reflection peaks make precise interpretation of the scattering measurements difficult.

1.2 Present work

The current work was initiated in an attempt to obtain theoretical results which could be more quantitatively compared with experimental data for small columns. In this work the scattering properties of a cylindrical plasma column in a parallel plate line are calculated retaining the propagation effects. This geometry is considerably closer to the experimental situation of a cylindrical column in a waveguide than is that of a one-dimensional slab in a capacitor. The effects of the glass tube surrounding the plasma have also been included explicitly in the calculation. The plasma will be described by a cold plasma model which retains damping effects.

Chapter 2 presents the methods used to calculate the cold plasma scattering coefficients. The geometry is discussed in Section 2.1, and Maxwell's equations in a cold cylindrical plasma are developed in Section 2.2. The boundary conditions for a cylindrical plasma column in an incident plane wave field, including the effects of the glass tube which contains the plasma, are developed in Section 2.3. The plane wave scattering coefficients calculated in Section 2.3 are then employed in Section 2.4 to treat the parallel plate transmission line (strip line) problem via the method of images.

A discussion of the nature of the hybrid layer in a cold, collisional plasma, illustrated by some of the computed solutions of the field equations, is presented in Chapter 3. The theoretical discussion is accompanied by some results which are indicative of resonant behavior in experimental plasmas.

The approximations involved in using the simple cold plasma model are discussed in Chapter 4. Finite temperature effects are of particular interest since additional wave propagation modes (the Bernstein [16] modes) are predicted by warm plasma theories, and these modes can be coupled to the electromagnetic modes which exist in a cold plasma by the strong gradients which occur at the hybrid resonance. This coupling might be expected to modify significantly the fields and currents at the hybrid layer and can effect the external scattering, as demonstrated by the Buchsbaum-Hasegawa [17] fine structure. The consequences of these warm plasma effects have been investigated by developing simplified model wave equations valid near the hybrid point. The warm plasma model equation is based on a low temperature wave equation derived by Baldwin [18] using a small Larmour radius expansion of Boltzman's equation. In Section 4.4, the analytic solutions of the cold plasma model equation are compared with asymptotic solutions of the warm plasma model equation developed by Rabenstein [19] . On the basis of this comparison, it is demonstrated that the finite temperature effects do not significantly alter the cold plasma solutions on the low density side of the hybrid layer

under certain conditions*. These results lead to the conclusion that the cold plasma model should be adequate to describe the scattering results for many low temperature plasma experiments.

Calculated scattering curves are presented in Chapter 5 which demonstrate the effects of variations in the external geometry and in the parameters which describe the plasma. Some of Stenzel's [15] experimental scattering measurements are presented for comparison with corresponding calculated curves. While the calculated results do not show the effects of the cutoff in the local refractive index, the importance of propagation effects are illustrated by a comparison between the results of the current work and an electrostatic calculation carried out for similar geometry by Baldwin and Ignat (as reported in Henderson [5]). The theoretical scattering results establish that the onset of enhanced absorption can be reliably used as a diagnostic of the peak plasma density in small inhomogeneous columns. The results of this work also indicate that the onset of significant enhanced reflection does not necessarily correspond to the maximum upper hybrid frequency and should not be used as a diagnostic.

A summary of the major conclusions of this work and suggestions for further study are presented in Chapter 6. For convenience of the reader, a list of symbols and their definitions appear in Appendix A.

---

*Baldwin [20] and Baldwin and Ignat [21], employing an electrostatic approximation, have arrived at analogous conditions for the validity of the cold-plasma theory in the magnetic field-free case.

II. Method of Calculation

2.1 Geometrical approximations

In an empty waveguide Maxwell's equations reduce to two independent second-order partial differential equations (p.d.e.'s) whose solutions are denoted as the TE and TM modes. The usual choice of working frequency is such that only a TE mode propagates and thus the field in the waveguide can be derived from a single second-order p.d.e. The presence of an obstruction (with a few useful exceptions) couples the TE and TM modes, so treating an obstruction in a waveguide usually requires the solution of two second-order p.d.e.'s. If the obstruction is a linear, isotropic, homogeneous dielectric, or a conductor, the TM and TE modes are coupled only at the boundaries and the p.d.e.'s may be solved separately. But, the magnetoplasma column is neither homogeneous nor isotropic, so the waveguide problem requires the simultaneous solution of two coupled second-order p.d.e.'s. Finally, there seems to be no satisfactory method of specifying the fields in the plasma at the holes in the waveguide walls.

In view of the difficulties with the real waveguide geometry, the current work treats the simpler, physically similar geometry of an infinitely long cylindrical plasma between two infinite parallel conducting planes which form a strip line. This theoretical geometry is indicated in Fig. 2.1, where the vertical spacing of the strip line is equal to the vertical height of the experimental waveguide. The strip line problem is completely independent of the axial coordinate z both inside and outside the plasma if there are no density gradients

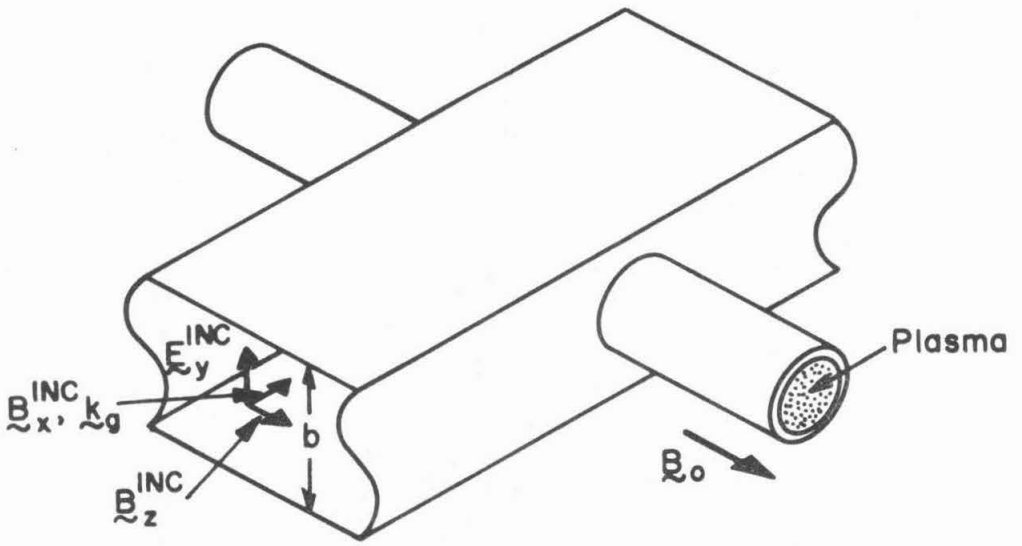

EXPERIMENTAL

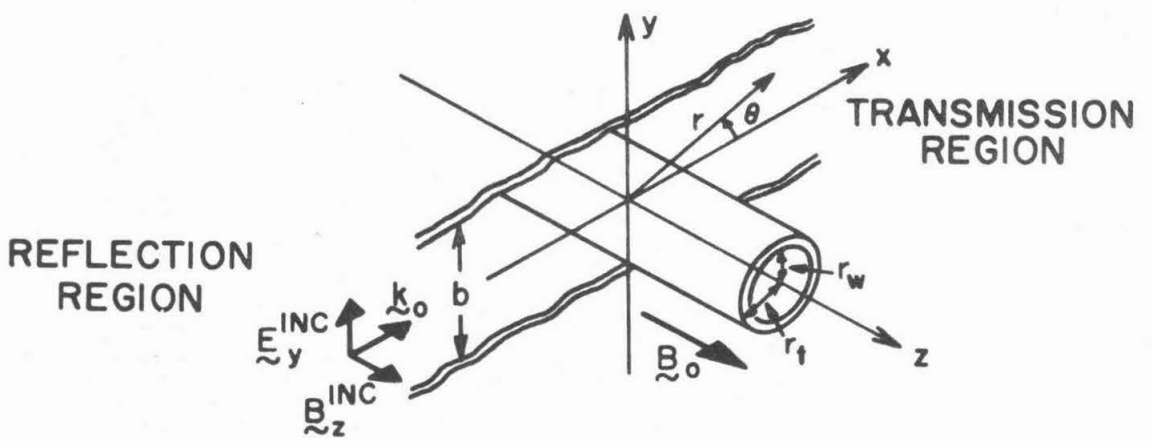

THEORETICAL

Fig. 2.1 The experimental waveguide and theoretical strip line geometries are indicated in the upper and lower sketches respectively. Both the rectangular and cylindrical coordinate systems employed in this study have been superimposed on the theoretical geometry.

in the axial direction. As a consequence of this z independence, Maxwell's equations, written in cylindrical coordinates, separate into two independent sets, one for E_r, E_θ, B_z and the other for B_r, B_θ, E_z . The strip line mode corresponding to the TE_{10} mode used experimentally is a TEM mode with only $B_z \neq 0$, $E_y \neq 0$. Since the fields for $x \to \pm\infty$ must have $B_r = B_\theta = E_z = 0$, these field components will be identically zero everywhere. Thus the strip line problem requires the solution of only one second order equation involving B_z, E_r, and E_θ.

2.2 Cold plasma model

The calculations reported here were made using the "cold plasma" model. This model is based on the following assumptions:

i) The working frequency is large enough and the static magnetic field is low enough that only electron motion need be considered ($\omega >> \omega_{ci}, \omega_{pi}$) .

ii) The temperature is low enough that the hydrodynamic equations for the electrons can be completed by taking the pressure tensor terms to be negligible.

iii) There are small damping effects which can be completely described by introducing a constant "effective collision frequency" $\langle\nu\rangle$ for the electrons.

iv) The incident field strength is low enough that the resulting plasma response can be taken as a small perturbation on the equilibrium state, the continuous fluid description of the electron motion remains valid, and nonlinear terms may be neglected.

v) The plasma equilibrium state is current free, azimuthally symmetric, and axially homogeneous.

The second assumption is probably the least acceptable; however, it can be shown that the use of ii) has no first-order effects on the scattering properties beyond the loss of the Buchsbaum-Hasegawa fine structure and Landauer radiation. Assumption iv) is often ignored by virtue of the low power levels in typical microwave apparatus, but the present calculation indicates that even at modest power levels this assumption may fail. The validity of all these assumptions, with the exceptions of i) and v) which are quite reasonable on physical grounds, will be investigated in detail in Chapter 4.

In the equations that follow, all quantities are taken as sums of a time-independent, zeroth-order, equilibrium term and a small perturbation with time dependence $e^{i\omega t}$ and a complex amplitude which is a function of r and θ. Under the assumptions stated above, the plasma response is described by the simplified hydrodynamic equations for the electrons:

$$i\omega n + N\frac{\partial v_r}{\partial r} + \frac{v_r}{r}N + \frac{N}{r}\frac{\partial v_\theta}{\partial \theta} + v_r\frac{\partial N}{\partial r} = 0 \qquad (2.1a)$$

$$i\omega v_r + \frac{e}{m}(E_r + v_\theta B_0) = -\langle\nu\rangle v_r \qquad (2.1b)$$

$$i\omega v_\theta + \frac{e}{m}(E_\theta - v_r B_0) = -\langle\nu\rangle v_\theta \qquad (2.1c)$$

where $N(r)$ is the equilibrium electron density; B_0 is the static magnetic field strength; m is the electron mass; e is the magnitude

of the electron charge; $n(r,\theta)$ is the amplitude of the perturbation in the electron density; $v_r(r,\theta)$ and $v_\theta(r,\theta)$ are the amplitudes of the electron velocity perturbations; and $E_r(r,\theta)$ and $E_\theta(r,\theta)$ are the amplitudes of the electric field components. In polar coordinates Maxwell's equations can be written:

$$\frac{\partial}{\partial r}(rE_\theta) - \frac{\partial E_r}{\partial \theta} = -i\omega r B_z \tag{2.1d}$$

$$\frac{1}{r}\frac{\partial B_z}{\partial \theta} = -\mu_o N e v_r + \frac{i\omega}{c^2} E_r \tag{2.1e}$$

$$\frac{\partial}{\partial r}(rE_r) + \frac{\partial E_\theta}{\partial \theta} = -\frac{r}{\epsilon_0} en \tag{2.1f}$$

$$-\frac{\partial B_z}{\partial r} = -\mu_o N e v_\theta + \frac{i\omega}{c^2} E_\theta \tag{2.1g}$$

where B_z is the perturbation in the magnetic field, the current densities have been linearized, and $B_r = B_\theta = E_z = 0$ as mentioned in Section 2.1.

Eliminating the redundant equation and taking n as defined by Eqn. (2.1f) reduces the system to:

$$\begin{aligned}
&(i\omega + \langle\nu\rangle)v_r + \omega_c v_\theta = -\frac{e}{m} E_r \\
&-\omega_c v_r + (i\omega + \langle\nu\rangle) v_\theta = -\frac{e}{m} E_\theta \\
&\frac{\partial}{\partial r}(rE_\theta) - \frac{\partial E_r}{\partial \theta} = -i\omega r B_z \\
&\frac{1}{r}\frac{\partial B_z}{\partial \theta} = -\mu_o N e v_r + \frac{i\omega}{c^2} E_r \\
&-\frac{\partial B_z}{\partial r} = -\mu_o N e v_\theta + \frac{i\omega}{c^2} E_\theta
\end{aligned} \tag{2.2}$$

where $\omega_c = \frac{eB_0}{m}$ is the electron-cyclotron frequency. The algebraic relations for v_r and v_θ may be solved and the result substituted into the remaining differential equations. Separating variables (writing all quantities in the form $\sum_{m=-\infty}^{\infty} f_m(r)e^{-im\theta}$) and transforming to dimensionless form gives the usual cold-plasma equations:

$$\begin{aligned}
&\frac{d}{d\xi}(\xi E_{\theta m}) + im E_{rm} = -i\xi\, cB_{zm} \\
&mcB_{zm} = -\xi[K_\perp E_{rm} + iK_x E_{\theta m}] \qquad (2.3) \\
&\frac{dcB_{zm}}{d\xi} = -[K_x E_{rm} + iK_\perp E_{\theta m}]
\end{aligned}$$

where the following dimensionless parameters have been introduced:

ξ normalized coordinate, $= \frac{\omega}{c} r = k_0 r$

Ω_c normalized cyclotron frequency, $= \omega_c/\omega$

$\Omega_p^2(\xi)$ normalized plasma density, $= \frac{n(\xi)e^2}{\varepsilon_0 m\omega^2}$

Γ normalized collision parameter, $= \langle\nu\rangle / \omega$

$K_\perp$ dielectric tensor component, $= 1 + \frac{\Omega_p^2(\xi)(1 - i\Gamma)}{[\Omega_c^2 - (1 - i\Gamma)^2]}$

K_x dielectric tensor component, $= \frac{\Omega_c\, \Omega_p^2(\xi)}{[\Omega_c^2 - (1 - i\Gamma)^2]}$

As no analytic solutions to Eqns. (2.3) exist for realistic density profiles, numerical methods must be employed. Since Eqns. (2.3) are given as a first-order set and yield the fields in the plasma, they were used as they stand in the numerical solution.

2.3 Plane wave boundary conditions

Since Eqns. (2.3) are equivalent to one second-order equation, a well-posed problem requires two independent boundary conditions. One boundary condition is regularity of the solution at the origin and the second follows from the "radiation condition" that all energy incident from ∞ be from an external source. In this section the second condition will be developed for the problem of a plasma column illuminated by an incident plane wave. These results will be used in the treatment of the strip line problem in Section 2.4.

External to the plasma column the field is composed of the incident plane wave plus some scattered waves as shown in Fig. 2.2. The radiation condition in this case becomes a requirement that the scattered wave have outward-directed Poynting's vector. In cylindrical coordinates, solutions to Maxwell's equations with this property are outward-propagating "cylindrical waves", linear combinations of $H_m^{(2)}(\xi)e^{-im\theta}$ where $H_m^{(2)}(\xi)$ is the Hankel function of the second kind. Expanding the incident plane wave in angular modes and taking the incident field strength as unity yields:

$$cB_z^{ext}(\xi,\theta) = \sum_{m=-\infty}^{\infty} [i^{-m}J_m(\xi) + s_m H_m^{(2)}(\xi)]\, e^{-im\theta}$$

$$E_r^{ext}(\xi,\theta) = -\frac{i}{\xi}\frac{\partial}{\partial\theta}\,(cB_z^{ext}(\xi,\theta))$$

$$E_\theta^{ext}(\xi,\theta) = i\,\frac{\partial}{\partial\xi}\,(cB_z^{ext}(\xi,\theta))$$

where s_m is the scattering coefficient for the m^{th} angular mode, J_m is the Bessel function of the first kind, and B_z^{ext}, E_r^{ext}, and

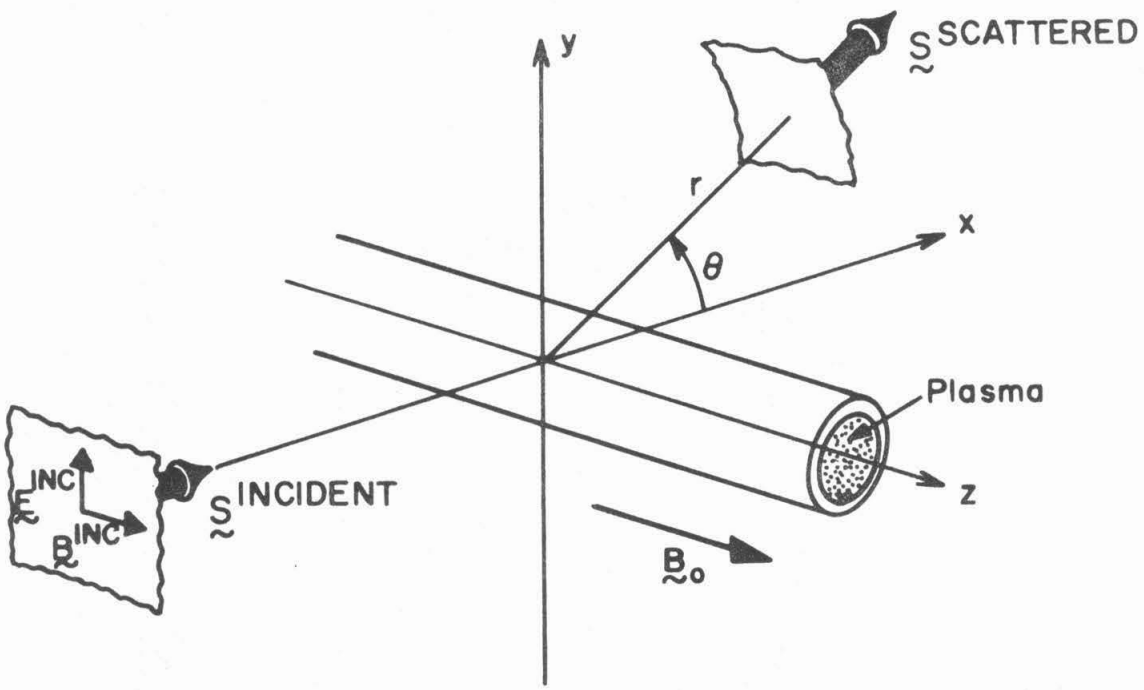

Fig. 2.2 Geometry of a plane wave scattering problem. Local Poynting vectors and segments of the wavefronts are indicated for the incident and scattered waves.

E_θ^{ext} are the total fields in the region outside the column. The s_m's contain all the information necessary to characterize the plasma's external response. As a result of the orthogonal property of $e^{-im\theta}$ the boundary conditions for each mode are independent, so sums over m and the $e^{-im\theta}$ factors will be dropped.

To get the boundary conditions at the plasma surface, the external solution must be extended through the glass wall surrounding the plasma column. Within the glass wall the fields are:

$$
\begin{aligned}
cB_{zm}^{glass}(\tilde{\xi}) &= A_m J_m(\tilde{\xi}) + B_m Y_m(\tilde{\xi}) \\
E_{rm}^{glass}(\tilde{\xi}) &= -\frac{m}{K_g \xi} cB_{zm}^{glass}(\tilde{\xi}) = -\frac{m}{n_g \tilde{\xi}} cB_{zm}^{glass}(\tilde{\xi}) \\
E_{\theta m}^{glass}(\tilde{\xi}) &= \frac{i}{K_g}\frac{d}{d\xi}[cB_{zm}^{glass}(\tilde{\xi})] = \frac{i}{n_g}\frac{d}{d\tilde{\xi}}[cB_{zm}^{glass}(\tilde{\xi})]
\end{aligned}
\tag{2.5}
$$

where $\tilde{\xi} \equiv n_g \xi$, $n_g = \sqrt{K_g} = \sqrt{\frac{\varepsilon_{glass}}{\varepsilon_o}}$ is the refractive index of the glass and Y_m is the Bessel function of the second kind. At the outer glass boundary there are the usual boundary conditions in the absence of surface currents:

$$
\begin{aligned}
\varepsilon_o E_{rm}^{ext}(\xi_t) &= \varepsilon_o K_g E_{rm}^{glass}(\tilde{\xi}_t) = D_{rm}^{glass}(\tilde{\xi}_t) \\
E_{\theta m}^{ext}(\xi_t) &= E_\theta^{glass}(\tilde{\xi}_t) \\
cB_{zm}^{ext}(\xi_t) &= cB_{zm}^{glass}(\tilde{\xi}_t)
\end{aligned}
\tag{2.6}
$$

where $\xi_t = k_o r_t$ and $\tilde{\xi}_t = n_g k_o r_t$.

The condition on $\mathcal{D}_{rm}$, the radial component of the electric displacement, is redundant with the one on cB_{zm} and will be dropped. Substituting Eqn. (2.5) into Eqns. (2.6) gives:

$$A_m J_m(\tilde{\xi}_t) + B_m Y_m(\tilde{\xi}_t) - s_m H_m^{(2)}(\xi_t) = i^{-m} J_m(\xi_t)$$

$$\frac{A_m}{n_g} J'_m(\tilde{\xi}_t) + \frac{B_m}{n_g} Y'_m(\tilde{\xi}_t) - s_m H_m^{(2)'}(\xi_t) = i^{-m} J'_m(\xi_t) \qquad (2.7)$$

where primes represent derivatives with respect to the arguments of the primed function.

The linearity of the field equations and the boundary condition at the origin determine the field solutions within the plasma up to a multiplicative constant. Thus, in the plasma, solutions which satisfy both boundary conditions can be expressed as follows:

$$cB_{zm}^{int}(\xi) = D_m \, \tilde{cB}_{zm}(\xi)$$

$$E_{rm}^{int}(\xi) = D_m \, \tilde{E}_{rm}(\xi)$$

$$E_{\theta m}^{int}(\xi) = D_m \, \tilde{E}_{\theta m}(\xi)$$

where D_m is a normalizing constant and $\tilde{B}_{zm}$, $\tilde{E}_{rm}$, $\tilde{E}_{\theta m}$ are any* set of solutions to Eqns. (2.3) which are regular at the origin. The boundary conditions on cB_{zm}^{int} and $E_{\theta m}^{int}$ at the plasma surface can be written:

---

*In particular the numerical integration of Eqns. (2.3) from the origin outwards yields such a set.

$$A_m J_m(\tilde{\xi}_w) + B_m Y_m(\tilde{\xi}_w) - D_m c\tilde{B}_{zm}(\xi_w) = 0$$

$$A_m J'_m(\tilde{\xi}_w) + B_m Y'_m(\tilde{\xi}_w) - D_m n_g C_m \, c\tilde{B}_{zm}(\xi_w) = 0 \qquad (2.8)$$

where $C_m \equiv \dfrac{-i\tilde{E}_{\theta m}(\xi_w)}{cB_{zm}(\xi_w)} = \left[\dfrac{K_\perp}{K_\perp^2 - K_X^2}\right]\left[\dfrac{1}{\tilde{cB}_{zm}(\xi_w)}\right]\dfrac{d}{d\xi}\left[cB_z(\xi_w)\right] + \dfrac{mK_X}{\xi_w K_\perp}\Bigg]$.

The redundant condition on the radial electric displacement has again been dropped. Since A_m and B_m are not of interest, they may be eliminated algebraically from Eqns. (2.7) and (2.8) yielding:

$$\left\{C_m + \left[J_m(\tilde{\xi}_t)\,\frac{2}{\pi u \tilde{\xi}_w} - J'_m(\tilde{\xi}_w)\right]\frac{1}{n_g J_m(\tilde{\xi}_w)}\right\} c\tilde{B}_{zm}(\xi_w)\, D_m$$

$$- \frac{2}{\pi n_g \tilde{\xi}_w u}\, H_m^{(2)'}(\xi_t) s_m = \frac{2i^{-m}}{\pi \tilde{\xi}_w\, n_g u}\, J_m(\xi_t) \qquad (2.9)$$

$$\left\{C_m + \left[J'_m(\tilde{\xi}_t)\,\frac{2}{\pi v\, \tilde{\xi}_w} - J'_m(\tilde{\xi}_w)\right]\frac{1}{n_g J_m(\tilde{\xi}_w)}\right\} c\tilde{B}_{zm}(\xi_w)\, D_m$$

$$- \frac{2}{\pi v\, \tilde{\xi}_w}\, H_m^{(2)'}(\xi_t)\, s_m = \frac{2i^{-m}}{\pi v\, \tilde{\xi}_w}\, J'_m(\xi_t)$$

where

$$u = J_m(\tilde{\xi}_w)\, Y_m(\tilde{\xi}_t) - J_m(\tilde{\xi}_t)\, Y_m(\tilde{\xi}_w)$$

$$v = J_m(\tilde{\xi}_w)\, Y'_m(\tilde{\xi}_t) - J'_m(\tilde{\xi}_t)\, Y_m(\tilde{\xi}_w)$$

Equation set (2.9) completes the solution of the plane wave problem given any set of solutions to Eqns. (2.3) which are regular at the origin.

2.4 Strip line boundary conditions

The scattering problem in the strip line will be treated by the image method. While this method is exact in principle, it requires the solution of an infinite set of linear equations. For all cases tested in this study, the solutions could be easily obtained to better than the accuracy of the numerical solutions of Eqns. (2.3).

First, consider the image problem for a single conducting plane located, for convenience, below the column. Since an incident plane wave satisfies the boundary condition on any conducting plane perpendicular to the y-axis, it is only necessary to develop the boundary conditions for the scattered fields emitted by the plasma column and its images. To solve this problem only one image column need be introduced as shown in Fig. 2.3. The fields radiated by the image column must combine with the fields radiated by the original column to satisfy the boundary condition for the conducting plane. The condition that tangential $\underset{\sim}{E}$ vanish will be satisfied if the following relations hold:

$$\begin{aligned} E_r^M(r,\theta) &\equiv - E_r^R(r,-\theta) \\ E_\theta^M(r,\theta) &\equiv E_\theta^R(r,-\theta) \end{aligned} \qquad (2.10a)$$

where the superscripts M and R denote the mirror image and the real column respectively. Equations (2.10a) and Maxwell's equations require:

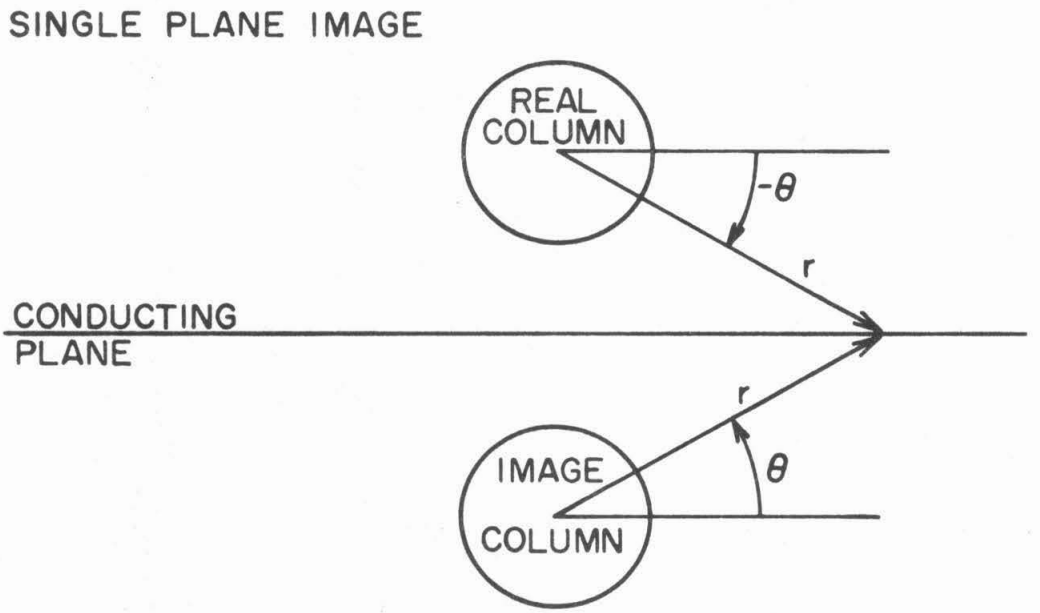

Fig. 2.3 Image Geometry for a cylindrical column and a single conducting plane

$$B_z^M(r,\theta) \equiv B_z^R(r,-\theta) \tag{2.10b}$$

These identities can be interpreted as a scheme for obtaining the components of the fields radiated from the mirror image column at an observation point (r,θ) relative to the center of the image column in terms of the expressions for the field radiated from the real column at an observation point $(r,-\theta)$ relative to the center of the real column. The conditions on E_z, B_r, and B_θ have been omitted since these field components are identically zero in the strip line problem.

The introduction of the second conducting plane above the real column to complete the strip line requires the introduction of two additional image columns above the real column, the upper of which is identical to the real column; however, the lower conducting plane requires that the additional image columns be themselves imaged below the original image column and then these new images require further images above the real column and so forth. Hence, the introduction of one additional conducting plane results in an infinite number of image columns, which are alternately real and mirror images of the original column. The complete image problem geometry is indicated in Fig. 2.4, where ℓ is an index which refers to the column at $y = \ell b$. Thus (ξ_ℓ,θ_ℓ) gives the coordinates of the observation point in a cylindrical coordinate system centered on the ℓ^{th} column. In the analysis that follows only $cB_z(\xi,\theta)$ will be considered, since the other field components may be derived via Maxwell's equations.

Physically, the scattered fields must be translationally invariant under $\ell' = \ell \pm 2n$ which implies that the scattered fields

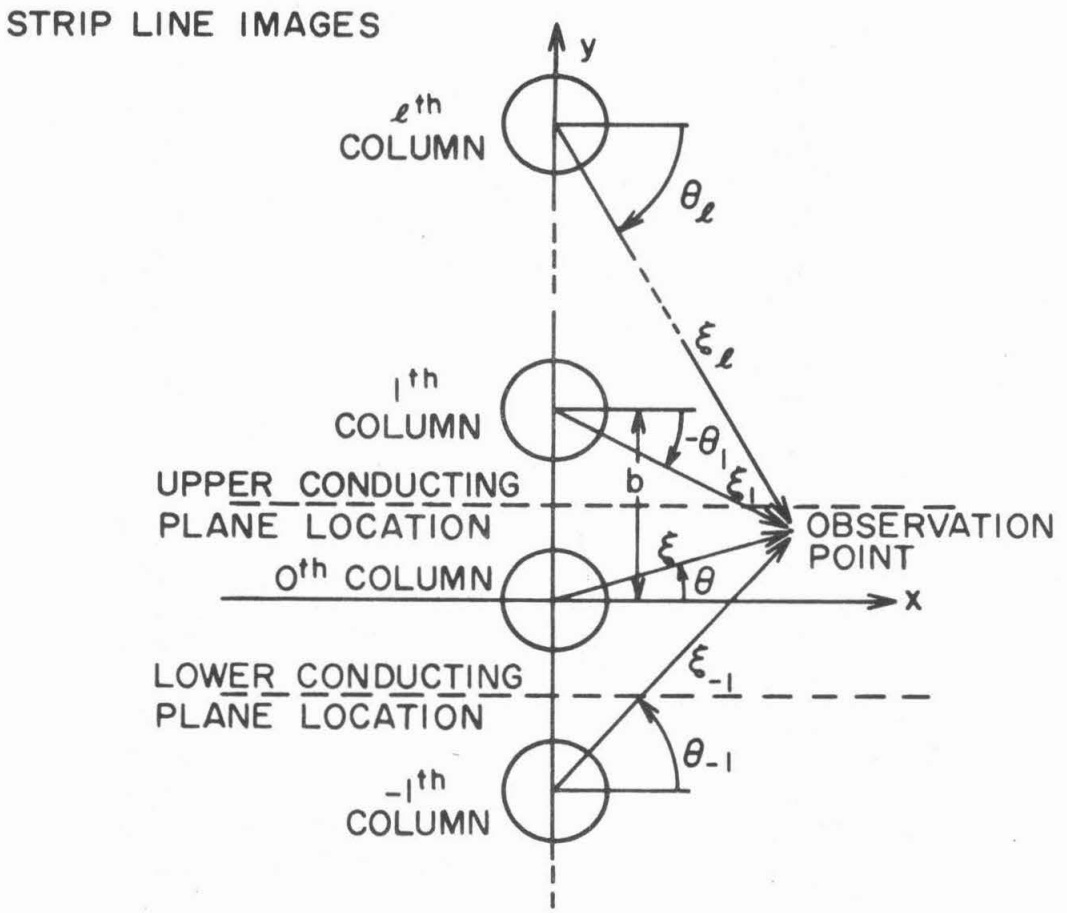

Fig. 2.4 Image geometry for a cylindrical column and two conducting planes

from each of the real-image columns, and each of the mirror-image columns, must be identical in the respective column-centered coordinate systems. As will be shown below, the radiation condition for the entire array will be satisfied if the scattered fields in the column-centered coordinates are linear combinations of outward-propagating cylindrical waves. Thus the total scattered field will be given by:

$$cB_z^{scatt}(\xi,\theta) = \sum_{\ell_{odd}=-\infty}^{\infty}\left[\sum_{m=-\infty}^{\infty} S_m^M H_m^{(2)}(\xi_\ell)e^{-im\theta_\ell}\right]$$

$$\sum_{\ell_{even}=-\infty}^{\infty}\left[\sum_{m=-\infty}^{\infty} S_m^R H_m^{(2)}(\xi_\ell)e^{-im\theta_\ell}\right] \qquad (2.11)$$

where the $S_m^{R,M}$ are the scattering coefficients for any real or mirror column in the array.

On the surface of the zeroth column the total scattered field can be expressed as the sum of the zeroth-column scattered field (the $\ell = 0$ term in the even sum) and the interaction field (all the rest) representing the field incident on the zeroth column due to all the other columns. Employing the addition theorem for Hankel functions:

$$H_m^{(2)}(\xi_\ell)\ e^{im\phi} = \sum_{n=-\infty}^{\infty} J_n(\xi_0)\ H_{n+m}^{(2)}(k_0\ell b)\ e^{in\psi} \qquad (2.12)$$

with $\phi = \frac{\pi}{2} + \theta_\ell$, $\psi = \frac{\pi}{2} - \theta_0$ for $\ell > 0$ and $\phi = \frac{\pi}{2} - \theta_\ell$, $\psi = \theta_0$ for $\ell < 0$; gives the expansion of the interaction field in cylindrical coordinates centered on the zeroth column when $\xi_o < k_0\ell b$. Using Eqn. (2.12) and suppressing the zero subscript on the coordinates yields:

$$cB_z^{scatt}(\xi,\theta) = \sum_{m=-\infty}^{\infty} S_m^R H_m^{(2)}(\xi)\, e^{-im\theta} + cB_z^{interaction}(\xi,\theta) \quad (2.13)$$

where

$$cB_z^{interaction}(\xi,\theta) = \sum_{m=-\infty}^{\infty}\Bigg[\sum_{n_{even}=-\infty}^{\infty} 2i^n (S_{n+m}^m\, h_n^m + S_{n+m}^R\, h_n^R)\Bigg] i^m J_m(\xi)\, e^{-im\theta},\ \xi < k_0 b\ ;$$

and

$$h_n^m = \sum_{\ell=1}^{\infty} H_n^{(2)}((2\ell-1)k_0 b) \quad ; \quad h_n^R = \sum_{\ell=1}^{\infty} H_n^{(2)}(2\ell k_0 b) \quad .$$

(rapidly convergent forms for the $h_n^{M,R}$ are given in Appendix B). Thus the total external field at the surface $\xi = \xi_t$ of zeroth column may be written as:

$$cB_z^{ext}(\xi_t,\theta) = \sum_{m=-\infty}^{\infty}\Bigg\{\Big[\, 1 + 2 \sum_{n_{even}=-\infty}^{\infty} i^n (S_{n+m}^M\, h_n^M + S_{n+m}^R\, h_n^R)\,\Big] \times\ i^m J_m(\xi_t) + S_m^R H_m^{(2)}(\xi_t)\Bigg\}\ e^{-im\theta} \quad (2.14)$$

Using the linearity of the plasma response, the problem can be expressed in terms of the plane wave coefficients. The plane wave results can be written as:

$$s_m = A_m i^m J_m(\xi_t)\ ;$$

and thus, since the plasma response is linear,

$$S_m^R = A_m \Big[\, 1 + 2 \sum_{n_{even}=-\infty}^{\infty} i^n (S_{n+m}^M\, h_n^M + S_{n+m}^R\, h_n^R)\,\Big] i^m J_m(\xi_t)\ ;$$

or, in terms of the s_m

$$S_m^R = s_m \left[1 + 2 \sum_{n_{even}=-\infty}^{\infty} i^n (S_{n+m}^M h_n^M + S_{n+m}^R h_n^R)\right] \tag{2.15}$$

Finally, it is necessary to eliminate the S_n^M in Eqns. (2.15) in order to arrive at a consistent set of equations. This can be accomplished by noting that the definition of the image-column fields, Eqns (2.10a,b) requires that

$$S_m^M = (-1)^m S_{-m}^R \tag{2.16}$$

Utilizing Eqn. (2.16), the bracketed quantity in Eqn. (2.15) may be reduced to an expression in S_m^R only. The result of this substitution is, dropping the superscript R on S_m^R :

$$S_m = \begin{cases} s_m \left[1 + 2 \sum_{n_{even}=-\infty}^{\infty} i^n S_n (h_{n-m}^R + h_{n+m}^M)\right] & , \text{m even} \\ s_m \left[1 - 2 \sum_{n_{odd}=-\infty}^{\infty} i^n S_n (h_{n-m}^R + h_{n+m}^M)\right] & , \text{m odd} \end{cases} \tag{2.17}$$

Equations (2.17) constitute an infinite set of simultaneous linear equations for the S_m , and thus there may be convergence problems, especially as the h_m increase with increasing $|m|$. In practice, it has been found that the error in truncating Eqns. (2.17) to order m is roughly the same as the error in truncating the series for the plane wave cross sections to the same order, and no attempt has been made to discover analytic estimates for the truncation errors.

There remains the problem of expressing the reflection and absorption coefficients in terms of the S_m . Equation (2.11) may be

rewritten in the following form by adding and subtracting the same quantity:

$$cB_z^{scatt}(\xi,\theta) = \sum_{\ell_{even}=-\infty}^{\infty}\left[\sum_{m=-\infty}^{\infty}(S_m - (-1)^m S_{-m})\, H_m^{(2)}(\xi_\ell) e^{-im\theta_\ell}\right]$$

$$+ \sum_{\ell=-\infty}^{\infty}\sum_{m=-\infty}^{\infty}(-1)^m S_{-m}\, H_m^{(2)}(\xi_\ell)\, e^{-im\theta_\ell} \qquad (2.18)$$

It is useful to introduce the function:

$$G_m(\xi,\theta,y_0) = \sum_{\ell=-\infty}^{\infty} H_m^{(2)}(\xi_\ell)\, e^{-im\theta_\ell} \qquad (2.19)$$

where:

$$\xi_\ell = k_0\sqrt{x^2 + (y - \ell y_0)^2} \quad , \quad \theta_\ell = \tan^{-1}\left[(y - \ell y_0)/x\right]$$

and k_0x and k_0y are the Cartesian coordinates of the point (ξ,θ). Thus for $y_0 = b$, (ξ_ℓ,θ_ℓ) is, as previously, the observation point in the coordinate system centered on the ℓth column. Inverting the order of summation and noting that $G_m(\xi,\theta,y_0) = (-1)^m G_{-m}(\xi,-\theta,y_0)$, Eqn. (2.18) may be rewritten:

$$cB_z^{scatt}(\xi,\theta) = \sum_{m=-\infty}^{\infty}(S_m - (-1)^m S_{-m})\, G_m(\xi,\theta,2b)$$

$$+ \sum_{m=-\infty}^{\infty} S_m\, G_m(\xi,-\theta,b) \qquad (2.20)$$

The problem of evaluating the G_m has been solved by Dumery [22, 23,24] in several papers, and the following treatment is essentially his. The problem is simplified by the observation that there are raising and lowering operators for the G_m, given by:

$$\mathcal{L} = \frac{1}{k_0}\left[\frac{\partial}{\partial x} + i\,\frac{\partial}{\partial y}\right] = e^{i\theta}\left(\frac{\partial}{\partial \xi} + \frac{i}{\xi}\,\frac{\partial}{\partial \theta}\right) \tag{2.21}$$

It can be shown by direct calculation that $\mathcal{L}$ and $\mathcal{L}^*$ (the complex conjugate of $\mathcal{L}$) have the properties:

$$\mathcal{L}\left[H_m^{(1,2)}(\xi)\; e^{im\theta}\right] = -\,H_{m+1}^{(1,2)}\; e^{i(m+1)\theta}$$

$$\mathcal{L}^*\left[H_m^{(1,2)}(\xi)\; e^{im\theta}\right] = \;H_{m-1}^{(1,2)}\; e^{i(m-1)\theta}$$

By repeated application of $\mathcal{L}$, G_m can be expressed in terms of G_0 as follows:

$$\begin{aligned} G_m(\xi,\theta,y_0) &= (-1)^m(\mathcal{L})^m\, G_0(\xi,\theta,y_0), \qquad m > 0 \\ G_m(\xi,\theta,y_0) &= (\mathcal{L}^*)^{|m|}\, G_0(\xi,\theta,y_0), \qquad m < 0 \end{aligned} \tag{2.22}$$

The G_0 function can be reduced to a more tractable form by observing that

$$\left[\nabla^2 + k_0^2\right] \sum_{\ell=-\infty}^{\infty} H_0^2(\xi_\ell) = -\,4i\delta(x) \sum_{\ell=-\infty}^{\infty} \delta(y - \ell y_0) \tag{2.23}$$

Applying a Fourier cosine transformation to Eqn. (2.23) yields:

$$\left\{\frac{d^2}{dx^2} + \left[k_0^2 - \left(\frac{2\pi n}{y_0}\right)^2\right]\right\} a_n(x) = \frac{4i}{y_0}\,\delta(x)$$

where the $a_n(x)$ are the Fourier coefficients of G_0 , thus:

$$G_0(\xi,\theta,y_0) = \sum_{\ell=-\infty}^{\infty} a_n(x)\,\cos\left(\frac{2n\pi y}{y_0}\right) \tag{2.24}$$

Applying the appropriate radiation conditions at $x = \pm\infty$ and matching the solutions and the discontinuity in the derivative implied by the delta function at $x = 0$ yields:

$$a_n(x) = \frac{2}{y_0 k_n} e^{-ik_n|x|}, \qquad k_n^* = \sqrt{k_0^2 - (\frac{2\pi n}{y_0})^2} \tag{2.25}$$

The choice of a working frequency such that there is only one propagating mode implies that $k_n^2 < 0$ for $n \neq 0$ and thus the far field solutions reduce to the $n = 0$ term in the sum. Applying the raising operator defined in Eqn. (2.21) to the far field forms for G_0 and then taking $y = 0$ yields:

$$\begin{aligned} G_m(\xi,0,y_0) &\to i^m \frac{2}{k_0 y_0} e^{-ik_0 x}, \quad x \to +\infty \\ G_m(\xi,\pi,y_0) &\to (-1)^m i^m \frac{2}{k_0 y_0} e^{ik_0 x}, \quad x \to -\infty \end{aligned} \tag{2.26}$$

Substituting Eqn. (2.26) into the expression for the scattered field, Eqn. (2.20), results in:

$$cB_z^{scatt}(x,y) = \begin{cases} \frac{2}{k_0 b}\left[\sum_{m=-\infty}^{\infty} i^m S_m\right] e^{-ik_0 x}, & x \to +\infty \\ \frac{2}{k_0 b}\left[\sum_{m=-\infty}^{\infty} (-1)^m i^m S_m\right] e^{ik_0 x}, & x \to -\infty \end{cases} \tag{2.27}$$

Using these solutions the usual voltage reflection and transmission coefficients for a transmission line with perfectly matched termination (or infinite length) are:

$$\begin{aligned} r_{ML} &= cB_z^{scatt}(x \to -\infty) e^{ik_0 x} = -\frac{2}{k_0 b}\left[\sum_{m=-\infty}^{\infty} (-1)^m i^m S_m\right] \\ t_{ML} &= 1 + cB_z^{scatt}(x \to +\infty)\ e^{ik_0 x} = 1 + \frac{2}{k_0 b}\left[\sum_{m=-\infty}^{\infty} i^m S_m\right] \end{aligned} \tag{2.28}$$

As long as the plasma response is linear, these two complex coefficients completely define the properties of the plasma column in the strip line. Thus transmission and reflection coefficients for arbitrary termination conditions may be calculated directly from r_{ML} and t_{ML} if the strip line is long enough to allow the nonpropagating modes excited by the plasma to attenuate away. In particular, most of the experimentally measured absorption curves with which the results of this calculation will be compared were obtained by measuring the reflection from the column with a shorting plane at $x = (\frac{2n+1}{4})\lambda$. For this case the power absorption coefficient can be given by:

$$|a_{SL}|^2 = 1 - |r_{SL}|2 = 1 - |(t_{ML}^2 - r_{ML}^2 + r_{ML})/(1 - r_{ML})|^2 \tag{2.29}$$

III. Discussion of Cold Plasma Solutions

3.1 Introduction

Direct experimental verification of the fields and plasma perturbations which are predicted from the solutions of Eqns. (2.3) has not proved possible. Even so, these solutions are still of interest, both for the physical insights which they yield and as a basis for a posteriori evaluation of the approximations involved in the cold plasma model.

The discussion in this chapter is concerned with the general nature of the cold plasma behavior that is revealed by study of the solutions of Eqns. (2.3); hence, detailed results will be presented for only a few cases. The parameter values chosen are typical of those encountered in Stenzel's [15] experimental work. Equations (2.3) are linear so the strengths of the internal fields and plasma perturbations are proportional to the incident plane wave field strength E_0 , which has been assumed to be in volts/cm. The effects of the quartz tube containing the plasma have been included in the solutions presented in this section, but the strip line effects, which alter the solutions by less than 10% for the cases to be shown, have not been included. The plasma radius r_w and the tube radius r_t for the solutions depicted below are 5 and 6 mm respectively, and ω is 2×3.0 GHz, so $k_0 r \sim .3$.

3.2 Nature of the solutions for a typical case

The scattering properties of a small object ($k_0 r << 1$) are characteristically dominated by the behavior of the m=-1, 0, and +1

angular modes in cylindrical coordinates. The dominance of these three modes arises from two effects: first, the radiation efficiency of a small current distribution decreases with increasing $|m|$ and second, for any incident field distribution only the $m=\pm1$ modes can have nonzero field strength as $k_0 r \to 0$. In a magnetoplasma the electrons have a preferred direction of rotation and the plasma response will be enhanced for an exciting electric field which rotates with the electron. If $k_0 r \lesssim 1$ the incident field in angular modes with $m > 0$ rotates with the electrons, so for small columns with low peak densities the plasma response and the scattering are increasingly dominated by the $m=+1$ mode as Ω_c approaches cyclotron resonance. The results in this section were calculated for parameter values such that $\sim$ 90% of the plasma response appears in the $m=+1$ mode, so the solutions will be presented below for the $m=+1$ mode only.

The internal conditions predicted by the cold plasma theory are illustrated in Figs. 3.1-3 for $\omega_p^2(0) = .19\omega^2$, $\omega_c = .93\omega$ and $\langle\nu\rangle = 8.0 \times 10^{-4}\omega$. For this choice of parameters the radius r_1 at which the hybrid resonance condition will be satisfied is $.5r_w$. The plasma response is demonstrated by plots of the magnitude of the density perturbation $|n(r)|$ and the magnitudes of the electron fluid velocity components $|v_r(r)|$ and $|v_\theta(r)|$ in Figs. 3.1 and 3.2 respectively. The effect of the plasma on the internal electromagnetic fields is illustrated by plots of the magnitudes of the electric field components $|E_r(r)|$ and $|E_\theta(r)|$ in Fig. 3.3. All of the perturbations and fields are represented as complex functions of the radius

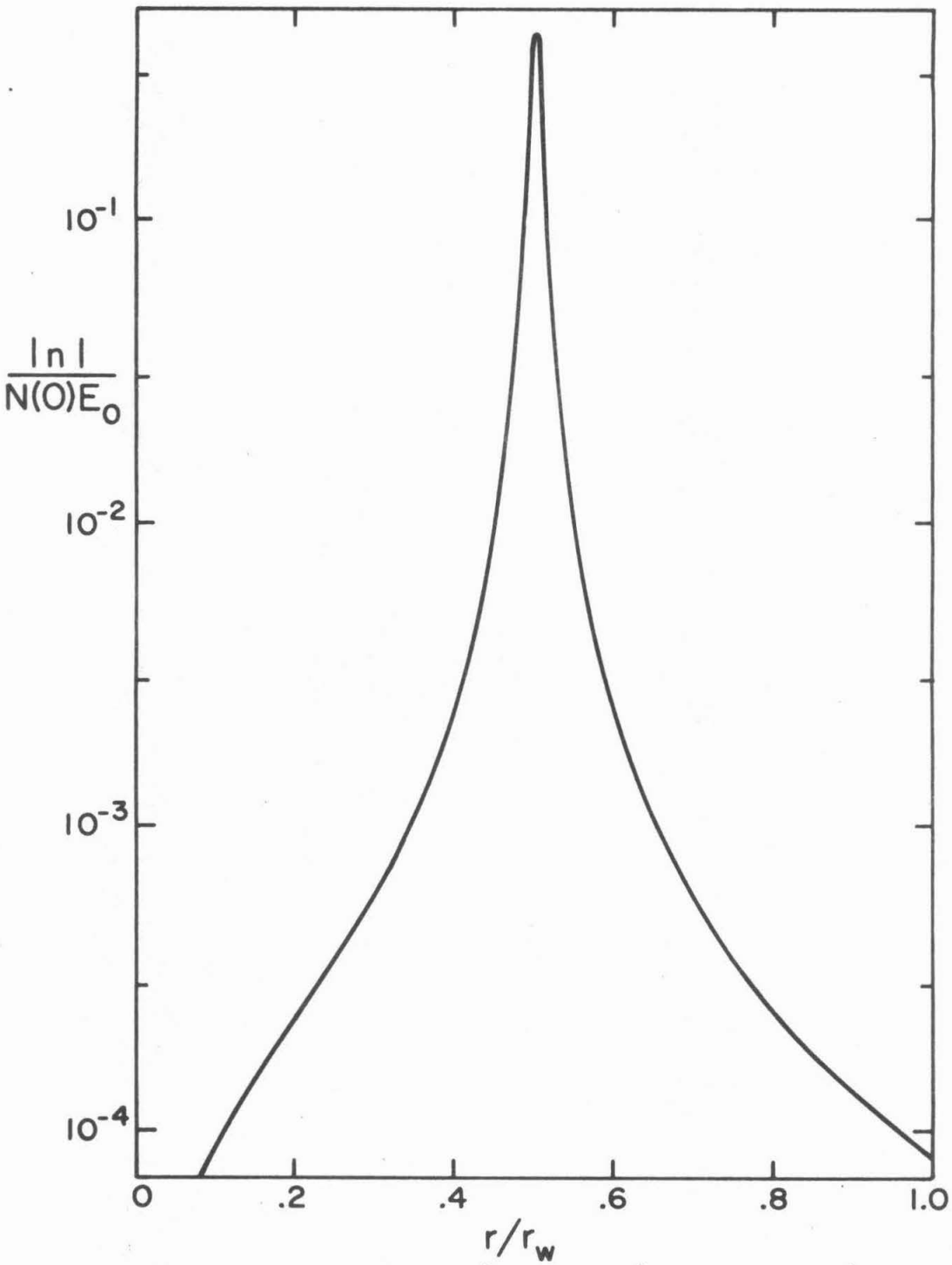

Fig. 3.1 Density perturbation, $\omega_p^2(0) = .19\omega^2$, $\langle\nu\rangle = 8\times 10^{-4}\omega$, $\omega_c = .93\omega$, $r_w = 0.5$ cm, and $\omega = 2\pi \times 3.0$ GHz. E_0 is the incident strength in V/cm (Note the vertical scale is in cm/volt).

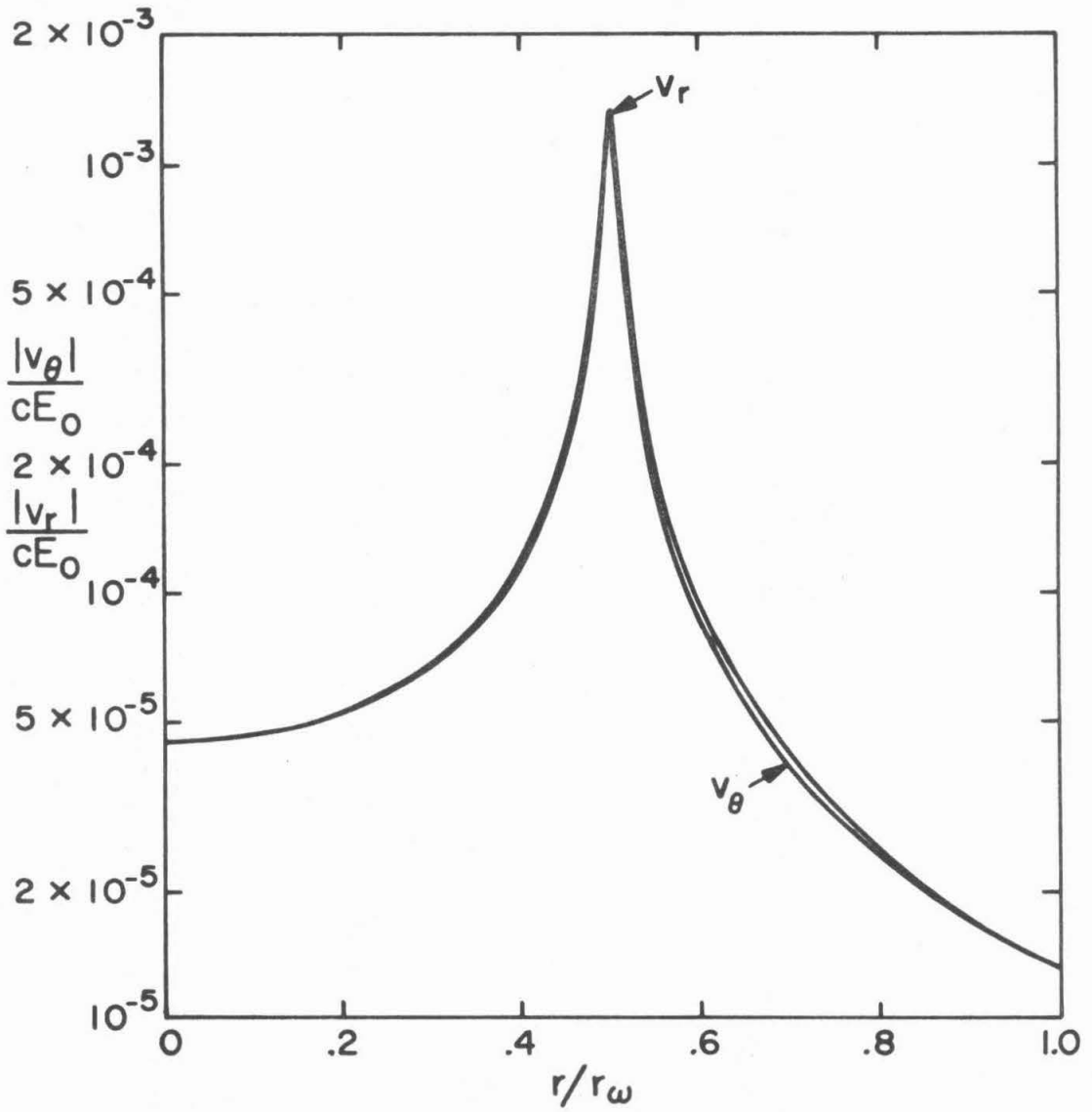

Fig. 3.2 Perturbed electron velocities; conditions as in Fig. 3.1

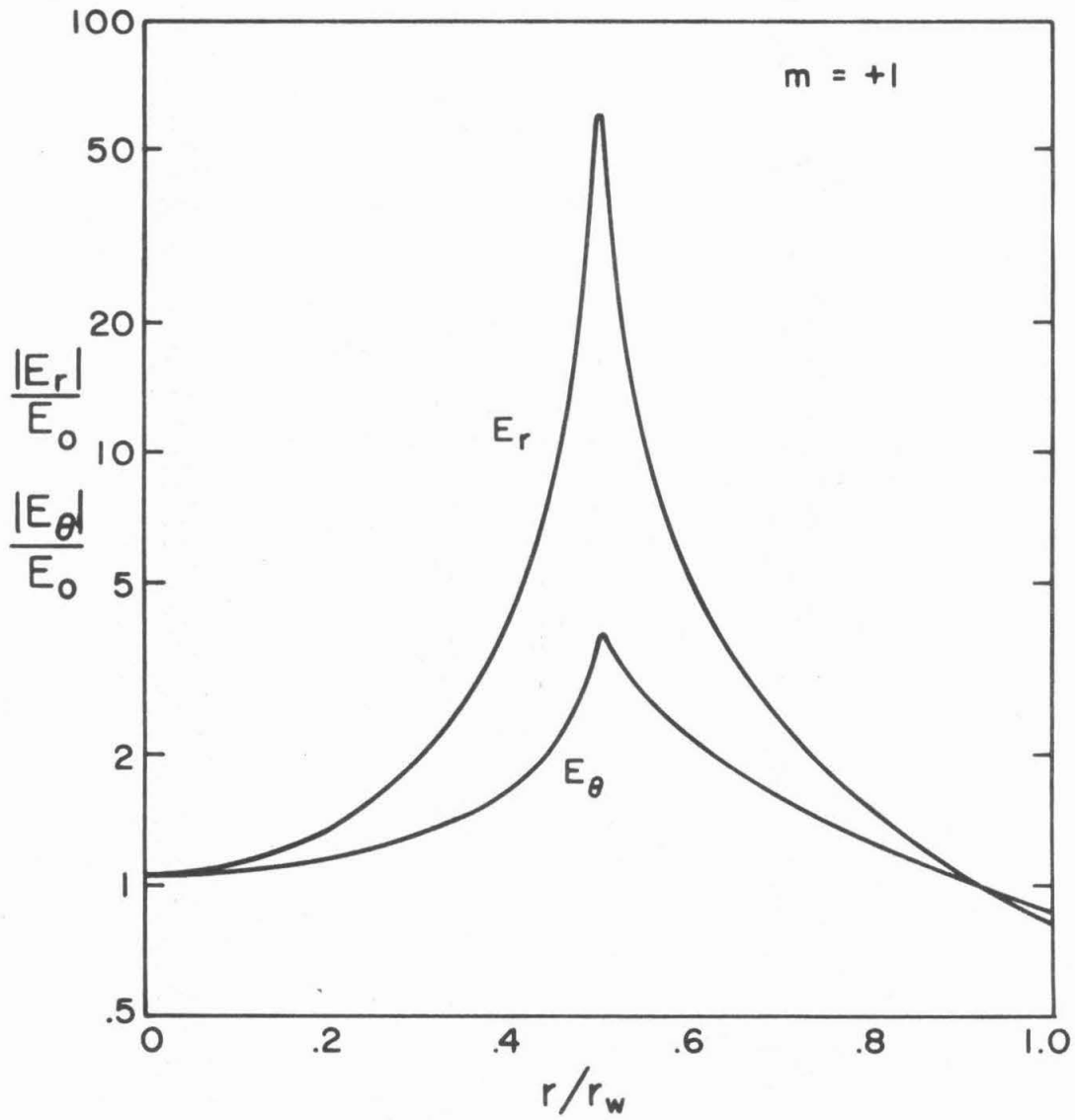

Fig. 3.3 Internal electric fields in the m = +1 mode; conditions as in Figs. 3.1 and 3.2. The vacuum m = +1 solution is $|E_r| \tilde{=} |E_\theta| \tilde{=} .5\ E_0$.

$f(r)$ multiplied by $e^{+i(\omega t - m\theta)}$, thus $|f(r)|$ gives the oscillation amplitude of the real physical quantity.

The most striking feature of the plasma response is the existence of a strong narrow resonant zone near r_1 which is the basis for characterizing the plasma as having a hybrid resonant layer. Thermal effects will modify this response, as will be discussed in Chapter 4, but it can be expected to remain strong for the temperatures encountered experimentally ($\kappa T_e < 1$ eV). Thus, the linearization of the cold plasma Eqns. (2.1), which requires $N >> |n|$, will set quite restrictive limits of the incident field strength. The strong hybrid response is also quite evident in the fields at r_1, and even away from r_1 the fields cannot be represented as small perturbations on the vacuum solutions. There is no evidence of the evanescent region predicted by the theory for a homogeneous plasma visible in the calculation shown in Figs. 3.1 - 3 or in any of the calculations carried out for this report.

The effect of changing the value of the damping is illustrated by the plots of $|E_r|$ shown in Fig. 3.4. As $<\nu>$ decreases the peak field at the hybrid layer increases approximately as $<\nu>^{-1}$, and the field outside a narrow region about the hybrid layer becomes independent of $<\nu>$. This behavior illustrates the existence of a collision-free limiting solution which is well behaved everywhere but at $r = r_1$. Since the scattering properties of the column are entirely determined by the solutions at $r = r_w$, the scattering will also exhibit a well defined collision-free limit.

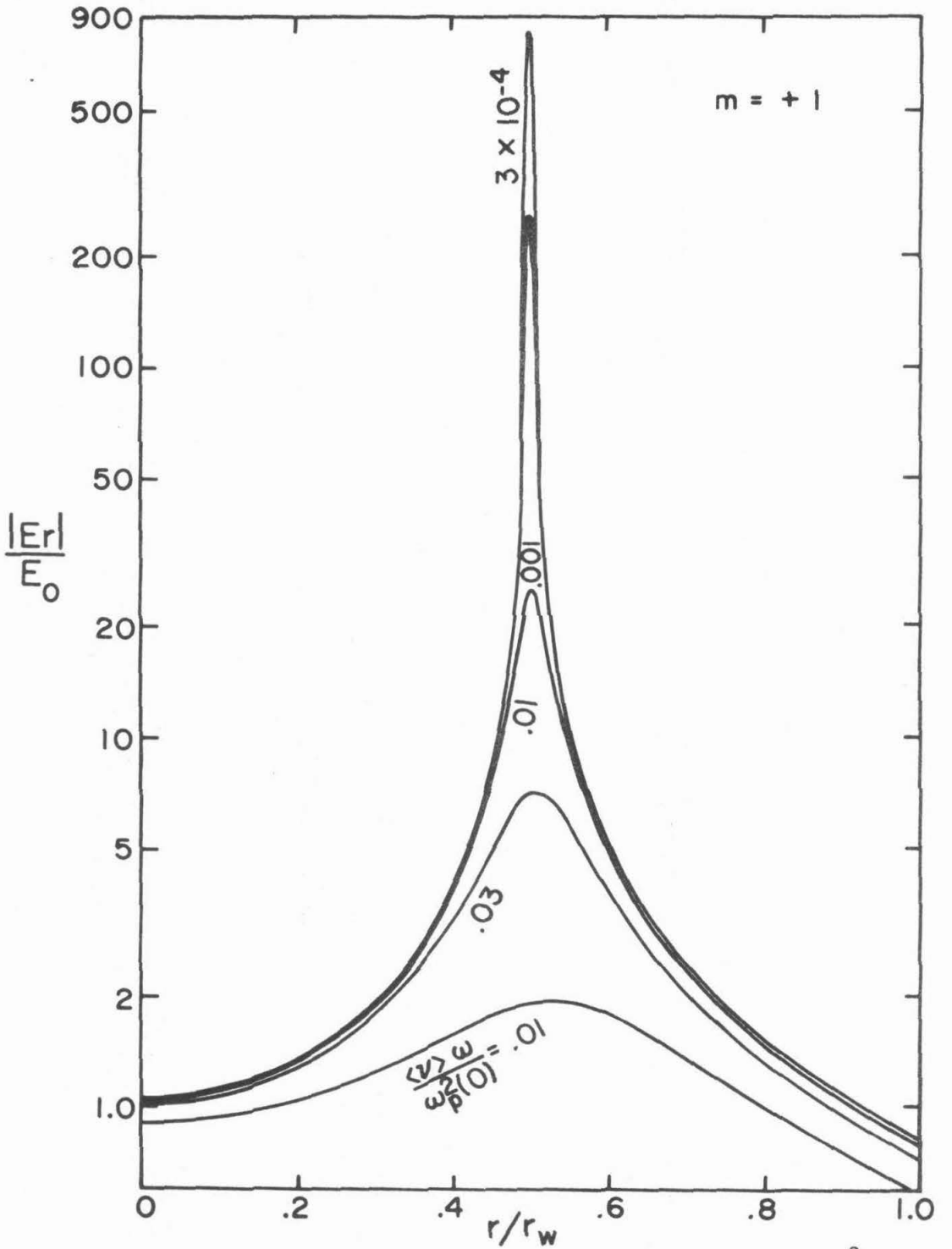

Fig. 3.4 Internal radial field for various values of $\langle\nu\rangle\omega/\omega_p^2(0)$; remaining parameters as in Figs. 3.1 - 3.3.

3.3 Some correlative experimental results

The local power absorption from the wave

$$P_{abs}(r) = -\frac{1}{4}\sqrt{\frac{\varepsilon_o}{\mu_o}}\frac{1}{r}\frac{d}{dr}\{r\ \mathrm{Re}[E_\theta\ cB_z^*]\}$$

presented in Fig. 3.5 is also of interested since the strong peak* at the hybrid layer suggests a possible interpretation of some experimental results. Kirchhoff's law states that the noise emission is proportional to the temperature and the absorptivity, thus the narrow band noise emission for center frequencies such that $\omega^2 \leq \omega_c^2 + \omega_{p\ max}^2$ should be dominated by emission from the electrons in a layer for which $\omega_p^2(r) \tilde{=} \omega^2 + \omega_c^2$. This suggests that a narrow band radiometer might respond to only a narrow spatial region in which the plasma density satisfies the hybrid condition for the radiometer center frequency.

Figure 3.6 shows the result of Stenzel's [15] measurement of the narrow band radiation temperature in a 1.0 cm radius experimental column as a function of ω_c for several afterglow times. At a fixed afterglow time the density should be only a weak function of magnetic

---

*The resonance in the absorption is a reflection of the form assumed for the damping since Eqns. (2.2) imply that $P_{abs}(r) = 2<\nu> N(r)U_p$ where U_p is the local particle energy $\frac{1}{4} m_e |\underset{\sim}{v}|^2$. While the approximations involved in this description of the damping effects are not too good, as will be discussed in Section 4.5, it seems unlikely that the absorptivity would not be enhanced in an excited region.

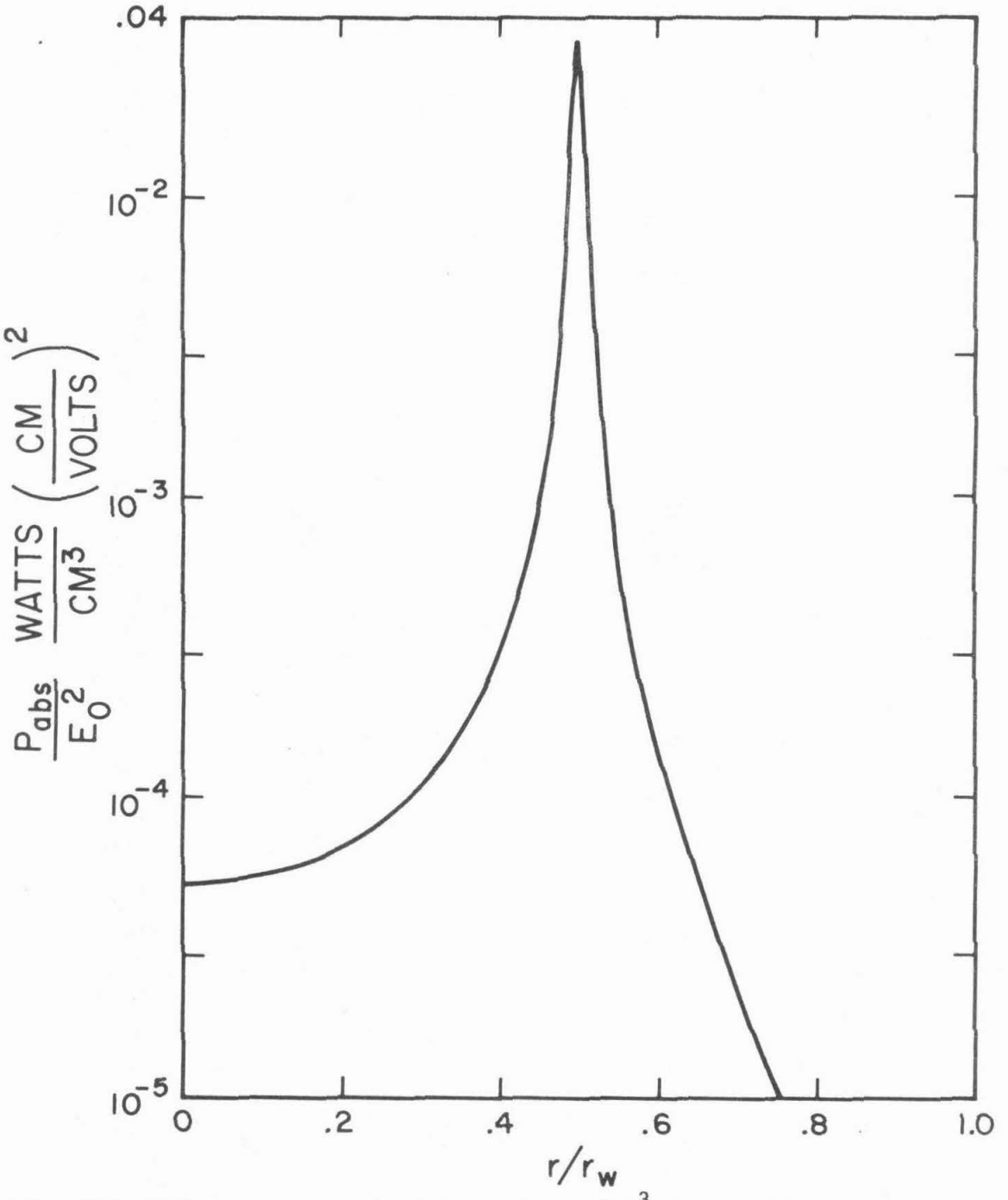

Fig. 3.5 Volume power absorption in watts/cm^3 for conditions as in Figs. 3.1 - 3.3. The peak absorption varies as $\langle\nu\rangle^{-1}$.

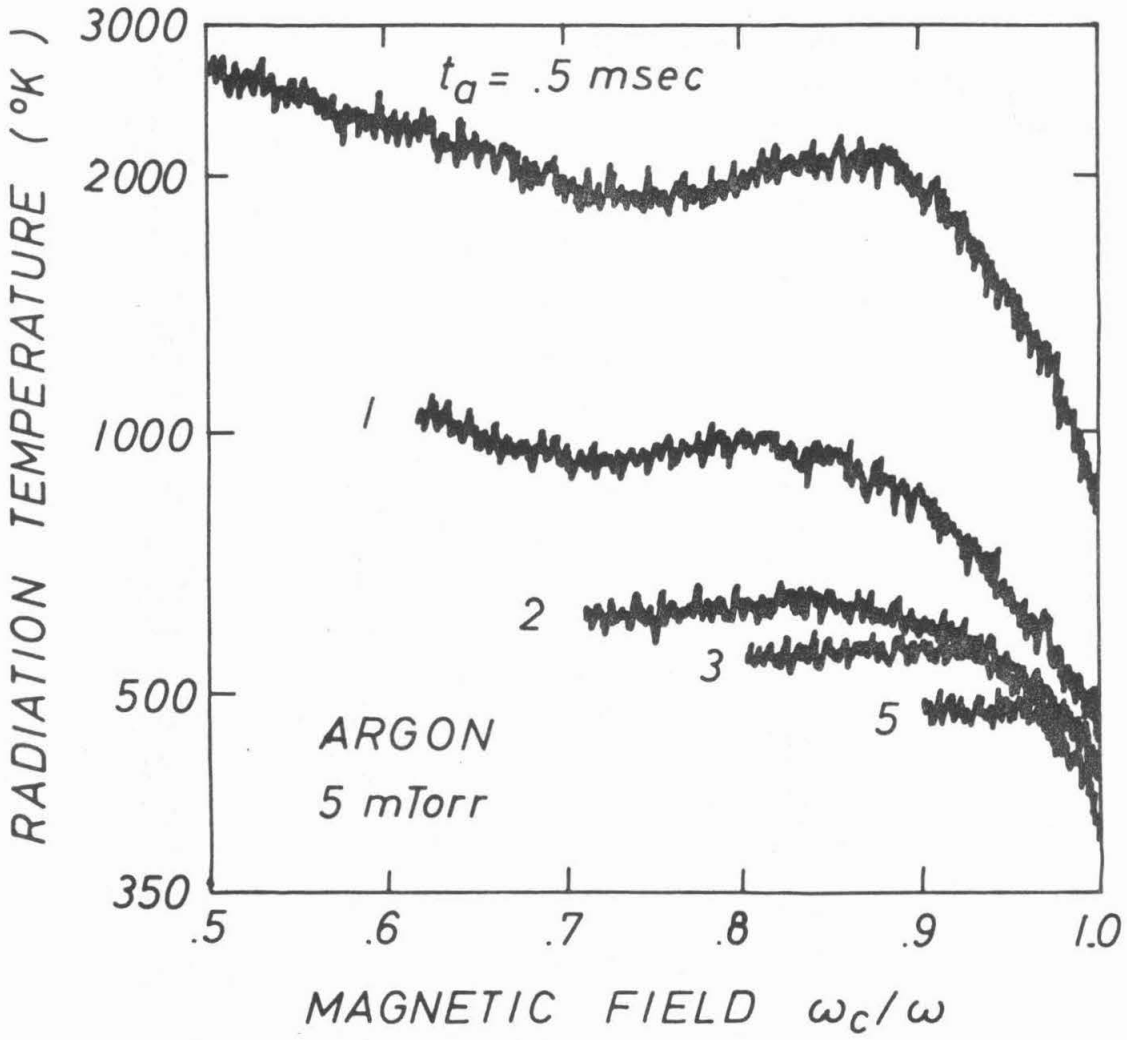

Fig. 3.6 Radiation temperature in argon versus normalized magnetic field at different afterglow times t_a. (2 cm column diameter) After Stenzel [15].

field, so changing Ω_c should alter only the radius at which the center frequency of the radiometer satisfies the hybrid resonance condition. Under this interpretation the cooling near $\Omega_c = 1$ can be explained by noting that, as Ω_c approaches one, the hybrid layer enters the cooler regions of the plasma near the wall.

A second set of experimental results can also be interpreted on the basis of the hybrid layer's existence. The plasma temperature was measured at various times after the decaying plasma had been excited by a short (500 μsec), low power (10 μW) heating pulse. The heating pulse frequency was such that it could excite a hybrid layer in the plasma and was applied at a fixed afterglow time and magnetic field. The radiometer center frequency and, assuming the interpretation developed above is correct, the radius that it senses was varied with the results shown in Fig. 3.7. The abscissa values for Fig. 3.7 were obtained by assuming a parabolic density profile and converting the radiometer frequency ω into a column radius via:

$$\frac{r}{r_w} = \left[\frac{\omega_p^2(0) + \omega_c^2 - \omega^2}{\omega_p^2(0)} \right]^{1/2}$$

where $\omega_p^2(0)$ is the maximum plasma frequency (assumed to be unaffected by the heating pulse). With this interpretation Fig. 3.7 suggests that the heating pulse strongly excites the electrons in a relatively narrow hybrid layer, and further, that the excited electrons cool without leaving the layer.

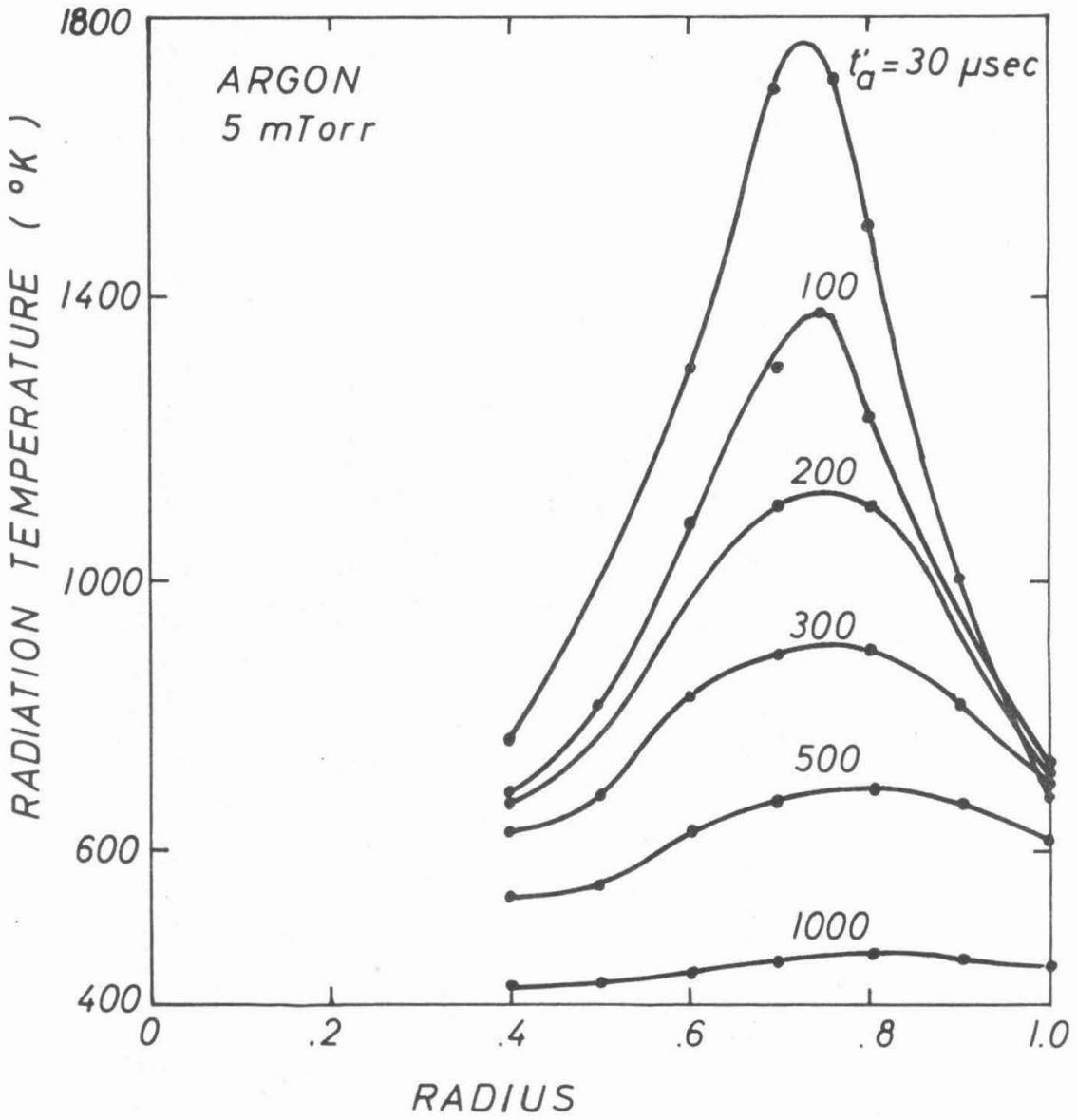

Fig. 3.7 Radiation temperature profiles of a heated afterglow plasma at different times t'_a after the end of the heating pulse. A parabolic radial density profile has been assumed. Other experimental parameters are the same as in Stenzel [15], Fig. 5.3.

IV. Discussion of Plasma Approximations

4.1 Introductory discussion of warm plasma effects and method of approach

An important feature of the cold plasma results presented in Chapter 3 is the strong plasma excitation in the hybrid layer. However, as a result of this strong localized excitation, the spatial gradients of the perturbations become large, and the neglect of the pressure tensor terms (which are $\sim \nabla nkT$) in the hydrodynamic equations (2.1) is questionable. The major result of including finite-temperature effects in a magnetoplasma is the introduction of the Bernstein [16] modes which can couple to the extraordinary electromagnetic mode at the hybrid layer (Ginzburg [25] , Stix [26] , Kuehl [27]).

In the warm plasma equations the highest derivatives have coefficients which are multiplied by T , so while the low-temperature equations can be formally recovered by setting $T = 0$, the warm plasma solutions represent singular perturbations on the solutions of the $T = 0$ equation. Thus there is no guarantee that the solutions of the low-temperature equations are small perturbations on the zero-temperature solutions on which this work is based.

In the following sections both the cold- and low-temperature plasma equations will be replaced by simplified models of the wave equations for E_θ valid near the hybrid layer. These model equations are soluble by analytic methods and the results will be compared to determine the validity of using cold-plasma solutions to describe the behavior of a low-temperature plasma. Thus this treatment is quite similar to those of Kuehl [27] , Tang [28], and Hedrick [29], all of

which were in one-dimensional geometry, but the emphasis here will be on establishing the usefulness of the cold-plasma solutions.

In order to present a single set of model equations it will be assumed that the plasma density and magnetic fields are such that the hybrid condition is satisfied somewhere in a region which is bounded away from both the origin and the column wall. Although these restrictions could be relaxed, it would not be particularly profitable to do so in either case. When the hybrid layer is near the origin, the Bernstein modes can set up standing-wave resonances (the Buchsbaum-Hasegawa fine structure) and the cold solutions are no longer valid. When the layer is near the wall several other assumptions fail; in particular, the complex question of the sheath structure in a magnetic field has been ignored in the choice of density profiles, and the assumption of purely perpendicular propagation ignores the possibility of coupling to strongly damped electron-cyclotron harmonic modes propagating parallel to the static magnetic field for $\Omega_c \gtrsim 1$.

Since the model equations for $m = 0$ are different from those for $m \neq 0$ and the cold plasma response is strongly dominated by the dipolar modes, the development below will treat only $m \neq 0$ unless noted. The $m = 0$ equations are very similar to the one-dimensional equations and lead to the same conclusions as result from considering the $m \neq 0$ equations.

4.2 Cold plasma theory near the hybrid singularity

In this section approximate solutions to the cold plasma equations near the hybrid layer will be developed by considering a model equation derived from the second-order equation for E_θ :

$$(K_\perp - \frac{m^2}{\xi^2})K_\perp E_\theta'' + \{\alpha'(\xi)\frac{m^2}{\xi^2} + \frac{K_\perp}{\xi}(K_\perp - \frac{3m^2}{\xi^2})\} E_\theta' +$$

$$\{\frac{m\alpha'(\xi)}{\xi}[\frac{m}{\xi^2}(1 + m\Omega_c) - \Omega_c] + \frac{m^2\Omega_c^2\alpha^2}{\xi^2} + \tag{4.1}$$

$$K_\perp[\frac{2m\Omega_c\alpha}{\xi^2} - K_\perp(\frac{2m^2+1}{\xi^2} - K_\perp) - \Omega_c^2\alpha^2 + \frac{m^2(m^2-1)}{\xi^4}]\} E_\theta = 0$$

which results from combining Eqns. (2.3). The dimensionless quantities $\alpha(\xi) \equiv 1 - K_\perp(\xi) = \Omega_p^2(\xi)(1 - i\Gamma) / [(1 - i\Gamma)^2 - \Omega_c^2]$ and $\Omega_c \equiv \Omega_c / (1 - i\Gamma) = -K_\times/\alpha$ have been introduced in order to write the dielectric tensor components with collisions in a convenient form.

When $\Gamma = 0$ the coefficient of E_θ'' in Eqn. (4.1) raises the possibility of singular points when $K_\perp(\xi) = 0$ and, for $m \neq 0$, also when $K_\perp(\xi) = m^2/\xi^2$. The first condition is the hybrid resonance condition and, for $m \neq 0$,* the transverse component exhibits singular behavior at the hybrid layer (Denisov [30], Dolgopolov [31]). The second condition does not yield a singularity in the solution as may be verified by considering the equation set (2.3) or the equivalent second-order equations for B_z or E_r.

Equation (4.1) can be simplified by expanding about the singular point ξ_1 where $\alpha(\xi_1) = 1.0$. When $\Gamma > 0$ the hybrid resonance occurs at a complex radius so the expansion about ξ_1 requires the extension of the radial variable into the complex plane in order to

---

*For $m = 0$ (or in a one-dimensional geometry) the transverse field component does not exhibit a singularity (Stix [9] pg. 242) in the collisionless case due to the infinite perturbation wavelength in the transverse direction.

treat collisions. Introducing the new independent variable $\zeta = \xi - \xi_1$ and assuming a density profile such that $\alpha(\zeta) = 1.0 + \zeta\alpha_1$, Eqn. (4.1) can be written:

$$E''_\theta + \frac{1}{\zeta} E'_\theta + \frac{1}{\zeta} \left\{ \left[\frac{(1 + m\Omega_c)}{\xi_1} - \frac{\xi_1 \Omega_c}{m} \right] + \frac{\Omega_c^2}{\alpha_1} \right\} E_\theta = 0 \qquad (4.2)$$

where it has been assumed that $\xi_1 >> |\zeta|$ and $|m^2/\alpha_1 \xi_1^2| >> |\zeta|$. For columns of small radius the second assumption is not restrictive for reasonable density gradients when the resonant layer is not close to the column wall.

The solutions of Eqn. (4.2) may be chosen as:

$$E_\theta = C_1 J_0(2A\sqrt{\zeta}) + C_2 H_0^{(2)}(2A\sqrt{\zeta}) \qquad (4.3)$$

where

$$A = \pm \left[\frac{1 + m\Omega_c}{\xi_1} - \frac{\xi_1 \Omega_c}{m} + \frac{\Omega_c^2}{\alpha_1} \right]^{1/2}$$

has been introduced for convenience. The choice of sign for A is unimportant and will be taken as positive. This form for E_θ can be used to obtain approximate expressions for the peak magnitudes of various quantities as functions of Γ for comparison with the numerical results reported previously. The physical solutions of Eqn. (4.2) are obtained by evaluating Eqn. (4.3) for ζ given by the mapping of the real ξ-axis onto the complex ζ-plane. Since ξ_1 has a positive imaginary part for $\Gamma > 0$, the "solution path" passes below the origin in the ζ-plane, and for low-damping the peak plasma response

will occur at, or very near*, the point of closest approach to the origin in the ζ-plane. Assuming a parabolic profile, the point of maximum response ζ_{max} is

$$\zeta_{max} = -i\ \mathrm{Im}(\xi_1) \tilde{=} - \frac{i\xi_w^2\ \Gamma(1 + \Omega_c^2)}{2\Omega_p^2(0)\ \mathrm{Re}[\xi_1]} \tag{4.4}$$

Substituting in Eqn. (4.3) and simplifying yields:

$$|E_\theta|_{max} \sim \frac{|C_2|}{\pi}\ \ell n\ \left|\frac{\Omega_p^2(0)}{\Gamma(1+\Omega_0^2)}\right| + |C_1| + \text{const.}$$

$$|E_r|_{max} \sim |E_\theta'|_{max} \sim |C_2| \cdot \left|\frac{\text{const}\ \Omega_p^2(0)}{(1+\Omega_c^2)}\right| \tag{4.5}$$

$$\text{when}\quad |E_r|_{max} >> |E_\theta|_{max}$$

which verifies the $<\nu>$ dependence exhibited by the numerical solution.

The explicit form of the connection formula for $\Gamma = 0$ will be useful for comparison with the warm plasma results of Section 4.3. Since, for $\Gamma > 0$, the solution path passes below the origin in the ζ-plane, the choice of $\arg\sqrt{\zeta} = 0$ on the low density side of the singular point implies that $\arg\sqrt{\zeta} = -\pi/2$ on the high density side and Eqn. (4.3) becomes

---

*The location of the maximum magnitudes of the various quantities shifts away from the collision-free hybrid point on the real ξ-axis when $\Gamma > 0$. For E_θ this shift is toward lower density and can be seen analytically by considering the solution path on the plot of $H_0^{(2)}(\sqrt{\zeta})$ such as is given in Jahnke and Emde [32].

$$C_1 I_0(2A\sqrt{-\zeta}) + \frac{2iC_2}{\pi} K_0(2A\sqrt{-\zeta}) \quad \leftrightarrow$$

$$C_1 J_0(2A\sqrt{\zeta}) + C_2 H_0^{(2)}(2A\sqrt{\zeta}) \tag{4.6}$$

where I_0 and K_0 are the modified Bessel functions.

4.3 Warm plasma theory near the hybrid turning point

Wave propagation in a low temperature, inhomogeneous, magnetoplasma has been dealt with a number of times using various approximations. In each case the approach has involved solving the linearized Boltzmann's equation

$$\frac{\partial \delta f}{\partial t} + \underset{\sim}{v} \cdot \underset{\sim}{\nabla}_{\underset{\sim}{v}} \delta f - \frac{e}{m} (\underset{\sim}{E}_0(\underset{\sim}{r}) + \underset{\sim}{v} \times \underset{\sim}{B}_0(\underset{\sim}{r})) \cdot \underset{\sim}{\nabla}_{\underset{\sim}{v}} \delta f$$

$$= \frac{e}{m}(\underset{\sim}{E}(\underset{\sim}{r},t) + \underset{\sim}{v} \times \underset{\sim}{B}(\underset{\sim}{r},t)) \cdot \underset{\sim}{\nabla}_{\underset{\sim}{v}} f + (\frac{\partial \delta f}{\partial t})_{\text{collisions}}, \tag{4.7}$$

where $f(\underset{\sim}{r},\underset{\sim}{v})$ is the equilibrium electron distribution function and $\underset{\sim}{E}_0(\underset{\sim}{r})$ and $\underset{\sim}{B}_0(\underset{\sim}{r})$ are the static external fields, for the perturbation in the electron distribution $\delta f(\underset{\sim}{r},\underset{\sim}{v},t)$ caused by the driving fields $\underset{\sim}{E}(\underset{\sim}{r},t)$ and $\underset{\sim}{B}(\underset{\sim}{r},t)$. The plasma response current is obtained by integrating $\underset{\sim}{v}\delta f$ over velocity and substituting the result into Maxwell's equations to yield a closed set of equations for the fields.

The early work by Buchsbaum and Hasegawa [17,33] assumed an isotropic Maxwellian form for f, employed the longitudinal approximation ($\underset{\sim}{B}(\underset{\sim}{r},t) \equiv 0$), and neglected the static ambipolar electric field necessary to maintain the equilibrium density profile. Azevedo and Vianna [34] and Hedrick [29] have given treatments which incorporate the anisotropy of the distribution function caused by $\underset{\sim}{B}_0$ but

ignore the ambipolar electric field. Pearson's [35] and Baldwin's [18] results include both the distribution function anisotropy and the ambipolar field necessary to maintain whatever equilibrium density profile is assumed.

In all of these treatments the plasma response current is expanded as a series with terms of the form $T^n \frac{\partial^{2n}}{\partial r^{2n}} h(\underset{\sim}{r})\, E(\underset{\sim}{r})$ where $h(\underset{\sim}{r})$ is a function which varies on the same scale as the equilibrium density and T is the electron temperature. This expansion is usually identified as one in r_L/L where $r_L = \sqrt{\frac{2\kappa T}{m\omega_c^2}}$ is the Larmour radius and L is a characteristic scale length for the fields or density profile. If this series were substituted into Maxwell's equations, the resulting wave equation would be of infinite order. For this reason, a low temperature assumption $r_L/L << 1$ is invoked and the series is truncated after the $(r_L/L)^2$ term. Use of the truncated series results in a fourth-order wave equation which can be written as:

$$
\begin{aligned}
&[\lambda^2\alpha(\frac{m^2}{\xi^2} - K_\perp) + O(\lambda^4/\xi^2)]\, E_\theta^{iv} + [\frac{\lambda^2\alpha}{\xi}(6\,\frac{m^2}{\xi^2} - \xi\alpha' - 4K_\perp) + \\
&2(\lambda^2\alpha)'(\frac{m^2}{\xi^2} - K_\perp) + O(\lambda^4/\xi^3)]\, E_\theta''' - [(\frac{m^2}{\xi^2} - K_\perp)K_\perp + O(\lambda^2/\xi^4)]\, E_\theta'' \\
&+ [\frac{m^2\alpha'}{\xi^2} + \frac{K_\perp}{\xi}(K_\perp - \frac{3m^2}{\xi^2}) + O(\lambda^2/\xi^5)]\, E_\theta' + \{\frac{m\alpha'}{\xi}[\frac{m}{\xi^2}(1 + m\Omega_c) - \Omega_c] + \\
&\frac{m^2\Omega_c^2\alpha^2}{\xi^2} + K_\perp[\frac{2m\Omega_c}{\xi^2} - K_\perp(\frac{2m^2+1}{\xi^2} - K_\perp) - \Omega_c^2\alpha^2 + \frac{m^2(m^2-1)}{\xi^4}] \\
&+ O(\lambda^2/\xi^6)\}\, E_\theta = 0
\end{aligned}
\tag{4.8}
$$

where $\lambda^2 = \frac{3\Omega_c}{2(4\Omega_c^2 - 1)} (k_0 r_L)^2$ is a temperature parameter and is << 1. Equation (4.8) has been obtained from Baldwin's* vector wave equation (Baldwin's Eqn. (3.13)) retaining the ambipolar electric field effects. In the low-temperature approximation all terms written as $0(\cdots)$ are neglected. It should be noted that this is not strictly valid very near the origin but that region has already been excluded from consideration. This assumption is also open to question in the coefficient of E_θ'' very near the hybrid point where $K_\perp = 0$. In this case the only effect of the $0(\lambda^2/\xi^4)$ term is to produce a shift of $0(\lambda^2/\alpha'(\xi_1)\xi_1^4)$ in the location of the singular point which is typically much less than 1% and thus can be safely neglected.

Expanding in the complex ζ-plane about the hybrid point, as discussed in deriving Eqn. (4.2), yields:

$$E_\theta^{iv} + \frac{\xi_1}{m^2}\left[\alpha_1\left(2\frac{m^2}{\xi_1} - \xi_1\right) + \frac{6m^2}{\xi_1^2}\right]E_\theta''' + \frac{\alpha_1}{\lambda^2}\left[\zeta E_\theta'' + E_\theta' + A^2 E_\theta\right] = 0 \tag{4.9}$$

where $\alpha_1 \left(= \left.\frac{d\,\alpha(\zeta)}{d\zeta}\right|_{\zeta=0}\right)$ and A (defined in Eqn. (4.3)) are as in the cold plasma case. Again the important assumptions are basically of the form $\xi_1 >> |\zeta|$. With the exception of the third derivative term, Eqn. (4.9) is in the form of the Orr-Sommerfeld equation [36]

---

*Baldwin's results were obtained under the same assumptions as were Pearson's but appear to be slightly different for the two-dimensional case when transverse propagation is considered ($m \neq 0$ in cylindrical geometry). These differences are not important here, since they involve terms which are discarded in arriving at the model equation.

of hydrodynamic stability. To reduce Eqn. (4.9) to the appropriate canonical form, the third derivative term is eliminated by a transformation of the dependent variable yielding:

$$\mathcal{E}_\theta^{iv} + \frac{1}{\Lambda}[\zeta\mathcal{E}_\theta'' + \mathcal{E}_\theta' + A^2\mathcal{E}_\theta] = 0 \qquad (4.10)$$

where $\mathcal{E}_\theta(\zeta) = \exp\{-4\frac{\xi_1}{m^2}[\alpha_1(\frac{2m^2}{\xi_1} - \xi_1) + 6\frac{m^2}{\xi_1^2}]\zeta\}E_\theta(\zeta)$

and $\Lambda = \lambda^2/\alpha_1$ is a temperature parameter (in the typical case $\Lambda \sim 10^{-10} \times T$ for T in ^oK). In the region under consideration the exponential term is approximately one, and thus $\mathcal{E}_\theta$ can be considered identical to E_θ. The term in brackets in Eqn. (4.10) is the left-hand side of Eqn. (4.2), the model equation for E_θ developed in the cold plasma case. Since $\zeta = 0$ is a turning point for Eqn. (4.10), the point at which the upper hybrid condition is satisfied in the warm plasma will be identified as the hybrid turning point.

Solutions of Eqn. (4.10) have been developed by Rabenstein [19] for $|\frac{1}{\Lambda}|$ large (T small) using the method of Laplace integrals. This approach involves representing the solutions in the form of contour integrals,

$$\mathcal{E}_\theta(\zeta) = \int_C e^{\zeta t} f(t)\, dt$$

where the form of $f(t)$ and the contours of integration in the complex t-plane are determined from substitution into Eqn. (4.10). Rabenstein shows that there are seven possible contours (and corresponding solutions), which he denotes as $B_{0,1,2,3}$ and $A_{1,2,3}$ of which only combinations of the form B_0, B_i, A_j, A_k with i,j,k all

different are independent. The independent solution set* B_0, A_1, A_2, B_3 will be used in the subsequent development.

Using the method of steepest descents, each solution is given as an asymptotic expansion in powers of $\sqrt{\Lambda/\zeta^3}$ which is valid in a region bounded away from the origin. In the collision-free case ($\Gamma = 0$) the solution path, as discussed in Section 4.2, is the real ζ-axis, and the asymptotic solution, given in the form of connection formulas across the hybrid point, are

$$B_0: \quad 2\pi i\, I_0(2A\sqrt{-\zeta})(1+0(\Lambda)) \leftrightarrow 2\pi i\, J_0(2A\sqrt{\zeta})(1+0(\Lambda))$$

$$A_1: \quad 2\pi i\, I_0(2A\sqrt{-\zeta})(1+0(\Lambda)) + \frac{\sqrt{\pi}\ \sqrt[4]{-\Lambda}}{(-\zeta)^{3/4}}\{\exp[i\tilde{\zeta}] - \exp[-i\tilde{\zeta}]\}\ (1+0((\frac{\Lambda}{\zeta^3})^{1/2})) \leftrightarrow \frac{i\sqrt{\pi}\ \sqrt[4]{-\Lambda}}{\zeta^{3/4}} \exp[-\frac{2}{3}\frac{\zeta^{3/2}}{\sqrt{-\Lambda}}](1+0((\frac{\Lambda}{\zeta^3})^{\frac{1}{2}}))$$

$$A_2: \quad -\frac{\sqrt{\pi}\ \sqrt[4]{-\Lambda}}{(-\zeta)^{3/4}} \exp[+i\zeta](1+0((\frac{\Lambda}{\zeta^3})^{1/2})) \leftrightarrow \frac{\sqrt{\pi}\ \sqrt[4]{-\Lambda}}{\zeta^{3/4}} \exp[\frac{2}{3}\frac{\zeta^{3/2}}{\sqrt{-\Lambda}}](1+0((\frac{\Lambda}{\zeta^3})^{1/2})) \tag{4.11}$$

$$B_3: \quad 2\pi i\, I_0(2A\sqrt{-\zeta})(1+0(\Lambda)) + 2K_0(2A\sqrt{-\zeta})(1+0(\frac{\Lambda}{\zeta^3})) + \frac{\sqrt{\pi}\ \sqrt[4]{-\Lambda}}{(-\zeta)^{3/4}} \exp[+i\tilde{\zeta}](1+0((\frac{\Lambda}{\zeta^3})^{1/2})) \leftrightarrow \pi i H_0^{(1)}(2A\sqrt{\zeta})(1+0(\frac{\Lambda}{\zeta^3}))\ ,$$

---

*This set is presented in detail in Rabenstein [19] Section 6 with his α, β, ξ, λ replaced by 1, A, $\frac{2}{3}\zeta^{2/3}/\sqrt{-\Lambda}$, and $-i/\sqrt{-\Lambda}$ respectively. The choice of $\arg(\lambda)$ is motivated by the fact that Λ is negative real when $\Gamma = 0$ and the density gradient is negative at the hybrid layer.

where $\tilde{\zeta} = \frac{2}{3}(-\zeta)^{3/2}/\sqrt{-\Lambda} - \pi/4$, with $\arg(-\zeta)^{3/2} = 0$, has been introduced for convenience and, as in the cold plasma case, a positive sign has been assumed for $\sqrt{A^2}$. The solutions on the high density side of the coupling region are presented on the left of the $\leftrightarrow$.

The Bessel function terms in these solutions correspond to the cold-plasma electromagnetic mode, as will be demonstrated shortly, and the exponential terms can be identified as Bernstein waves since their local wave number satisfies the Bernstein mode dispersion relation [16] in the region away from the hybrid layer. Since propagating Bernstein modes are backward waves, the Bernstein terms appearing in A_2 and B_3 on the high density side carry energy toward the center of the column and on the low density side the solution A_2 represents an exponentially decaying Bernstein curve tunneling inward from some source on that side of the hybrid layer.

With this interpretation, the modes are decoupled on the low density side of the hybrid layer in the solution sets as given, and the linear combinations $B_3 - A_2$ and $A_1 - B_0$ along with B_0 and A_2 form a decoupled set on the high density side. Thus the model equation predicts that there is no coupling between the various modes as long as they remain away from the hybrid point and that coupling can occur only in crossing the hybrid layer. For this reason the neighborhood around the hybrid layer in which the $O((\Lambda/\zeta^3)^{1/2})$ terms cannot be neglected will be denoted as the coupling region.

As there are no sources for evanescent Bernstein waves in the case of interest, solution A_2 will be dropped. Writing E_θ as the

following linear combination of the remaining three solutions:

$$E_\theta = \frac{(C_1 + 2C_2)}{2\pi i} B_0 + \frac{C_3}{2\pi i} A_1 + \frac{iC_2}{\pi} B_3$$

gives the following connection formula (the terms indicating the order of approximation have been suppressed):

$$(C_1 + C_3) I_0(2A\sqrt{-\zeta}) + \frac{2iC_2}{\pi} K_0(2A\sqrt{-\zeta}) + \frac{i\sqrt[4]{-\Lambda}}{\pi(-\zeta)^{3/4}} \{(C_2 - \frac{C_3}{2}) \exp[i\tilde{\zeta}] +$$

$$(\frac{C_3}{2}) \exp[-i\tilde{\zeta}]\} \leftrightarrow C_1 J_0(2A\sqrt{\zeta}) + C_2 H_0^{(2)}(2A\sqrt{\zeta}) + \qquad (4.12)$$

$$\frac{C_3 \sqrt[4]{-\Lambda}}{\sqrt{\pi}(\zeta)^{3/4}} \exp[-\frac{2}{3}\frac{(\zeta)^{3/2}}{\sqrt{-\Lambda}}]$$

Recalling their backward wave nature, only the $\exp[-\tilde{\zeta}]$ term in Eqn. (4.12) represents an "outgoing" Bernstein wave, i.e., one which carries energy outward toward the hybrid layer. Thus, if there are no outgoing Bernstein waves present, C_3 must be zero, and Eqn. (4.12) is the same connection formula for the Bessel function terms as was derived for the electromagnetic mode in a cold plasma (Eqn. (4.6)), which justifies the identification made above.

4.4 Conditions for validity of the cold plasma results

If the presence of an "ingoing" Bernstein wave (a wave carrying energy inward, away from the hybrid layer) does not affect the relationship between C_1 and C_2 required by boundary conditions on the high density side of the hybrid layer, and $|C_3| \ll |C_1|$ and $|C_2|$, then the warm plasma connection formula, Eqn. (4.12), is equivalent to the

cold plasma connection formula, Eqn. (4.6). In this case the inclusion of finite temperature effects will not alter the cold plasma field solutions outside the hybrid layer, and the cold plasma theory should be adequate to predict the scattering properties of the plasma. For a cylindrical plasma, the boundary condition at the column axis requires total reflection* of the ingoing Bernstein wave into an outgoing wave, so the presence of the Bernstein waves will not alter the boundary condition on the electromagnetic mode. Thus, the negligibility of C_3 should be sufficient to guarantee that the cold plasma results will be valid outside the hybrid layer.

Although the model equation approach adopted in this work is not adequate to develop theoretical estimates of when C_3 will be negligible, as will be discussed below, there is an experimentally observable consequence of the presence of an outgoing Bernstein wave at the hybrid layer. Since there are no sources for Bernstein waves other than the linear conversion process, any outgoing wave present at the hybrid layer will interfere with the ingoing wave and cause fine structure (the Buchsbaum-Hasegawa resonances) to appear in the measured scattering coefficients of the plasma. Thus, if there is no fine structure evident in the scattering coefficient over some range of densities or magnetic fields, then it can be assumed that C_3 is negligible over that range and scattering properties calculated on the basis of the cold plasma theory should be valid.

---

*The wave "reflected" back toward any sector of the hybrid layer is just the ingoing wave from the diametrically opposite sector of the hybrid layer.

In the collision-free case it is unlikely that the cold plasma theory will be valid for any bounded plasma because, with a closed hybrid surface and no damping, the Bernstein waves generated by linear conversion will travel across the high density plasma region and eventually become outgoing waves. In a real plasma the Bernstein waves are subject to strong collisional damping at low temperatures due to their low group velocities. Hence a theoretical estimate of when the cold plasma theory is valid in the external region would require the inclusion of collisional effects. Such an estimate would also require knowledge of the behavior of the solutions to the complete warm plasma wave equation (Eqn. (4.8)) over the entire region interior to the hybrid surface and is beyond the limitations of the model equation approach used in this work.

Collisional effects also reduce the conversion between the electromagnetic modes and the Bernstein modes at the hybrid layer. The conditions under which the conversion is negligible, and thus cold plasma solutions are valid over the entire plasma, can be estimated using the model equation. Since identical expansions about the hybrid point have been used in the warm and cold plasma model equations, the inclusion of collisional effects implies that the solution path moves off the real ζ-axis, as discussed in Section 4.2, and the point of closest approach* ζ_{ca} is a negative imaginary number. Recalling the discussion following Eqn. (4.11), as the solution path moves away

---

*This is the point at which the cold plasma solutions are maximum; defined as ζ_{max} in Eqn. (4.4).

from the origin it will leave the coupling region and it should be possible to form a set of solutions in which the electromagnetic and Bernstein modes are decoupled everywhere. The condition for the solution path to lie outside the coupling region is that the $O((\Lambda/\zeta^3)^{1/2})$ terms in Eqns. (4.11) be negligible, which implies:

$$|\zeta_{ca}|^{3/2} >> |\Lambda|^{1/2} \tag{4.13}$$

When inequality (4.13) is satisfied, the arguments of the exponential functions in Eqns. (4.11) have large real parts such that the Bessel function term in solution A_1 is negligible relative to the $\exp[-i\tilde{\zeta}]$ term, and the $\exp[+i\tilde{\zeta}]$ term in solution B_3 is negligible relative to the Bessel function terms. Hence, when inequality (4.13) is satisfied, the terms corresponding to the electromagnetic modes disappear from the solutions* representing the Bernstein modes and vice versa, and the solutions given in Eqns. (4.11) form a decoupled set as written. Assuming a parabolic density profile, the distance of closest approach is given by Eqn. (4.4) and when

$$\left| \frac{\xi_w^2 \Gamma(1 + \Omega_c^2)}{\xi_1 \Omega_p^2(0)} \right|^{3/2} >> \left| \frac{\lambda^2}{\alpha_1} \right|^{1/2} \tag{4.14}$$

the cold-plasma solutions will be valid† everywhere in the plasma.

---

*Since the Bernstein modes are primarily longitudinal in nature, it is also necessary to verify that inequality (4.13) is sufficient to guarantee the relative dominance of the corresponding terms in the solutions of the wave equation for E_r .

†Henderson [5] arrives at a similar condition for the importance of thermal corrections to the cold solutions in a one-dimensional electrostatic treatment.

Applying this discussion to Stenzel's [15] experimental conditions, inequality (4.14) becomes:

$$\sqrt{\frac{1}{T}\left(\frac{\Gamma}{\Omega_p^2(0)}\right)^3} \gg 5 \times 10^{-6}\, {}^{o}K^{-1/2}$$

where T is the electron temperature in ^{o}K, Γ is the normalized collision parameter, and $\Omega_p^2(0)$ is the normalized peak density. In the early afterglow ($\Omega_p^2(0) > .1$), T is about $5000^{o}K$ for the 1 cm diameter tube, and experimental conditions suggest that $\Gamma/\Omega_p^2(0)$ could be as low as 2×10^{-3} so, on the basis of inequality (4.13), significant mode conversion should be expected at the hybrid layer*. In the late afterglow T is about $500^{o}K$ and experimental conditions suggest that $\Gamma/\Omega_p^2(0)$ is about 10^{-2}, so the mode conversion process is probably negligible for $\Omega_p^2(0) < .05$.

Although mode conversion may be significant in the early afterglow, the ingoing Bernstein wave could be absorbed via collisional damping before it penetrates sufficiently far to give rise to a significant outgoing wave at the hybrid layer when the layer is far from the column axis. The experimentally measured scattering properties, taken at constant afterglow time (fixed $\Omega_p^2(0)$) show fine structure only when Ω_c is in the lowest 15-20% of the hybrid range ($\sqrt{1-\Omega_p^2(0)} < \Omega_c < 1$); thus, even in the early afterglow, the cold

---

*Under these conditions the radius of the coupling region is so large that the assumption of closeness to the hybrid layer made in deriving the model equation may no longer be valid at the edge of the coupling region, but the conclusions as to the nature and importance of the thermal effects should remain valid.

plasma model should be adequate over 80% of the hybrid range.

4.5 Connection between warm and cold plasma theories

When damping is included in the warm plasma theory, there is a smooth transition from the finite temperature results to the cold plasma results. This transition occurs because, as $T \to 0$ with fixed, nonzero $<\nu>$, the inequality (4.14) will eventually be satisfied. As discussed in the previous section, the damping effects will dominate the linear conversion process when inequality (4.14) is satisfied, and the warm plasma solutions become identical to the cold plasma solutions everywhere in the plasma.

The situation is less clear in the collision-free case. The terms which correspond to the Bernstein waves in E_θ (see Eqns. (4.11)) disappear as $\sqrt{T}$ for $\zeta \neq 0$; however, in the warm plasma theory when $m \neq 0$, E_r can be expressed* near the hybrid point in terms of E_θ as:

$$E_r = -\frac{i\xi_1^3\lambda^2}{m^4}\left\{mE_\theta''' + \left[\frac{4m}{\xi_1} + \xi_1\Omega_c\left(\frac{2m^2}{\xi_1^2} - 1\right)\right]E_\theta''\right\} + \frac{i\xi_1}{m}E_\theta' - \frac{i\xi_1^2}{m^2}\left(\Omega_c - \frac{m}{\xi_1^3}\right)E_\theta \tag{4.15}$$

Thus, as $T \to 0$, both the $\lambda^2 E_\theta'''$ and E_θ' terms tend to infinity as $T^{-1/2}$ for the Bernstein wave terms in Eqn. (4.15). Furthermore, the wavelength of the Bernstein waves, given by $i / (d\tilde{\zeta}/d\zeta)$, goes to

---

*The complete warm plasma expression for E_r, like Eqn. (4.8), follows directly from Baldwin's [18] vector wave equation. Equation (4.15) has been obtained from the complete expression by expanding about the hybrid point as discussed in deriving Eqn. (4.2).

zero as T. Thus, in the collision-free case the warm plasma solutions do not approach the cold plasma solutions at low temperatures (this behavior is not unusual since the equations for $T \neq 0$ are singular perturbations on the cold plasma equations).

Although the collision-free fields are dissimilar in the $T \to 0$ limit, the energy flux across the hybrid layer does show a connection between the low temperature warm plasma results and those for the cold plasma. The energy flux is obtained from the steady-state version of Poynting's theorem,

$$\frac{1}{2c\,\mu_0}\,\nabla_\xi \cdot \mathrm{Re}[\underset{\sim}{E} \times c\underset{\sim}{B}^*] = -\frac{1}{2k_0}\,\mathrm{Re}[\underset{\sim}{j}^* \cdot \underset{\sim}{E}] \tag{4.16}$$

by converting the volume integral of Eqn. (4.16) over a cylindrical shell containing the hybrid surface into an integral over the surface of the shell. The integrand of this surface integral is the energy flux across the surface of integration. Applying Gauss's theorem, the left-hand side of Eqn. (4.16) yields the electromagnetic energy flux as Poynting's vector:

$$\underset{\sim}{S}^{EM} = \frac{1}{2c\,\mu_o}\,[\underset{\sim}{E} \times c\underset{\sim}{B}^*] \tag{4.17}$$

If any part of the right-hand side of Eqn. (4.16) can be expressed as a divergence of a vector, then that vector is the convective energy flux $\underset{\sim}{S}^C$ carried by the field driven particle motions.

For the cold plasma, expressions for the response current, obtained from Eqns. (2.3), are

$$\frac{j_r}{\omega\varepsilon_o} = i(K_\perp - 1)\, E_r - K_\times E_\theta$$

$$\frac{j_\theta}{\omega\varepsilon_o} = K_\times E_r + i(K_\perp - 1)\, E_\theta \qquad (4.18)$$

These expressions imply that $\mathrm{Re}[\underset{\sim}{j}^* \cdot \underset{\sim}{E}] = 0$ since $K_\parallel$ and $K_\times$ are real in the collision-free case. Thus the only energy flux in the cold plasma is the electromagnetic flux given by $\underset{\sim}{S}^{EM}$. Using the collisionless connection formula, Eqn. (4.6), yields the radial component of Poynting's vector as:

$$S_r^{EM} = \frac{\alpha_1 \xi_1^2}{2c\mu_o \pi n^2} \begin{cases} \mathrm{Re}[C_2^* C_1] & , \ (\xi < \xi_1) \\ [\mathrm{Re}[C_2^* C_1] + C_2 C_2^*] & , \ (\xi > \xi_1) \end{cases} \qquad (4.19)$$

Recalling that $\alpha_1 < 0$, Eqn. (4.19) implies that the hybrid layer is absorbing energy at the rate

$$\frac{|\alpha_1|\ \xi_1^3}{\omega\mu_o\, m^2}\, C_2 C_2^*$$

demonstrating the collisionless absorption* mentioned in Chapter 1.

The expressions for the response current, to order λ^2, in the warm plasma which follow from Baldwin's vector wave equation are:

$$\frac{j_r}{\omega\varepsilon_o} = i(K_\perp - 1)E_r - K_\times E_\theta - \frac{i}{\xi}[\xi\lambda^2 E_r']' + \frac{2\Omega_c}{\xi}[\xi\lambda^2 E_\theta']' - \frac{2m\lambda^2(1 - 4\Omega_c^2)E_\theta'}{3\xi}$$

*Since no steady state exists at the hybrid layer in a nonrelativistic collision-free cold plasma, the use of Eqn. (4.16) is not justified there. The full time-dependent version of Poynting's theorem should be employed at the hybrid surface; however, since the time-dependent terms do not contribute to the flux, they have been ignored.

$$\frac{j_\theta}{\omega\varepsilon_o} = K_\times E_r + i(K_\perp - 1)E_\theta - \frac{2\Omega_c}{\xi}[\xi\lambda^2 E_r']' - \frac{i(1+8\Omega_c^2)}{3}[\xi\lambda^2 E_\theta']' - \frac{2m\lambda^2(1-4\Omega_c^2)}{3\xi}E_r' \tag{4.20}$$

Using Eqns. (4.20), the right-hand side of Poynting's theorem, Eqn. (4.16), can be written as

$$\frac{1}{2k_o}\mathrm{Re}[\underset{\sim}{j}^* \cdot \underset{\sim}{E}] = \sqrt{\frac{\varepsilon_o}{\mu_o}}\frac{\lambda^2}{2}\nabla_\xi \cdot \{\mathrm{Re}\{\frac{2}{3}\frac{m}{\xi}(4\Omega_c^2 - 1)E_\theta^* E_r + 2\Omega_c[(E_\theta^*)'E_r - (E_r^*)'E_\theta] + \frac{i}{3}(1+8\Omega_c^2)(E_\theta^*)'E_\theta + i(E_r^*)'E_r\}\hat{a}_r\} \tag{4.21}$$

Thus, in the warm plasma there is a radial convective energy flux given by the expression in brackets. Using Maxwell's equations with $\underset{\sim}{j}$ given by Eqns. (4.20), and the warm plasma connection formula for E_θ, Eqn. (4.12) yields the same expression, Eqn. (4.19), for S_r^{EM} as was obtained in the cold plasma case and

$$S_r^C = \begin{cases} \dfrac{\alpha_1\xi_1^2}{2c\mu_o\pi m^2} C_2 C_2^* & , \quad (\xi < \xi_1) \\ 0 & , \quad (\xi > \xi_1) \end{cases} \tag{4.22}$$

for the convective energy flux, as $T \to 0$.

In the warm plasma the Bernstein wave terms in Eqn. (4.12) contribute only to S_r^C and the electromagnetic terms contribute only to S_r^{EM} in the $T \to 0$ limit. Thus, comparing Eqns. (4.19) with (4.22), the same amount of energy which is absorbed at the cold

collisionless hybrid layer is converted into Bernstein waves at the finite temperature hybrid layer. So, even though the warm plasma solutions do not agree with the cold plasma solutions in the collisionless case, the electromagnetic energy flux is identical in both cases and, for $T \neq 0$, instead of the ever-increasing energy store at the hybrid layer predicted by the cold plasma theory, a steady state is attained in which the energy is convected away from the layer as a Bernstein wave.

4.6 Validity of approximating dissipative effects by $<\nu>$

The major wave dissipative mechanisms in the experimental afterglow plasmas with which this work is concerned are the electron-neutral and electron-ion collisions, and transit time effects. The cold plasma theory of Chapter 2 assumes that all these effects can be approximated by a simple drag force $-m\underset{\sim}{v}<\nu>$, in the electron equation of motion; the warm plasma theory of Section 4.3 assumes that the $(\frac{\partial \delta f}{\partial t})_{\text{collisions}}$ term in Boltzmann's equation (Eqn. (4.7)) can be replaced by $-<\nu>\delta f$ where, in both cases, $<\nu>$ is a velocity independent effective collision frequency. Although there are some theoretical arguments which justify the use of these simple forms, evaluation of the approximations involved is beyond the scope of this work. Consequently, the damping terms will be considered as heuristic in nature, and their use will be justified primarily on the basis that they have little quantitative effect on the scattering properties of interest here. In this spirit, the form of $<\nu>$ has been chosen individually for each of the processes as the best simple form available.

For the electron-neutral collisions it is reasonable to replace $(\frac{\partial \delta f}{\partial t})_{\text{collisions}}$ by $-\nu_{en}(\underset{\sim}{v})\delta f$ in Boltzmann's equation (Eqn. (4.7)) (cf. Clemmow and Dougherty [37], Section 9.5.2, or Holt and Haskell [38], Section 10.1) where $\nu_{en}(\underset{\sim}{v})$ is the momentum transfer collision frequency. In this form the linearized Boltzmann's equation can be solved for the response of an infinite uniform plasma to a uniform oscillating electric field in the absence of any static fields* (cf. Heald and Wharton [39], Section 2.4.2). If $\nu_{en}(\underset{\sim}{v}) \ll \omega$, the plasma response can be described by a conductivity which has the same form as the conductivity derived from the hydrodynamic equations (Eqns. (2.1) with $B_0 = 0$) if $<\nu>$ is defined as:

$$<\nu> = -\frac{4\pi}{3}\int \nu_{en}(v)\,\frac{df_0(v)}{dv}\,v^3 dv \tag{4.23}$$

where f_0 is the equilibrium speed distribution and will be assumed to be Maxwellian. The electron-neutral momentum transfer collision frequency can be expressed in terms of the momentum transfer cross section $\sigma_m(v)$ as follows

$$\nu_{en}(v) = p\,\frac{273}{T_g}\,v\,\sigma_m(v) \times 3.54(10)^{16}\,\text{sec}^{-1}$$

where p is the neutral background pressure in Torr, T_g is the neutral gas temperature, and $3.54(10)^{16}$ is the number of particles in 1 cm^3 of an ideal gas at 1 Torr and 0°C. For neon, Chen [40] gives

---

*The effects of a static magnetic field can be included, but the results are similar except for the narrow range when $|\omega - \omega_c| \lesssim <\nu>$. Since sheath effects, which might be important for $\omega \sim \omega_c$, have been ignored, the effects of the static magnetic field will also be neglected.

$\sigma_m(v)$ in the form $A + Bv$ and Eqn. (4.23) yields:

$$\langle \nu_{en} \rangle_{Ne} = p \frac{273}{T_g} [3.13(10)^5 T^{1/2} + 9.81(10)^4 T]$$

where T is the electron temperature in ^oK. For argon, the momentum transfer cross section was approximated by

$$\sigma_m(v) = 1.4(10)^{-17}(1 - Av^n \exp(-nv^2/v_R^2)) cm^2$$

where A and n are arbitrary parameters chosen for each temperature to match the empirical data given by Frost and Phelps [41] at $v = v_R$, the Ramsauer minimum, and at $v = \sqrt{5kT/m}$, the maximum of the term multiplying $\sigma_m(v)$ in the integral expression for $\langle \nu \rangle$ in terms of $\sigma_m(v)$.

In the waveguide geometry, thermal motion along B_0 may carry an electron out of the waveguide side walls at which point its directed momentum is lost, just as if it had undergone a close-range collision. This is the source of the transit-time damping, and its treatment should involve something like introducing an upper limit on the axial mean free path due to close-range processes (or, equivalently, a lower limit on $\nu_{en}(v_z)$) before averaging to obtain $\langle \nu_{en} \rangle$. A simpler estimate of the transit-time damping can be obtained by calculating a separate effective collision frequency $\langle \nu_t \rangle$, ignoring all other collision mechanisms, and using $\langle \nu_t \rangle$ as a minimum for $\langle \nu_{en} \rangle$. The average distance which an electron must travel to escape is $a/2$ where a is the axial width of the waveguide, so the transit time "collision" frequency can be written as

$$\nu_t(v) = 2v/\sqrt{3}a$$

and Eqn. (4.23) yields:

$$\langle \nu_t \rangle = \frac{9.55(10)^5}{a} T^{1/2}$$

The electron-ion collisions involve the long range Coulomb forces and are best included directly in the kinetic equation. In the infinite wavelength limit this was done by Oberman, et al [42,43] for a homogeneous plasma with isotropic Maxwellian equilibrium distribution. Since inclusion of the static magnetic field requires the evaluation of nontrivial integrals over the plasma dispersion function, the expression for $\langle \nu_{ei} \rangle$ used in this report is

$$\langle \nu_{ei} \rangle = 1.14(10)^{-9} \frac{\omega_p^2}{T^{3/2}} \ell n(2.5(10)^8 T^{3/2}/\omega)$$

as given by Dawson and Oberman [44] for the magnetic field-free case in the range $\omega_p < \omega$.

4.7 Validity of the linearization assumptions

The linearization approximations are of somewhat less importance than the approximations considered in previous sections, since the existence of steady state solutions implies that the linearization conditions can be arbitrarily well satisfied experimentally by placing a sufficiently large attenuator between the generator and the plasma. When the linearized equations are valid, the external scattering properties of the plasma must be power independent, so the linearization assumptions are sometimes verified experimentally by observing that the power levels are always below those for which the scattering

coefficients depart from their low power values. When a hybrid resonant layer is present in the plasma, such an experimental verification could be in error because the external properties of the plasma are nearly constant over a considerable range of damping parameters and temperatures. Thus the presence of nonlinear effects, such as heating and frequency doubling which primarily affect the damping parameter and temperature, may be masked.

The linearization of the cold plasma* equations (2.1) requires that $|v| \ll c$, $|n| \ll N$ and that the driving field cause negligible heating if the effective collision frequency $\langle\nu\rangle$ is a function of temperature. These conditions will be investigated on the basis of the results presented in Chapter 3 for typical experimental parameters. The limits established on this basis should be considered only as suggestive due both to the dependence of the perturbation amplitudes at the hybrid layer on the value of $\langle\nu\rangle$ and to the possibility of significant thermal effects at the hybrid layer.

The requirement that $|v| \ll c$ is equivalent to neglecting diamagnetic effects in the plasma response. Inspection of Fig. 3.2 suggests that $|v| \ll c$ if $E_0 \ll 10^3$ v/cm. This would not be a significant restriction on typical microwave power levels since the incident power P_{in} in S-band waveguide is given by

$$P_{in} \sim 10^{-2}|E_0|^2 \text{ watts} \tag{4.24}$$

---

*Essentially similar conditions follow from the linearization of Boltzmann's equation (4.7).

when E_0 is expressed in V/cm.

The condition that $|n| << N$ is required in the linearization of the currents in Maxwell's equations and is thus a condition for negligible harmonic generation. The curve for $|n|/N$ presented in Fig. 3.1 indicates that $|n| << N(0)$ if $E_0 << 1$ V/cm and thus, from Eqn. (4.24), harmonic generation might be significant at power levels in the 10 milliwatt range. For the assumed profiles, which go to zero at the wall, the condition $|n| << N$ cannot be satisfied near the wall since $n(r_w) \neq 0$. This violation is probably not significant as the region near the wall contributes little to either the scattering or the absorption. Furthermore, the difficulty may lay in the neglect of sheath structure rather than in any essential nonlinear behavior.

The condition for negligible heating cannot be guaranteed by simply requiring that the directed energy of a particle be negligible relative to its thermal energy, in view of the fact that while an electron loses all its directed energy in a momentum randomizing collision, it can lose only $\frac{3m_e}{2M_i} \kappa(T_e - T_i)$ of its total energy in the collision. Initially, collisions will convert the energy absorbed from the wave into electron thermal energy elevating the electron temperature until, eventually, the collisional energy loss rate balances the absorption rate. At this point the energy absorbed from the wave is transferred entirely to the heavy particles and a

true steady state* exists, since by virtue of their long mean free paths the heavy particles can rapidly transfer the energy to the walls and remain essentially unheated. In the collisional cold plasma the local rate at which a particle absorbs energy from the wave is $\langle\nu\rangle m_e|\underset{\sim}{v}|^2$ where v is the local perturbed electron fluid velocity, so the electron heating will be negligible if:

$$\kappa\Delta T = \frac{2M_i}{3}\frac{\langle\nu\rangle}{\langle\nu_{ei}\rangle+\langle\nu_{en}\rangle}|\underset{\sim}{v}|^2 << \kappa T_e$$

The ratio of effective collision frequencies arises because the transit-time damping contributes to the wave absorption but not to the electron-heavy particle energy transfer. The results presented in Fig. 3.2 for v imply that $P_{in} << .5$ μwatt for negligible heating at the hybrid layer.

The discussion in this section suggests that the plasma perturbation may be significant at low power levels. Stenzel's [15] experimental investigation of the effects of the incident wave power

---

*There are actually two steady states involved here, the incident field establishes the linear steady state perturbation in a time of $0(1/\langle\nu\rangle)$ while the heating is a quasi-steady state process accomplished in a time of $0(M_i/m_e[\langle\nu_{ei}\rangle+\langle\nu_{en}\rangle])$. During the heating, the perturbations (and therefore the fields) change only as the heating affects the plasma parameters. Stenzel experimentally demonstrated these time scales ($1/\langle\nu\rangle \sim .1$μsec and $M_i/m_e[\langle\nu_{ei}\rangle+\langle\nu_{en}\rangle] \sim 3$ msec for the plasmas studied) by showing that the heating of the hybrid layer was dependent only on the pulse energy for pulse lengths between 1 μsec and 100 μsec and that the temperature of the hybrid layer decayed on a 1/2 msec time scale after the end of the heating pulse. This decay time is about the same as the temperature relaxation times for the unheated plasmas.

tends to confirm this suggestion. Pulse heating experiments in the late afterglow ($T \sim 350^{\circ}K$) show strong emission enhancement, evidence of significant heating, for a 5 μwatt power level. As the pulse power is increased to the 100 μwatt range, the plasma decay rate is strongly increased and ultimately, at milliwatt power levels, the excitation causes sufficient ionization to overcome the enhanced diffusion and the plasma can be maintained by a continuous microwave signal.

V. Small Column Scattering Properties

5.1 Approximate scaling relations for the scattering coefficients

A typical set of calculated power absorption curves are displayed in Fig. 5.1 as a function of magnetic field (ω_c/ω) for constant values of $\omega_p^2(0)$ and $\langle\nu\rangle$ assuming a parabolic density profile*. The shaded portions of the ω_c/ω axes denote the range over which a hybrid layer exists somewhere† in the plasma. A major feature of these curves, and of the experimental measurements, is a collapsing scale in ω_c/ω as $\omega_p^2(0)/\omega^2$ decreases. In the theoretical calculations, this scale is correlated with the hybrid range, as is evident in Fig. 5.1, and it has been assumed that the similar scaling which appears in experimental results also correlates with the hybrid range (see discussion in Section 5.4). This behavior in both the theoretical and experimental results, and the nature of the hybrid resonant response developed in Chapters 3 and 4, suggests the possibility of a scaling relation between ω_c/ω and $\omega_p^2(0)/\omega^2$ which would allow sets such as are shown in Fig. 5.1 to be obtained from a single curve.

An exact scaling relation would be a function of the four parameters, g(r) (the profile shape function) $\omega_p^2(0)/\omega^2$, ω_c/ω, and $\langle\nu\rangle/\omega$, which has the property that the plasma response (and the

---

*This form of presentation was chosen for compatibility with Stenzel's [15] experimental measurements which will be presented in Section 5.4.

†The hybrid resonance appears at the column center for ω_c/ω at the left hand end (denoted as the onset point, $(\omega_c/\omega)_o$) of the shaded hybrid range and approaches the wall as ω_c/ω increases to one.

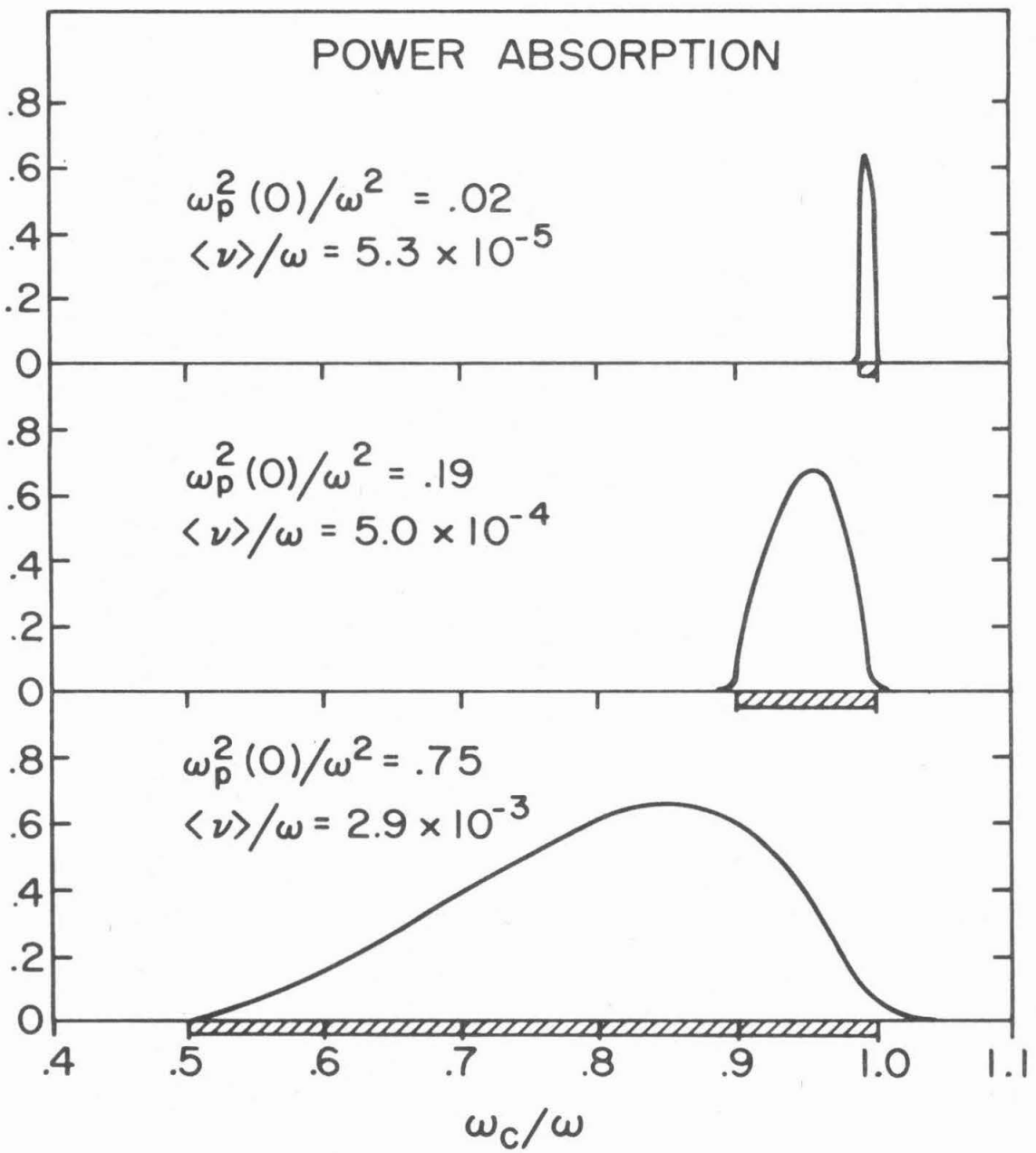

Fig. 5.1 Typical set of calculated strip line power absorption coefficients for various values of $\omega_p^2(0)$ and $\langle\nu\rangle$, including glass effects, $r_w = 0.5$ cm, $r_t = 0.6$ cm, $K_g = 3.8$, $\omega = 2\pi \times 3.0$ GHz.

scattering coefficients) is indistinguishable for all parameter sets which yield the same value of the scaling function. Recalling the discussion in Section 2.2, the plasma response is completely described by the dielectric tensor components $K_{\perp}(r)$ and $K_{\times}(r)$, which can be written in the form

$$K_{\perp}(r) = 1 - \alpha g(r) , \quad K_{\times}(r) = \frac{\omega_c/\omega}{1 - i\langle\nu\rangle/\omega} \alpha g(r) \tag{5.1}$$

where

$$\alpha(\omega_p^2(0)/\omega^2,\ \omega_c/\omega,\ \langle\nu\rangle/\omega) \equiv \frac{\omega_p^2(0)/\omega^2(1 - i\langle\nu\rangle/\omega)}{[(1 - i\langle\nu\rangle/\omega)^2 - \omega_c^2/\omega^2]} .$$

The plasma response will be indistinguishable for two different parameter sets if the functions $K_{\perp}(r)$ and $K_{\times}(r)$ are identical for both parameters sets. Since $g(0) \equiv 1.0$ for all shape functions, $K_{\perp}(r)$ and $K_{\times}(r)$ can be identical only if both α and $\omega_c/\omega/[1 - i\langle\nu\rangle/\omega]$ are identical, a condition which can be satisfied only for identical parameter sets. Thus, there is no useful exact scaling relation, but a useful approximate scaling relation does exist for low densities. Since $\langle\nu\rangle \ll \omega$, $\omega_c/\omega/[1 - i\langle\nu\rangle/\omega]$ will be nearly constant over the hybrid range at low densities, and $K_{\perp}(r)$ and $K_{\times}(r)$ will be approximately scaled for any parameter sets for which the profile shapes are identical and $\alpha(\omega_p^2(0)/\omega^2, \omega_c/\omega, \langle\nu\rangle/\omega)$ is constant. When

$$(\langle\nu\rangle/\omega)^2 \ll [1 - (\omega_c/\omega)^2]^2$$

then

$$\mathrm{Re}\,[\alpha] \simeq \frac{\omega_p^2(0)/\omega}{1 - \omega_c^2/\omega^2}$$

and

$$\mathrm{Im}[\alpha] \simeq -\frac{\frac{\langle\nu\rangle}{\omega}\left(1+\frac{\omega_c^2}{\omega^2}\right)}{\omega_p^2(0)/\omega^2}\,[\mathrm{Re}[\alpha]]^2$$

so the scaling relation $\alpha = \text{const}$ becomes*

$$\frac{1-(\omega_c/\omega)^2}{\omega_p^2(0)/\omega^2} = \text{const}\ , \qquad \frac{\frac{\langle\nu\rangle}{\omega}\left(1+\frac{\omega_c^2}{\omega^2}\right)}{\omega_p^2(0)/\omega^2} = \text{const} \tag{5.2}$$

These scaling relations are physically reasonable. The first scaling relation requires that the hybrid layer fall at the same radius and the second requires that the solution maxima at the layer be the same (see Eqns. (4.5)). The existence of the collision-free limit, as discussed in Chapter 3, suggests that the first of Eqns. (5.2) should be more important than the second.

A quantitative analytic assessment of the validity of the scaling is difficult since it would require some estimate of the sensitivity of the solutions at $r = r_w$ to the errors in the coefficients of Eqns. (2.3) caused by the approximate nature of the scaling. As an alternative, the effectiveness of the scaling relation has been computationally investigated. The cases presented in Fig. 5.1 are displayed in Fig. 5.2 as functions of the first scaling parameter (the values of

---

*The approximation used in arriving at Eqns. (5.2) is not valid in a narrow region about $\omega_c/\omega = 1$; however, in that region α is predominantly imaginary and, since the second of Eqns. (5.2) will preserve the scaling of $\mathrm{Im}[\alpha]$ at $\omega_c/\omega = 1$, Eqns. (5.2) will be assumed to be valid everywhere.

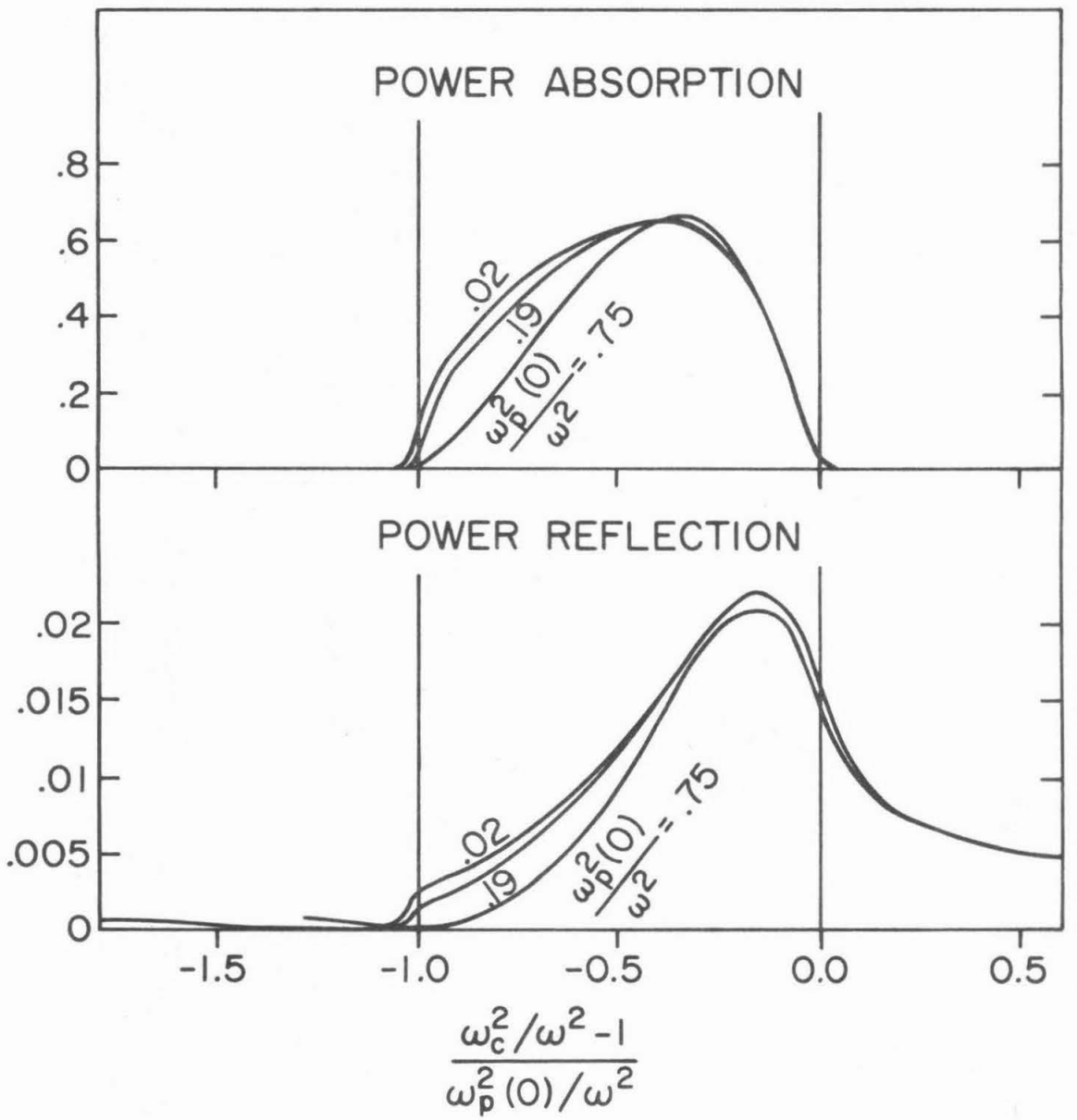

Fig. 5.2 Power absorption as a function of the first scaling parameter suggested in Eqns. (5.2) for cases presented in Fig. 5.1. Power reflection is also shown. The hybrid layer is present for $(\omega_c^2/\omega^2 - 1)/\omega_p^2(0)/\omega^2$ between -1.0 and 0 , as indicated by the vertical bars.

$<\nu>$ were chosen so that the second scaling parameter is constant at $\omega_c/\omega = 1$ for all cases) and, in addition, the matched line power reflection curves for the same cases are also presented. On the basis of the results presented in Fig. 5.2 and estimates of the errors which occur in the coefficients of the second order differential equation for cB_z, the scaling relations presented in Eqns. (5.2) appear to be quite adequate when $\omega_p^2(0)/\omega^2 \leq .2$. In addition Fig. 5.2 indicates that the scattering properties will be qualitatively similar over the entire low density range. For these reasons, the remaining discussion for the low density case with the exception of a set of curves calculated for direct comparison with experimental results will be illustrated by curves calculated with the particular value $\omega_p^2(0)/\omega^2 = .19$*.

5.2 Effects of external geometry on the scattering coefficients

The effect of the external geometry on the plasma power reflection is illustrated in Figs. 5.3 and 5.4. The upper curves in Fig. 5.3 show an equivalent power reflection coefficient for a plane wave, defined by the power per unit axial length scattered toward the generator $\sigma_s/2$ (σ_s is derived in Appendix C) divided by the incident power carried across an area of unit axial length and height equal to the parallel plate spacing a, while the lower curves are simply $|r_{ML}|^2$. The left-hand curves represent the reflection from a plasma column without a glass envelope and the right-hand curves represent

*This value was chosen primarily to yield a convenient hybrid range $\omega_c/\omega \in (.9, 1.0)$.

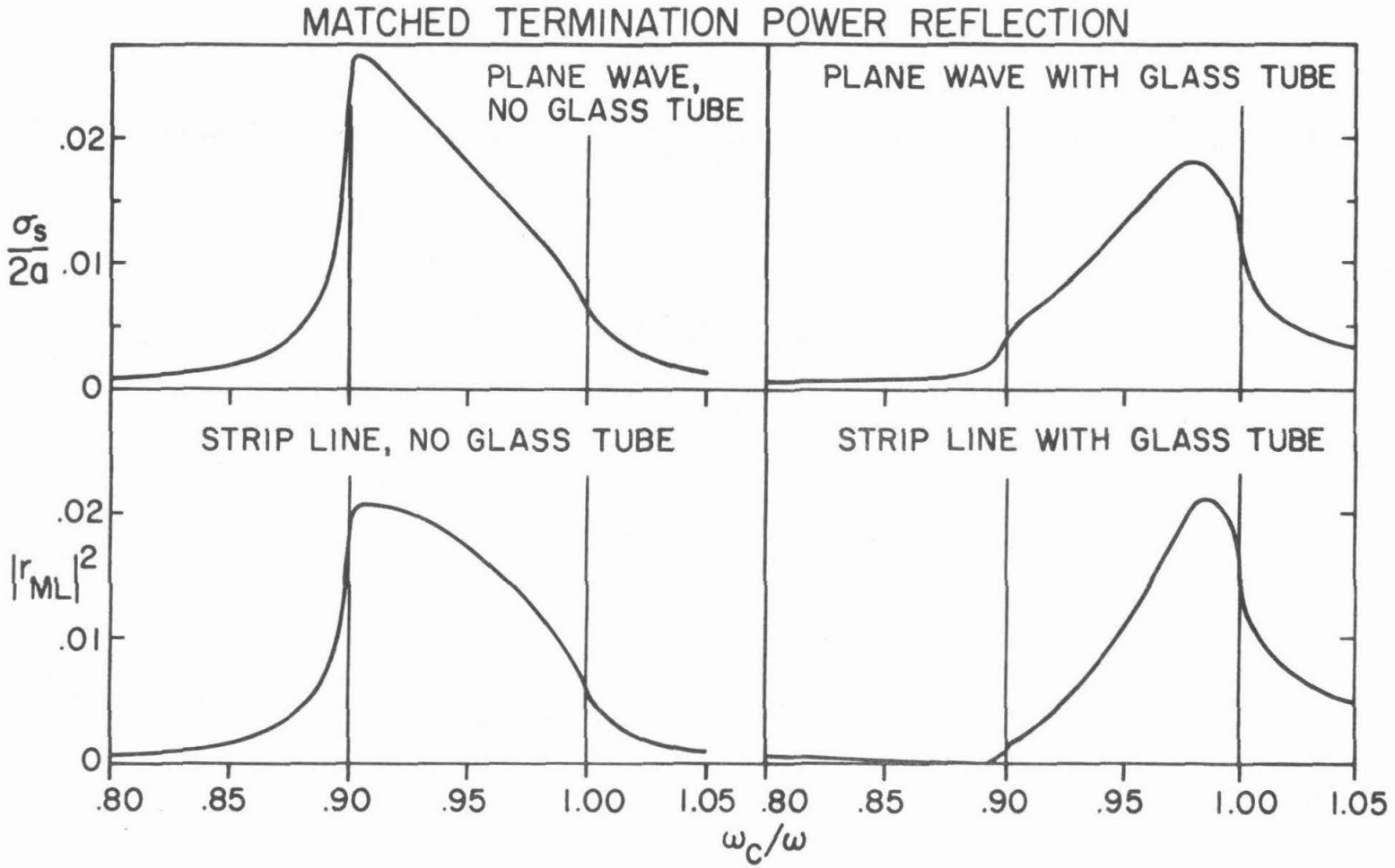

Fig. 5.3 Equivalent power reflection coefficients showing the effect of various external configurations, $\omega_p^2(0)/\omega^2 = .19$, $\langle\nu\rangle/\omega = 8.0 \times 10^{-4}$, $r_w = 0.5$ cm, $r_t = 0.6$ cm, $K_g = 3.8$, $\omega = 2\pi \times 3.0$ GHz.

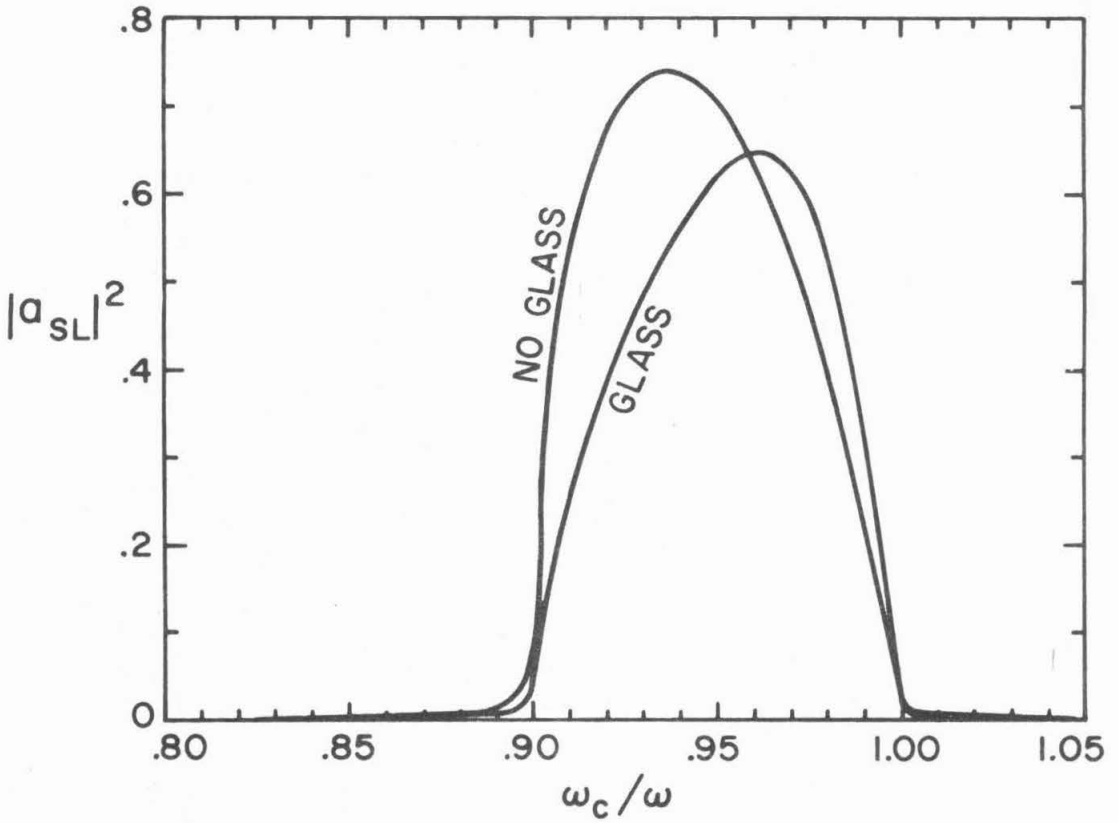

Fig. 5.4 Power absorption coefficient with and without glass tube for strip line with shorted termination, plasma conditions as in Fig. 5.3.

the reflection from the plasma column with a glass envelope. Only the strip line results appear in Fig. 5.4 because there does not seem to be any satisfactory way to relate the plane wave scattering properties of the column to those for the column in a shorted transmission line without the use of an arbitrary scaling parameter.

The effects of the glass tube on the scattering are not simple since the fields scattered from the plasma modify the dielectric response in the glass and vice versa. Near the onset point $(\omega_c/\omega)_o$ the interaction results in partial cancellation of the scattered fields, but as ω_c/ω approaches 1.0, the time phase of the fields scattered from the plasma changes and the interaction results in reinforcement. The strength of the glass effects indicates that they should be included in order to make quantitative comparisons between theory and experiment. The interaction between the plasma and the glass tube suggests that it is less desirable* to tune or balance out the glass effects experimentally than to include them explicitly in the theoretical treatment when quantitative results are desired.

---

*The experimental scattering measurements reported by Greenwald [45] and by Blum, Bauer, Gould and Stenzel [13] were made using a bridge arrangement to balance out the reflected signal from the empty glass tube. The reflection coefficients measured in these studies show two peaks, one near $(\omega_c/\omega)_o$ and another near $\omega_c/\omega = 1.0$, which is qualitatively different from the theoretical results obtained in the current study either with or without the glass tube. This disagreement may be a result of the use of such balancing procedures.

5.3 Dependence of the theoretical scattering coefficients on $\langle\nu\rangle$ and the profile shape

The results of varying $\langle\nu\rangle/\omega$ over three orders of magnitude are shown in Fig. 5.5 for a parabolic density profile with $\omega_p^2(0)/\omega^2 = .19$ and $\langle\nu\rangle/\omega$ constant for each of the curves shown. Thus, these curves represent slowly varying values for the second scaling parameter given in Eqns. (5.2) and the labels actually give the value of this parameter at $\omega_c/\omega = 1$. These curves show the existence of the collision-free limit.

The absorption and reflection for several density profiles are shown in Fig. 5.6 for $\omega_p^2(0)/\omega^2 = .19$ and $(2\langle\nu\rangle/\omega)/(\omega_p^2(0)/\omega^2) = 5 \times 10^{-3}$. The increasing magnitude of the scattering and the shift of the peaks toward lower values of ω_c/ω seem to be the major effects of flattening the profiles near $r = 0$.

5.4 Comparison with experimental scattering measurements for $\omega_p^2(0)/\omega^2 < 1.0$

The theoretical results to be presented in this section were computed using a parabolic profile as a reasonable approximation in the afterglow when ambipolar effects should be important. The central density for each experimental curve was calculated from the observed value of $(\omega_c/\omega)_o$ for the absorption assuming that

$$\frac{\omega_p^2(0)}{\omega^2} = 1 - \left(\frac{\omega_c}{\omega}\right)_o^2 \tag{5.3}$$

The value of $\langle\nu\rangle$ was calculated via the method discussed in Section 4.6 from electron temperature measurements made under similar

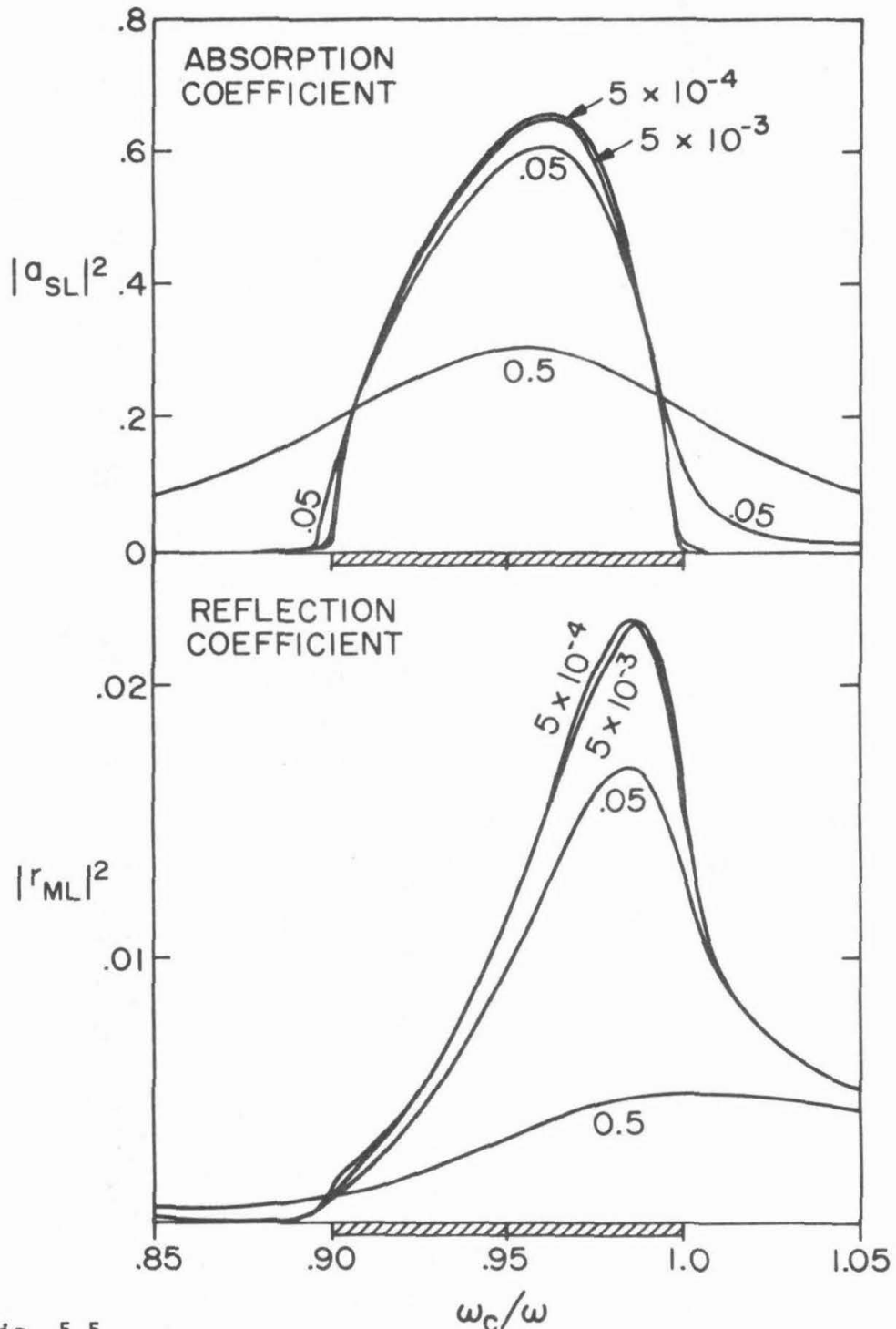

Fig. 5.5
Strip line power absorption and reflection coefficients as a function of damping, remaining parameters as in Fig. 5.3. The curves are labeled by the value of $\frac{2\langle\nu\rangle/\omega}{\omega_p^2(0)/\omega^2}$

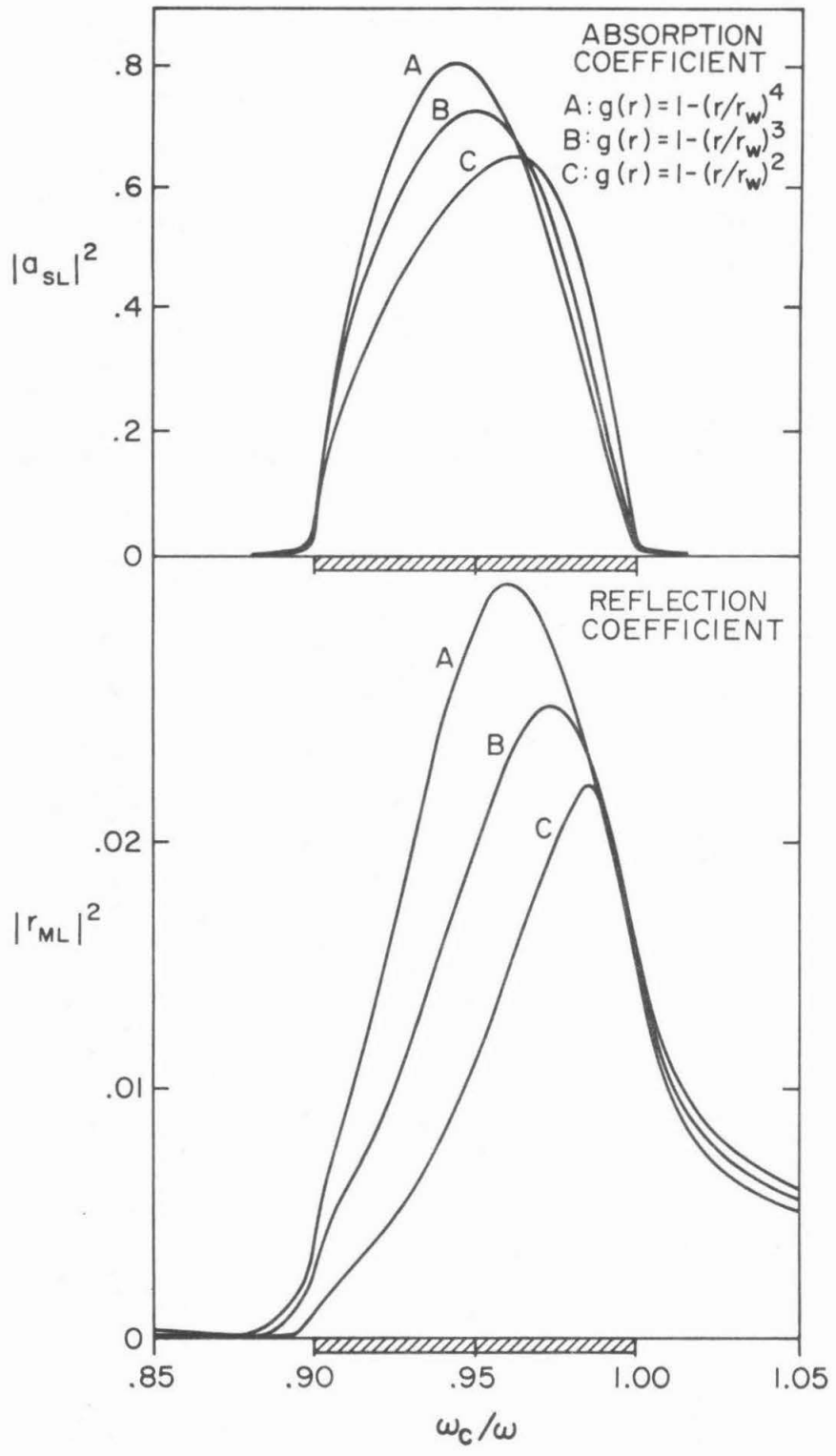

Fig. 5.6 Strip line power absorption and reflection coefficients as a function of the density profile shape, plasma conditions as in Fig. 5.3.

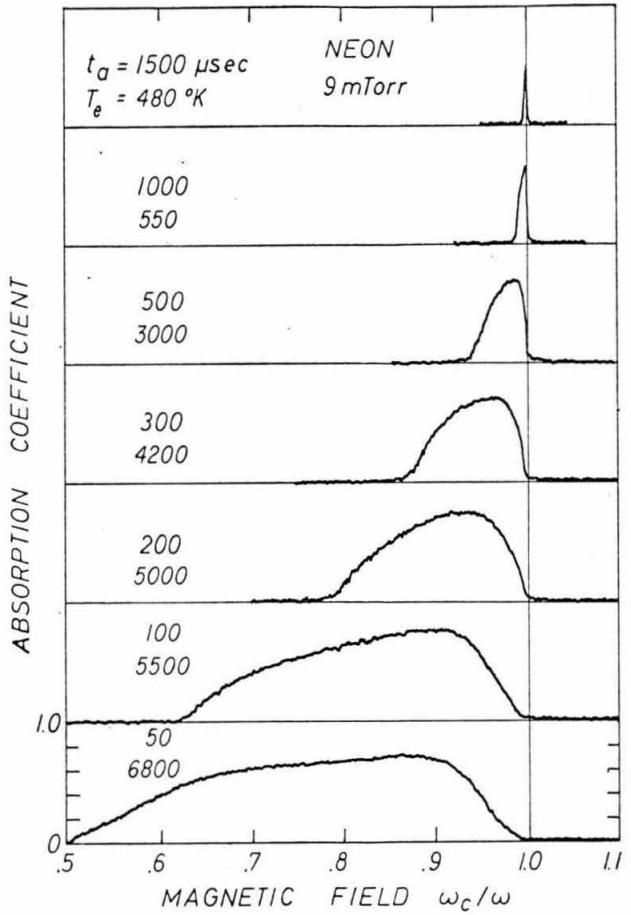

Fig.5.7 Experimentally measured power absorption for neon at 9 mtorr for various afterglow times. Approximate electron temperatures in the plasma core are from separate measurements. After Stenzel [15,Fig.3.3]

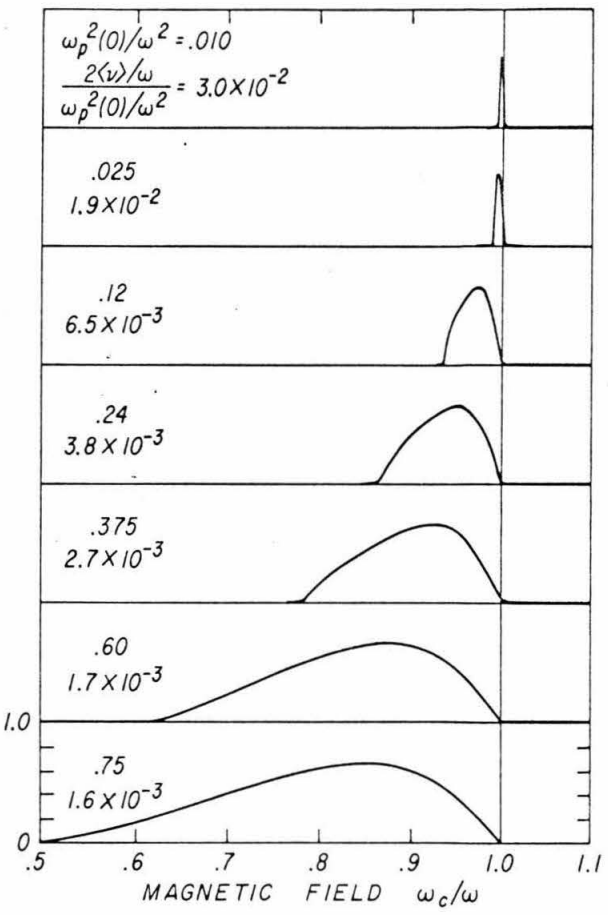

Fig.5.8 Theoretically calculated strip line power absorption coefficients for cases corresponding to the experimental conditions in Fig. 5.7.

experimental conditions. The parameter values derived from Figs. 5.7 and 5.9 were used to calculate the curves in Figs. 5.8 and 5.10. The reflection coefficients displayed in Fig. 5.11 were measured for plasma conditions identical to those for Fig. 5.9 and so the parameters derived from Fig. 5.9 were also used to calculate the results presented in Fig. 5.12.

The use of Eqn. (5.3) to determine the central density in the experimental columns is based on the results of the theoretical treatment which indicates that the absorption onset occurs at $(\omega_c/\omega)^2 = 1 - \omega_p^2(0)/\omega^2$. The onset of enhanced absorption has been utilized as a measure of the peak density in various geometries by Lustig [46] , Schmitt, Meltz and Freyheit [47] , Tanaka [48] , Stenzel [15] , and Henderson [5] , but Lustig, Schmitt et al, and Tanaka apparently interpreted the absorption onset as corresponding to the maximum upper hybrid resonance frequency on the basis of results presented by Buchsbaum, Mower, and Brown [49] from a cavity perturbation analysis assuming a uniform plasma. The perturbation results are, however, stated in terms of a resonance at $\omega^2 = \omega_c^2 + \omega_p^2/G$ where G is a geometrical factor depending on the incident field configuration, and they do not predict the existence of a well defined absorption onset. The first theoretical treatment to actually establish the use of Eqn. (5.3) appears to be Blum's [13,14] planar calculation. Comparison of Figs. 5.9 with 5.11 or 5.10 with 5.12 illustrates another consequence of the effect of the glass tube. Due to the partial cancellation caused by the glass, the onsets of both the measured and calculated reflection coefficients do not correspond to the onsets of the absorption at

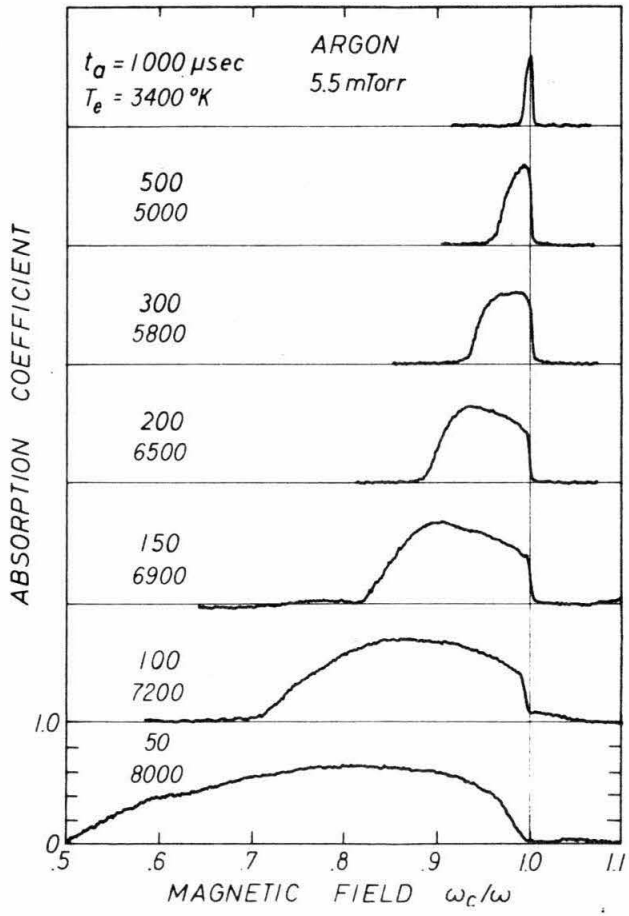

Fig.5.9 Experimentally measured power absorption for argon at 5.5 mtorr for various afterglow times. Approximate electron temperatures in the plasma core are from separate measurements. After Stenzel [15], Fig.3.4

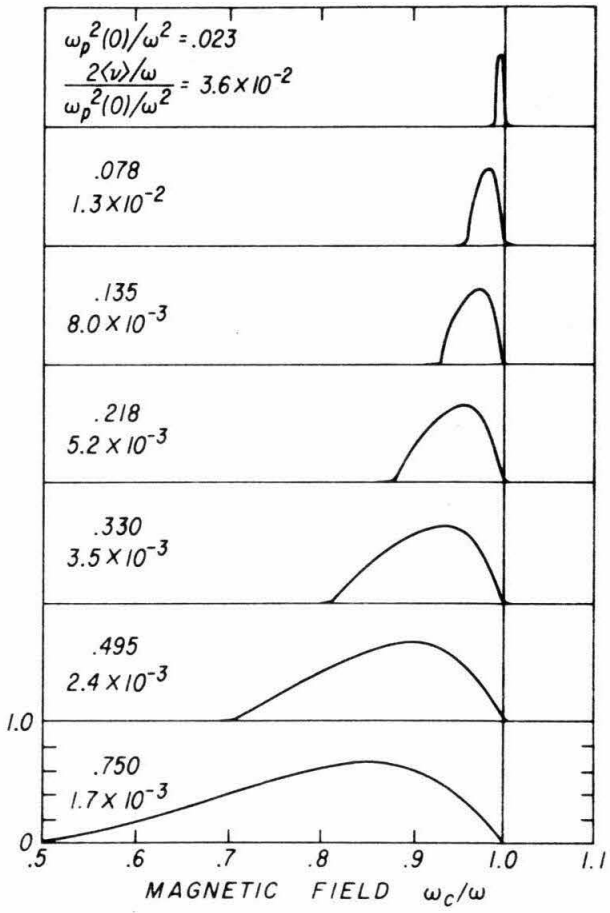

Fig.5.10 Theoretically calculated strip line power absorption coefficients for cases corresponding to the experimental conditions in Fig. 5.9

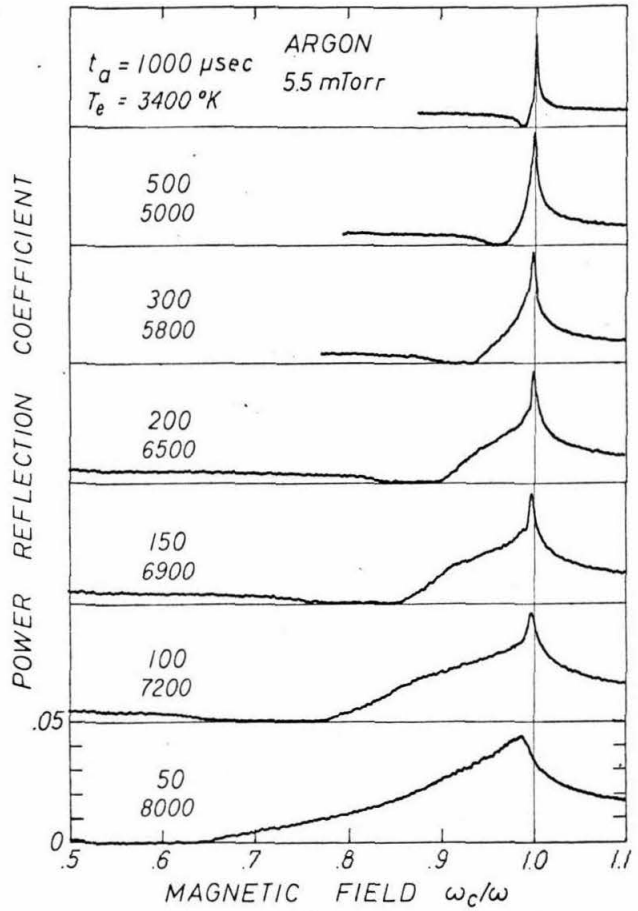

Fig. 5.11 Experimentally measured power reflection for experimental conditions as in Fig. 5.9. After Stenzel [15] Fig. 3.10.

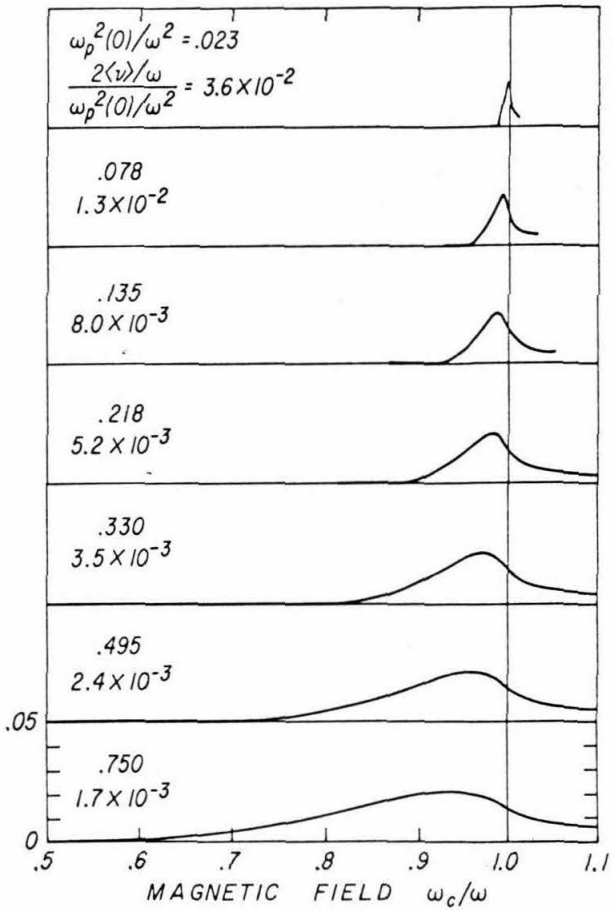

Fig. 5.12 Theoretically calculated power reflection for cases corresponding to those in Fig. 5.10.

moderate densities $\omega_p^2(0) \gtrsim .2$ and thus the reflection onset is not a reliable indicator of the maximum upper hybrid resonance frequency. Comparison of the experimental and theoretical absorptivities show that, while the theory does yield reasonable agreement ($\sim$ 10% for the maximum value of the absorption) the curve shapes do not exhibit impressive similarity. Comparison between the theoretical and experimental reflectivities reveals a more serious disagreement. The curves are only mildly similar in shape and the theoretical reflectivities are only one-half the experimental values at their respective maxima.

A partial explanation of these differences may lie in the observation that scattering curves measured for similar densities and temperatures also exhibit different shapes when the rf pulses which cause the breakdown are altered or when the gases (cf. Figs. 5.7 and 5.9) are changed (which also changes the breakdown conditions). This suggests that the afterglows studied may have density profiles which are significantly different from the assumed nearly-ambipolar one; unfortunately it was not possible to verify directly the profile shape in experimental apparatus employed for these measurements. Both the reflectivity and the absorptivity would be affected by any density profile differences that might exist. In particular, some calculations were carried out for profiles with $g(r_w) \neq 0$ in a rough test of the effects which might arise from a sheath formed at the edge of the column. The major effects on the calculated scattering properties were the introduction of a small, sharp spike in the reflection and an accelerated dropoff in the absorption for $(\omega_c/\omega)^2 \geq 1 - \frac{\omega_p^2(0)}{\omega^2} g(r_w)$. Such a combination of features might appear near

$\omega_c/\omega = 1$ in the 100 and 150 μsec curves in Figs. 5.9 and 5.11.

In addition to the possible profile differences, there is also the question of the validity of comparing results measured in a waveguide with results calculated for a strip line. A perturbation theory approach [50] can be used to derive the reflection coefficient for a dielectric rod in a waveguide and in a parallel plate line when the dielectric constant and size of the rod is such that the reflection coefficient is small. In this case the power reflection in a waveguide is $(k_0/k_g)^2$ times stronger* than the reflection from an identical object in a strip line with the same vertical spacing. However, this increase in the reflectivity occurs only for weakly reflective dielectric objects, and as the reflectivity increases, the results in the two cases must approach each other. The reflection coefficient in a waveguide is also affected by the presence of the holes in the side walls. In a larger experimental tube (I.D. 2.0 cm) the reflection from the holes alone was as strong as the reflection from the glass tube and the experimental and theoretical reflectivities for the larger tube show even less agreement than those for the smaller tube (for this reason no comparison results have been presented for the larger tube). The differences between the waveguide and strip line absorption coefficients are probably small for two reasons. First, the relatively strong absorptivity in the strip line suggests that the results are

---

*This enhancement would apply to the reflected fields from both the plasma and the glass tube so its effect near $(\omega_c/\omega)_o$ where the glass and plasma reflections compete is not obvious, but might well be small as the comparison between Figs. 5.11 and 5.12 seems to suggest.

probably in the region where the strip line and waveguide results approach each other. Second, the absorption in the cold plasma is proportional to the excitation of the hybrid layer and when the reflected fields are small, as is true in all the cases studied, the excitation should be proportional to the incident electric field perpendicular to $\underset{\sim}{B}_0$ and the fractional power absorbed ought to be identical in the strip line and in the waveguide*.

Finally, the experimental curves presented in this section were obtained by averaging at constant afterglow time over many cycles of a repetitively fired plasma. Using this method, the slight shot-to-shot variations in the afterglow conditions result in an average over the Buchsbaum-Hasegawa fine structure. The presence of this fine structure has been observed [15] by displaying the reflected signal as a function of afterglow time for a single shot. Such observations suggest that the constant afterglow time results for $\omega_p^2(0)/\omega^2 \gtrsim .1$ are averages over the fine structure for approximately the 15-20% of the hybrid range starting at $(\omega_c/\omega)_o$. Thus, as was discussed in Section 4.4, the cold plasma scattering results may not be valid over this range.

---

* This argument would indicate that the strip line absorption for a line terminated by a matched load $|a_{ML}|^2$, and the equivalent plane wave absorption defined as σ_a/a, should also be nearly identical. For the typical case depicted in Figs. 5.3 and 5.4, σ_a/a and $|a_{ML}|^2$ agree within $\sim$ 10% over the entire hybrid range, which lends additional support to the argument.

5.5 Comparisons with experimental measurements for $\omega_p^2(0)/\omega^2 \gtrsim 1$ and with theoretical results using the electrostatic approximation

Experimental measurements of the transmission coefficient for an afterglow plasma with $\omega_p^2(0)/\omega^2 > 1$ have been reported by Henderson [5] . The measurements were performed in a waveguide with a matched load so the matched line power transmission coefficient $|t_{ML}|^2$ is given by

$$|t_{ML}|^2 = 1 - |r_{ML}|^2 - |a_{ML}|^2 \tag{5.4}$$

A typical experimental curve is shown in Fig. 5.13 for $\omega_c/\omega = .9$. The abscissa is a logarithmic scale for the central density which was derived from the afterglow time. The values in parentheses were extrapolated from measured decay rates and are probably lower than the actual density at the indicated point. The scale values are given in terms of $\omega_p^2/\omega^2 \,/\, [1 - (\omega_c/\omega)^2]$ so the hybrid layer will be present for all values greater than one.

The high density minimum in the transmission corresponds to strong excitation of the hybrid layer in the $m = -1$ mode. This shift in excitation from the $m = +1$ mode at low densities to the $m = -1$ mode at high densities is a result of the increasing reflected fields from the high density region at the center of the plasma. These increasing reflected fields are evident in the transmission which is almost completely determined by the absorptivity at low densities while, in the vicinity of the high density minimum, the reflectivity becomes comparable to the absorptivity.

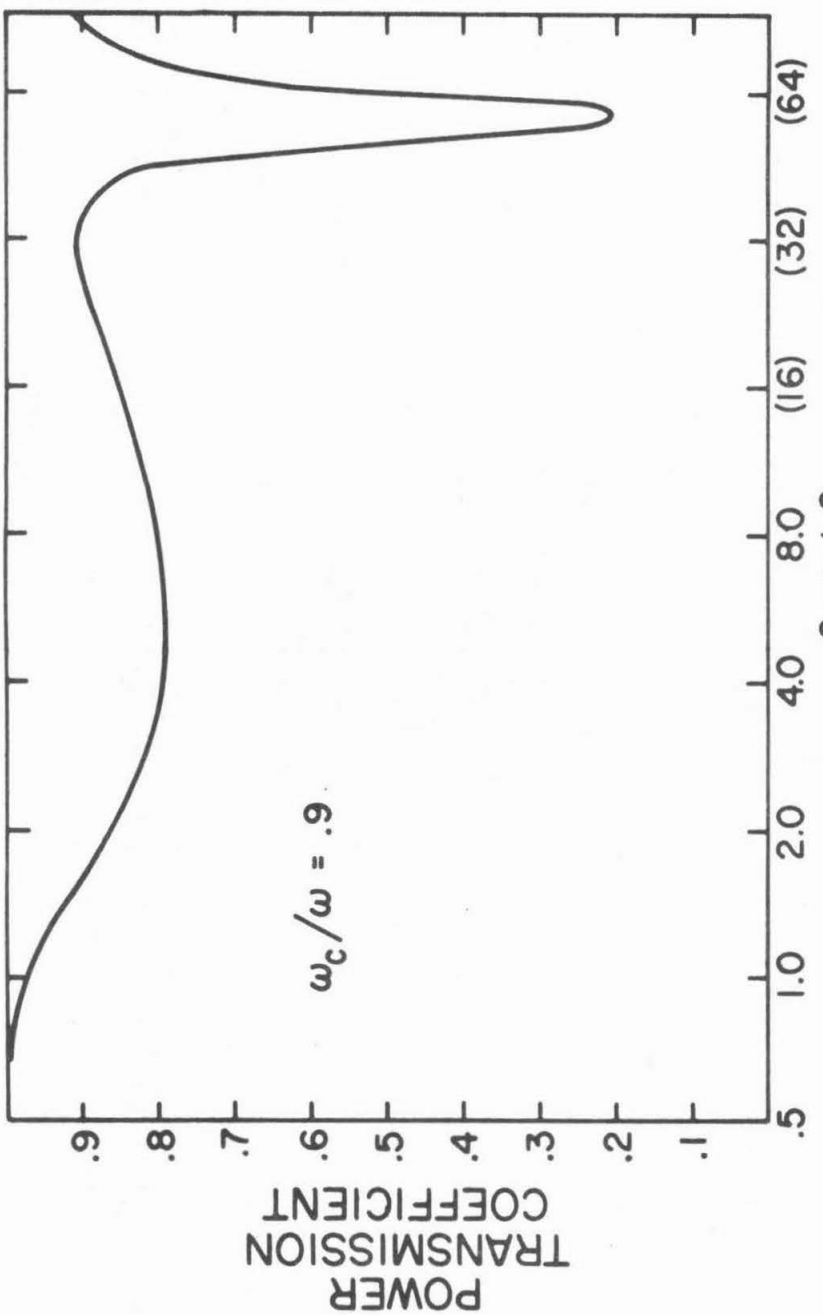

Fig. 5.13 Experimentally measured matched line power transmission as a function of plasma density, from Henderson [5].

The theoretically calculated strip line transmission using the methods developed in this report is shown as the solid line in Fig. 5.14. The agreement between the electromagnetic calculation and the experimental measurements is reasonable, as might be expected since the reflection coefficient appears significantly in the transmission only when it is large (and therefore when it should be nearly the same in the strip line and waveguide geometries).

For comparison the transmission calculated by Baldwin and Ignat (as reported by Henderson [5]) using an electrostatic approximation is also shown in Fig. 5.14 as a dashed line. The electrostatic treatment was carried out by calculating the admittance of a collisionless cylindrical cold plasma with a Bessel function profile in a parallel plate capacitor. The electromagnetic calculation was made using a finite collision frequency (which was small enough to guarantee that the transmission was at its collision-free limit to better than the plotting accuracy) and a parabolic profile (which is close enough to $J_0(r/2.405\ r_w)$ that it should not give rise to any substantial differences in the transmission). The discrepancy between the plasma scattering, which is characterized by $|r_{ML}|^2$ and $|a_{ML}|^2$ or $1 - |t_{ML}|^2$, calculated by the two methods is more than a factor of two at some points. This error is apparently due to the electrostatic approximation itself since the expansion used by Baldwin and Ignat to compute the plasma admittance has a claimed accuracy of 0.5% in the low density region. Since the electrostatic approximation still requires the numerical solution of a second order differential equation and appears to be quite unreliable even for the relatively small value of $k_0 r (\sim .3)$

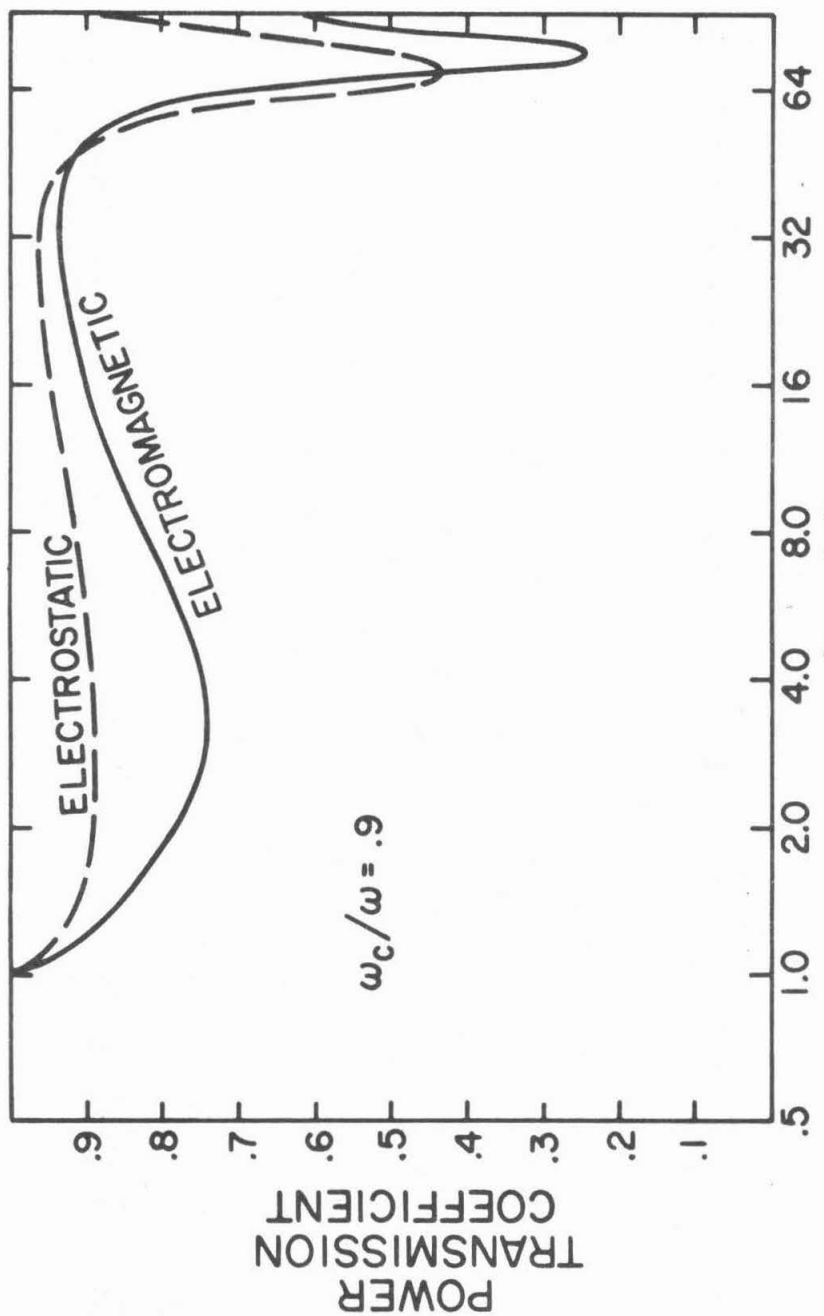

Fig. 5.14 Theoretically calculated strip line power transmission from the current (electromagnetic) treatment and Baldwin and Ignat's electrostatic treatment, reported by Henderson [5].

used here, it would appear to be unsuited for upper hybrid resonance scattering calculations.

VI. Conclusions and Suggestions for Further Study

6.1 Conclusions

This report has presented the results from a theoretical study of the nature of the upper hybrid resonance which occurs in the model of an inhomogeneous cold magnetoplasma. Since it is difficult to measure directly the internal state of the excited plasma, a considerable portion of this effort has been devoted to calculations of the external scattering properties of the plasma, preserving as many of the features of the geometry used for experimental measurements as possible without significantly increasing the amount of actual computation involved. In addition, the consequences of the neglect of finite temperature effects inherent in the cold plasma model have been investigated.

The calculation in cylindrical geometry has confirmed that the region of enhanced absorption appears between $\omega_c = (\omega^2 + \omega_{p\ max}^2)^{1/2}$ and $\omega_c = \omega$ for an inhomogeneous cylindrical plasma, just as it did in the planar treatment presented by Blum [13]. This result confirms the essential role of the density inhomogeneity in determining the absorption spectrum and provides a firm theoretical basis for using the experimentally observed absorption onset as a diagnostic for the maximum plasma density in a wide range of geometries. This treatment also demonstrates that the onset of enhanced reflection or scattering is not a reliable indicator of the maximum upper hybrid frequency due to the effects of the glass tube and strip line.

The investigation of finite-temperature effects carried out in Chapter 4 indicates that, in a warm plasma, the partial linear conversion of the incident electromagnetic wave into a Bernstein wave at the hybrid layer will not affect the cold plasma electromagnetic solution outside the hybrid layer unless there is also a Bernstein wave present carrying energy toward the hybrid layer. It was also demonstrated in Section 4.4 that collisional effects can dominate the linear conversion process, with the result that the cold plasma solutions are correct over the entire plasma. These results lead to the conclusion that the collisional cold plasma model might be useful in describing the external electromgnetic properties of a wider range of low-temperature plasmas than would be expected on the basis of the assumption that thermal effects must be strictly negligible.

This work, in conjunction with the companion experimental study [15], presents a case for the existence of a localized hybrid resonant layer in low-temperature magnetoplasmas. In Section 3.3 it was shown that the existence of the hybrid layer suggests a simple explanation of experimental radiation temperature measurements and that the hybrid layer might be useful as a microwave diagnostic to obtain spatially resolved temperature data. The existence of the hybrid resonant layer also suggests the possibility of nonlinear behavior at low power levels, as discussed in Section 4.7.

The most serious discrepancies between the theoretical and experimental results seem to have been caused by using the strip line geometry in the theoretical calculations as an approximation for the waveguide used experimentally. The quantitative differences between

the strip line scattering coefficients and the equivalent plane wave quantities suggest that the effects of the waveguide side walls and the holes through which the plasma passes need further investigation before scattering properties measured experimentally in a waveguide can be reliably interpreted in terms of a theoretical calculation.

6.2 Suggestions for further study

Although further refinements in the cold plasma calculation may not yield much greater understanding of the physical nature of the hybrid layer in a plasma, it may still be worth while to extend this treatment to a real waveguide-like geometry since there is a possibility that the scattering properties could be interpreted to yield the density profile in the plasma. This could prove to be a useful technique for investigating the profile in the sheath region near the plasma wall where probe techniques may be unreliable. It should be noted that the use of this diagnostic need not involve sweeping the magnetic field, as was assumed in this treatment, since the hybrid layer location can also be altered by sweeping the working frequency.

The current computational algorithm could be extended to include explicitly the effects of the Bernstein modes. This expanded calculation would involve a numerical solution of the fourth-order warm plasma wave equation in the coupling region near the hybrid layer and a WKB solution for the short wavelength Bernstein waves outside the coupling region. Such a treatment could be modified to include the effects of sources for the Bernstein waves in the plasma core, allowing direct comparison between the scattering from externally driven standing wave resonances and the emission from internally driven resonances, such as

calculated by Alper and Gruber [51] using a slab model.

The possibility of strong excitation of the plasma at the hybrid layer suggests that it should prove useful for nonlinear studies. Cano, Fidone, and Granata [52] have reported significant harmonic generation at relatively inaccessible* hybrid layers in large plasmas ($k_0 r \sim 10$). The techniques employed in this study could be extended to include such nonlinear effects and would permit the calculation of the efficiency of the processes. Further, since this study is based on an electromagnetic treatment, it would remain valid for the short wavelength modes which might be involved in nonlinear interactions.

The strong excitation of the hybrid layer could also be valuable in producing localized heated regions in a plasma. Examples of such heating have been presented in the companion experimental study for relatively cool plasmas and it might be of value to extend the theoretical investigation of the hybrid layer behavior to include hot plasma effects. The existence of a useful hybrid layer in a hot plasma is an open question since the appropriate expansion parameter is $(v_{th}\omega/c\omega_c)^2$, indicating that corrections to the first order thermal theory of Chapter 4 must also include relativistic effects. If the hybrid layer in a hot plasma retains its character as a region of strong coupling between the electromagnetic and Bernstein modes, it may still be useful for heating purposes since the slow Bernstein modes are subject to strong collisional damping and will thermalize rapidly.

---

*The hybrid resonance is described as inaccessible when a wide evanescent region screens it from the incident wave (see the discussion in Chapter 1).

Finally, the question of the accessibility of the layer in view of the short wavelengths associated with the parameters typically encountered in hot plasmas is also open because the decreasing B field encountered as a wave enters a confined hot plasma, at least in high β devices, will act to make the layer more accessible than would be predicted from the results for uniform $\underset{\sim}{B}_0$.

Appendix A

List of Symbols

A	dimensionless constant which appears in model equation solutions given in Chapter 4, p.50
A,n	arbitrary parameters used in evaluating argon collision frequency, p.69
A_m, B_m	coefficients used in constructing field solutions in the glass envelope in Chapter 2, p.21
a	axial width of the waveguide, p.69
a	parallel plate vertical spacing (used in Chapter 5, in place of b), p.80
a_{ML}	matched line absorption coefficient, p.93
a_{SL}	shorted line absorption coefficient, p.34
$a_n(x)$	Fourier coefficients of G_0, p.32
$\hat{a}_r$	radial unit vector, p.66
$\underset{\sim}{B}_0, \underset{\sim}{E}_0$	static magnetic and electric field vectors, p.2 and p.52
$\underset{\sim}{B}(\underset{\sim}{r},t)$, $\underset{\sim}{E}(\underset{\sim}{r},t)$	perturbation magnetic and electric field due to incident electromagnetic field, p.14
$\underset{\sim}{B}^{ext}, \underset{\sim}{E}^{ext}$	total electromagnetic fields external to the plasma column, p.19
$\underset{\sim}{B}^{glass}, \underset{\sim}{E}^{glass}$	total induced fields in the plasma envelope, p.21
$\underset{\sim}{B}^{inc}, \underset{\sim}{E}^{inc}$	incident wave magnetic and electric field, p.14
$\underset{\sim}{B}^{int}, \underset{\sim}{E}^{int}$	electromagnetic fields within the plasma column, p.22
$B^{interaction}$	magnetic field due to columns in the image array with $\ell \neq 0$, p.29
B^M, E^M	electromagnetic fields due to mirror image columns, p.24,25
B^R, E^R	electromagnetic fields due to real image columns, p.24,25
B^{scatt}, E^{scatt}	electromagnetic fields scattered from the plasma column or image array, p.28 and Appen. C, p.112

B_0, A_1, A_2, B_3	complete solution set to the warm plasma model equation, p.56
B_ℓ	ℓ^{th} Bernoulli number, Appen. B , p.111
$\tilde{B}_{zm}, \tilde{E}_{rm}, \tilde{E}_{\theta m}$	unnormalized solutions to Eqn. (2.3), p.22
b	stripline vertical spacing, p.14
C_m	coefficient defined in Eqn. (2.8), p.23
C_1, C_2, C_3	arbitrary constants used in constructing complete solutions to model equations of Chapter 4, p.51,58
c	speed of light, p.18
D_m	normalizing constant, p.22
$\mathcal{D}$	electric displacement vector, p.22
$\mathcal{D}^{glass}$	electric displacement in the glass envelope, p.21
$E_{r,\theta\ max}$	maximum field components near the hybrid point, p.51
$\mathcal{E}_\theta$	function related to E_θ introduced in Eqn. (4.10), p.5 p.55
e	magnitude of the electron charge, p.16
f_0	equilibrium speed distribution, p.68
$f(\underset{\sim}{r},\underset{\sim}{v})$	equilibrium electron distribution function, p.52
$\delta f(\underset{\sim}{r},\underset{\sim}{v},t)$	perturbed distribution function, p.52
G	geometrical factor, p.88
$G_m(\xi,\theta,y_0)$	generalized Schloemilch's series used in evaluating scattered fields from an image array with spacing y_0 , p.31
g(r)	density profile function, p.75
$H_m^{(1,2)}(\xi)$	Hankel functions of the first and second kinds, p.19
$h(\underset{\sim}{r})$	function varying on the same scale as the density profile function, p.53
$h_n^{M,R}$	Schloemilch's series evaluated in Appen. B, p.29

I_0, K_0	modified Bessel functions, p.52
J_m	Bessel function of the first kind, p.19
$\underset{\sim}{j}$	plasma response current, p.64
K_g	dielectric constant of the glass, p.21
$K_\perp, K_\times$	dielectric tensor components, p.18
k_g	guided wave number, p.14
k_n	transmission line wave number defined in Eqn. (2.25), p.33
k_0	free space wave number, p.6
L	characteristic scale length for the fields or density profile, p.53
$\mathcal{L}$	raising operator for cylindrical waves, p.32
ℓ	column number in the image geometry, p.26
M_i	ion mass, p.72
m, m_e	electron mass, p.16,72
m	angular mode number, p.18
N(r)	equilibrium electron density, p.16
$n(r,\theta)$	amplitude of perturbation in electron density, p.16
n_g	refractive index of the glass, p.21
$P_{abs}(r)$	local power absorption, p.42
P_{in}	incident power in S-band waveguide, p.71
p	neutral background pressure, p.68
(r,θ,z)	cylindrical polar coordinates, p.7
r_L	Larmour radius, p.53
r_{ML}	matched line reflection coefficient, p.34
r_{SL}	shorted line reflection coefficient, p.34
r_t	outer radius of plasma envelope, p.14

r_w	inner radius of plasma envelope, p.14
r_1	hybrid layer location, p.7
S^C	connective energy flux, p.64
S^{EM}	electromagnetic energy flux (Poynting's vector), p.64
$\underset{\sim}{S}^{incident}$	Poynting's vector for the incident electromagnetic field, p.20
$\underset{\sim}{S}^{scattered}$	Poynting's vector for the scattered electromagnetic field, p.20
$S_m^{R,M}$	scattering coefficients for real or mirror columns in the image array, p.28
s_m	plane wave scattering coefficient, p.19
TE,TM	transverse electric and magnetic waveguide modes, p.13
T, T_e	electron temperature, p.40
T_g	neutral gas temperature, p.68
T_i	ion temperature, p.72
t_a	afterglow time, p.44
t_{ML}	matched line transmission coefficient, p.34
U_p	local particle energy, p.42
u,v	combinations of Bessel functions used in Eqn. (2.9), p.23
$\underset{\sim}{v}$	electron velocity, p.2
v_R	speed at Ramsauer minimum, p.69
v_{th}	thermal velocity, p.102
(x,y,z)	Cartesian coordinates, p.6
Y_m	Bessel function of the second kind, p.21
$\alpha(\xi)$	radially dependent dimensionless parameter related to dielectric constant, p.49
α	$\alpha(0)$, p.77
α_1	derivative of $\alpha(\xi)$ at hybrid point, p.50

Γ	normalized collision parameter, p.18
γ	Euler's constant, Appen. B, p.111
δ	Dirac delta function, p.32
ε_{glass}	permittivity of the glass envelope, p.21
ε_0	permittivity of free space, p.18
ζ	complex radial coordinate centered on the hybrid point, p.50
ζ_{ca}	distance of closest approach to the hybrid point, p.60
ζ_{max}	point at which cold plasma solutions are maximum, p.51
$\tilde{\zeta}$	normalized coordinate related to ζ, p.56
κ	Boltzmann's constant, p.40
Λ	dimensionless temperature parameter, p.55
λ	wavelength, p.34, temperature parameter defined after Eqn. (4.8), p.53
μ_{ex}	refractive index for extraordinary waves, p. 3
μ_0	permeability of free space, p.17
$\nu_{en}(v)$	electron-neutral momentum transfer collision frequency, p.68
$\langle\nu\rangle$	effective collision frequency, p.15
$\langle\nu_{ei}\rangle$	effective electron ion collision frequency, p.70
$\langle\nu_t\rangle$	effective transit time damping, p.69
ξ	normalized coordinate, p.18
(ξ_ℓ,θ_ℓ)	polar coordinates of the observation point relative to the ℓth column in an image array, p.26
$\tilde{\xi}$	$n_g\xi$, p.21
σ_a	plane wave absorption coefficient, p.93
$\sigma_m(v)$	momentum transfer cross section, p.68

σ_s	plane wave scattering cross section, p.80
ϕ,ψ	angular arguments used in Eqn. (2.12), p.28
Ω_c	normalized cyclotron frequency, p.18
$\Omega_p^2(\xi)$	normalized plasma density, p.18
ω	working frequency, p.1
ω_c	electron cyclotron frequency, p.2
ω_{ci}	ion cyclotron frequency, p.15
ω_p	electron plasma frequency, p.1
$\bar{\omega}_p$	average electron plasma frequency, p.1
ω_{pi}	ion plasma frequency, p.15
$\omega_{p\ max}$	maximum electron plasma frequency, p.6
ω_{uh}	upper hybrid frequency, p.2

Appendix B

Rapidly Convergent Forms for the $h_n^{M,R}$ Series Appearing in Section 2.4

The question of summing the Schloemilch series in Eqn. (2.14), Section 2.4 is of interest, since these series are slowly convergent as given, and useful, rapidly convergent forms can be developed. Recalling the definition of the G_n, Eqn. (2.19), the $h_n^{M,R}$ can be expressed in terms of the G_n via:

$$h_n(y_0) = \frac{(-1)^{n/2}}{2} \lim_{\xi \to 0} (G_n(\xi,\theta,y_0) - H_n^{(2)}(\xi)) \quad , \text{ n even} \qquad (B.1)$$

where $h_n^R = h_n(2b)$ and $h_n^M = h_n(b) - h_n^R$. Recall that Eqns. (2.17) require the $h_n^{M,R}$ only for n even. In Eqn. (B.1) the G_n are obtained by applying the raising operator to Eqn. (2.24). The limiting process in Eqn. (B.1) is nontrivial and is detailed in Infeld [53] for $n = 0$. The results for all n are quoted in Dumery [24] and are repeated below with some typographical errors corrected and specialized to the case of interest:

$$h_0(y_0) = -\frac{1}{2} + \frac{1}{k_0 y_0} + \frac{i}{\pi}\left[\gamma + \ell n\left(\frac{k_0 y_0}{4\pi}\right) + \sum_{\ell=1}^{\infty}\left(\frac{1}{\sqrt{\ell^2 - \left(\frac{k_0 y_0}{2\pi}\right)^2}} - \frac{1}{\ell}\right)\right]$$

$$h_{2n}(y_0) = \left[\frac{(-1)^{\ell}}{(k_0 y_0)^2}\right]^n \left[\sum_{\ell=-\infty}^{\infty} \frac{\left[2\ell\pi + i\sqrt{(k_0 y_0)^2 - (2\ell\pi)^2}\,\right]^{2n}}{\sqrt{(k_0 y_0)^2 - (2\ell\pi)^2}}\right] - \frac{i}{n\pi}$$

$$- \frac{i}{2\pi} \sum_{\ell=1}^{n} \frac{(-1)^{\ell}(\ell + n - 1)!}{(2\ell)!\,(n-\ell)!} \left(\frac{4\pi}{k_0 y_0}\right)^{2\ell} B_{2\ell}$$

where B_{ℓ} is the ℓ^{th} Bernoulli number, and γ is Euler's constant (= 0.577..).

Appendix C

Plane Wave Scattering and Absorption Cross Sections for the Cylindrical Column

The treatment of the plane wave problem presented in Section 2.3 results in Eqns. (2.9) for the plane wave scattering coefficients s_m. While these coefficients represent a complete solution of the scattering problem, it is useful to determine the cross sections for scattering and absorption, since these are usually the quantities which are experimentally measured.

For the two-dimensional problem, the scattering cross section σ_s is defined as the total power per unit axial length carried (outward) by the scattered wave divided by the incident power per unit area. The absorption cross section σ_a is defined as the net power per unit axial length which the total field carries toward the plasma column across any surface surrounding the column divided by the incident power per unit area. Thus the two-dimensional cross sections are expressed as lengths.

Symbolically, the scattering cross section may be written as:

$$\sigma_s = \frac{\int_0^{2\pi} \frac{1}{4}\sqrt{\frac{\epsilon_0}{\mu_0}}\ \mathrm{Re}\left[(\underset{\sim}{E}^{scatt} \times [cB^{scatt}]^*)\right] \cdot \hat{a}_r r\, d\theta}{\frac{1}{4}\sqrt{\frac{\epsilon_0}{\mu_0}} \int_0^1 (E_y^{inc})(cB_z^{inc})^*\, dy}$$

$$= \int_0^{2\pi} \mathrm{Re}\left[E_\theta^{scatt}(\xi,\theta)\ c(B_z^{scatt}(\xi,\theta))^* \right] \frac{\xi}{k_0}\, d\theta \qquad (C.1)$$

Substituting into Eqn. (C.1) the expressions for the scattered fields in terms of Hankel functions (see Section 2.3), utilizing the Wronskian for J_m and Y_m, and performing the indicated integration, yields the scattering cross section as a single series in m as follows:

$$\sigma_s = \frac{4}{k_0} \sum_{m=-\infty}^{\infty} |s_m|^2 \tag{C.2}$$

For the absorption cross section,

$$\sigma_a = - \int_0^{2\pi} \mathrm{Re}\left[E_\theta^{ext}(\xi,\theta)(cB_z^{ext}(\xi,\theta))^* \right] \frac{\xi}{k_0} \, d\theta$$

Using the expressions for the total fields given in Eqns. (2.4) and carrying out the manipulations yields:

$$\sigma_a = - \frac{4}{k_0} \sum_{m=-\infty}^{\infty} \{ |s_m|^2 + \mathrm{Im}[i^{m+1} s_m] \} \tag{C.3}$$

Since the s_m can be derived independently for each m in the plane wave case, the form of Eqns. (C.2) and (C.3) makes it possible to determine scattering and absorption cross sections for each value of m separately.

REFERENCES

1. L. Tonks, I. Langmuir, Phys. Rev. 33, 195 (1929).

2. L. Tonks, Phys. Rev. 37, 1458 (1931);
L. Tonks, Phys. Rev. 38, 1219 (1931).

3. N. Herlofson, Arkiv Fysik 3, 247 (1951).

4. E. M. Barston, Ann. Phys. 29, 282 (1964).

5. D. M. Henderson, Ph.D. thesis, Yale University (1970).

6. P. M. Platzman, H. T. Ozaki, J. Appl. Phys. 31, 1597 (1960).

7. F. W. Crawford, G. S. Kino, A. B. Cannara, J. Appl. Phys. 34, 3168 (1963).

8. P. E. Vandenplas, A. M. Messiaen, Nucl. Fusion 5, 47 (1965).

9. T. H. Stix, The Theory of Plasma Waves McGraw-Hill Book Co., New York, 1962.

10. G. Bekefi, J. D. Coccoli, E. B. Hooper, S. J. Buchsbaum, Phys. Rev. Letters 9, 6 (1962).

11. K. G. Budden, Radio Waves in the Ionosphere, University Press, Cambridge, 1961.

12. A. F. Kuckes, A. Y. Wong, Phys. Fluids 8, 1161 (1965).

13. F. A. Blum, L. O. Bauer, R. W. Gould, R. L. Stenzel, Phys. Fluids 12, 1018 (1969).

14. F. A. Blum, Ph.D. thesis, California Institute of Technology (1968).

15. R. L. Stenzel, Ph.D. thesis, California Institute of Technology (1969).

16. I. B. Bernstein, Phys. Rev. 109, 10 (1958).

17. S. J. Buchsbaum and A. Hasegawa, Phys. Rev. 143, 303 (1966).

18. D. E. Baldwin, J. Plasma Phys. 1, 289 (1967).

19. A. L. Rabenstein, Arch. Rational Mech. Anal. 1, 418 (1958).

20. D. E. Baldwin, Phys. Fluids 12, 279 (1969).

21. D. E. Baldwin, D. W. Ignat, Phys. Fluids 12, 697 (1969).

22. G. Dumery, C. R. Acad. Sc. Paris 260, 3857 (1965).

23. G. Dumery, C. R. Acad. Sc. Paris 262, 1481 (1966).

24. G. Dumery, Acustica 18, 334 (1967).

25. V. L. Ginzburg, Propagation of Electromagnetic Waves in Plasma, Gordon and Breach, Science Publishers, Inc., New York, 1961.

26. T. H. Stix, Phys. Rev. Letters 15, 878 (1965).

27. H. H. Kuehl, Phys. Rev. 154, 124 (1967).

28. Ting-wei Tang, Phys. Fluids 13, 121 (1970).

29. C. L. Hedrick, Ph.D. thesis, University of California, Los Angeles (1970).

30. N. G. Denisov, JETP (U.S.S.R.) 31, 609 (1956) [Soviet Physics--JETP 4, 544 (1957)].

31. V. V. Dolgopolov, ZTF 36, 273 (1966) [Soviet Physics--Technical Physics 11, 198 (1966)].

32. E. Jahnke, F. Emde, F. Losch, Tables of Higher Functions, McGraw-Hill Book Co., Inc., New York, 1960.

33. S. J. Buchsbaum, A. Hasegawa, Phys. Rev. Letters 12, 685 (1964).

34. J. C. de Almeida Azevedo, M. L. Vianna, Phys. Rev. 177, 300 (1969).

35. G. A. Pearson, Phys. Fluids 9, 2454 (1966).

36. K. Oswatitsch, in Handbuch der Physik, Springer-Verlag, Berlin, Vol. 8, no. 1, p.116;
H. Schlichting, in Handbuch der Physik, Springer-Verlag, Berlin, Vol. 8, no. 1, p.370.

37. R. C. Clemmow, J. P. Dougherty, Electrodynamics of Particles and Plasmas, Addison Wesley, Reading, Mass., 1969.

38. E. H. Holt, R. E. Haskell, Foundations of Plasma Dynamics, Macmillan, New York, 1965.

39. M. A. Heald, C. B. Wharton, Plasma Diagnostics with Microwaves, John Wiley and Sons Inc., New York, 1965.

40. C. L. Chen, Phys. Rev. 135, A627 (1964).

41. L. S. Frost, A. V. Phelps, Phys. Rev. 136, A1538 (1964).

42. C. Oberman, A. Ron, J. Dawson, Phys. Fluids 5, 1514 (1962).

43. C. Oberman, F. Shure, Phys. Fluids 6, 834 (1963).

44. J. Dawson, C. Oberman, Phys. Fluids 5, 517 (1962)

45. R. Greenwald, F. I. Boley, Phys. Fluids 13, 1380 (1970);
R. Greenwald, Ph.D. thesis, Dartmouth College (1969).

46. C. D. Lustig, Phys. Rev. 139, A63 (1965).

47. H. J. Schmitt, G. Meltz, P. J. Freyheit, Phys. Rev. 139, A1432 (1965).

48. S. Tanaka, J. Phys. Soc. Japan 21, 1804 (1966).

49. S. J. Buchsbaum, L. Mower, S. C. Brown, Phys. Fluids 3, 806 (1960).

50. R. L. Bruce, F. W. Crawford, R. S. Harp, J. Appl. Phys. 39, 3349 (1968).

51. A. T. Alper, S. Gruber, Phys. Fluids 13, 1089 (1970).

52. R. Cano, I. Fidone, G. Granata, Bull. Am. Phys. Soc. 14, 1067 (1969).

53. L. Infeld, V. G. Smith, W. Z. Chien, J. Math. and Phys. 26, 22 (1947).